TIJERAS ARROYO INFILTRATION EXPERIMENT

James R. Brainard (SNL/NM)
Peter W. Burck (INTERA Inc.)
Mehdi Eliassi (SNL/NM)
James T. McCord (SNL/NM)
Robert J. Glass (SNL/NM)
Craig Roepke (INTERA Inc.)
Robert Holt (Associated Western University)
Daniel Garrett (SNL/NM)
Diana Crowson (SNL/NM)
Don Fox (SNL/NM)
Paul Giarratano (University of New Mexico)
Kelly Kriel (SNL/NM)
Michael Mann (SNL/NM)
Curtis Cherne (SNL/NM)

Sandia National Laboratories/New Mexico
Albuquerque, NM

March 1996

EXECUTIVE SUMMARY

This report describes the Tijeras Arroyo Infiltration Experiment (TAIE) conducted at Sandia National Laboratories/New Mexico (SNL/NM). The TAIE was performed by the SNL/NM Geohydrology Department as part of the vadose zone characterization activities portion of the Site-Wide Hydrogeologic Characterization Project. The Project was established to assist the SNL/NM Environmental Restoration Project by characterizing the hydrogeologic system of Kirtland Air Force Base.

The TAIE is intended to help characterize vadose zone response to intermediate-scale ponded infiltration events such as spills and leaks from tanks, pipelines, and other intermediate-sized effluent discharge contamination events. The infiltration test was performed in alluvial fan deposits which, due to similar depositional and pedogenic processes and histories, exhibit textural heterogeneities that are analogous to other near-surface deposits found within KAFB. The TAIE objectives include comparing and contrasting vadose zone characterization and monitoring techniques as applied to texturally complex alluvial fan deposits throughout KAFB and testing numerical modeling approaches that may be applied to aid with assessment and predictions at various SNL/NM ER sites.

The infiltration experiment was performed at the end of a ridge extending from the north escarpment of Tijeras Arroyo just northeast of Pennsylvania Blvd. Five radial trenches excavated on the slopes below the infiltration site provided a means to describe the geology at the site. The geology in one of the trenches was described in detail. Seven geologic units were identified that provided the basis for Correlations to the other trenches and to instrument bore holes which provided a means to construct geologic cross-sections across the site.

The infiltration experiment involved applying water to the ground surface for 26 days through a 2-m diameter constant-head infiltrometer ring while monitoring wetting front advancement and redistribution with a variety of subsurface probes. The probes included arrays of time domain reflectometry (TDR) moisture probes, neutron access tubes, tensiometers paired with TDR probes, tensiometers targeted in specific geologic units, and thermocouples to monitor thermal response to infiltration. Each array of probes was installed in an axi-symmetric grid relative to the center of the infiltrometer. Infiltration of rain water and evaporation was prevented by two layers of water proof tarps, each covered with dirt. Holes were cut in the tarps to accommodate the infiltrometer, tensiometer casings, and neutron access tubes. Additionally, an infiltrometer cover consisting of a plywood deck, prevented additional losses and gains due to precipitation and evaporation.

Hydrologic characterization included determination of initial moisture contents across the infiltration site from a series of soil samples collected during instrumentation. Undisturbed soil samples (carefully excavated and encased in sample rings to preserve the original pore structure) from the trenches were used to determine saturated hydraulic conductivity and pressure-saturation curves in the laboratory.

This report provides an overview of the site geology, a detailed description of the site setup and soil sample collection methods. The report also describes equipment components (e.g. dataloggers, multiplexers, probes etc.) as well as calibration, installation, and data reduction techniques used in the water flow, water temperature, TDR moisture, neutron probe, pressure field, thermocouple, and weather station systems.

Based on the data presented in this report, some general conclusions can be made concerning equipment performance and vadose zone response.

Conclusions regarding equipment performance include the following: The data acquisition equipment performed well enough to provide useful information on flow rates, wetting front advancement, and changes in soil tensions during the redistribution phase of the test. Although the TDR data acquisition systems operated correctly and provided a detailed record of wetting front arrival times, anomalous readings did occur making moisture content data suspect.

Conclusions concerning vadose zone response include the following: Neutron data suggest that the lateral movement of the wetted bulb slightly outpaced the downward movement. Also, lateral spread of the wetted bulb was more extensive in the coarse textured layer which is sandwiched between two finer textured layers. Numerical simulations of homogenous material incorporating textbook values of hydraulic properties can misrepresent true conditions. However, when the undisturbed sample hydraulic properties were used, the computed wetting front advancement was more representative of the observed behavior.

The TAIE accomplishments include: 1) implementation of the infiltration test, 2) mapping of the geology underlying the site, 3) determination of hydraulic properties of soil samples collected at the site, and 4) completing numerical simulations incorporating non-hysteretic and hysteretic conditions.

Selected representative results are presented for soil samples, the water flow system, the TDR moisture system, the neutron probe, the pressure field, the thermocouple system, weather station and the numerical simulation results.

CONTENTS

Section Page

Executive Summary. ii
Contents. iv
List of Figures. viii
List of Tables. xii

1.0I INTRODUCTION 1-1

1.1 Context of the TAIE within the SNL/NM Environmental Restoration Project 1-1
1.2 Context of the TAIE within Current Understanding of Vadose Zone Processes 1-1
1.3 TAIE Site History and Timeline 1-2
1.3.1 Scope of Report. 1-2
1.3.2 Summary of Accomplishments 1-2

2.0 TIJERAS ARROYO EXPERIMENT PROJECT OBJECTIVES 2-1

3.0 GENERAL EXPERIMENTAL DESIGN 3-1

4.0 SITE SETTING 4-1

4.1 Regional SNL/KAFB Hydrogeologic Setting 4-1
4.2 TAIE Site Geology 4-2
4.2.1 Alluvial Fans and Terraces on SNL/KAFB 4-2
4.2.2 TAIE Site Shallow Subsurface as Revealed in Trenches 4-3
4.2.3 T165 Geologic Units 4-3
4.2.4 Geologic Cross-Sections 4-5

5.0 SITE LAYOUT, INSTRUMENTATION, AND DATA ACQUISITION. 5-1

5.1 Overview of Site and Preparation Activities 5-1
5.1.1 Site Selection 5-1
5.1.2 Monitoring Equipment 5-1
5.1.3 Site Preparation Activities 5-1

5.2 Infiltration Site Setup 5-1
5.2.1 Introduction 5-1
5.2.2 Overview of Site 5-2
5.2.3 Subsurface Paired TDR and Tensiometer Array 5-2
5.2.4 Surface TDR Array 5-3
5.2.5 Geology Tensiometers 5-3
5.2.6 Neutron Access Tubes 5-3
5.2.7 Trenches 5-3

5.3 Water Supply System 5-4

5.4 Infiltrometer And Ground Surface Evaporation Barrier 5-4
5.4.1 Infiltrometer and Infiltrometer Deck 5-4
5.4.2 Ground Surface Evaporation Barrier 5-5

5.5 Data Acquisition And Reduction Overview 5-5

5.6 Water Flow Monitoring Systems 5-5
5.6.1 Introduction 5-5
5.6.2 Description of System 5-5
5.6.3 Calibration Method 5-6
5.6.4 Installation Method 5-6
5.6.5 Data Reduction 5-6

5.7 Water Temperature Monitoring System 5-7
5.7.1 Introduction 5-7
5.7.2 Description of System 5-7
5.7.3 Calibration Method 5-7
5.7.4 Installation Method 5-7
5.7.5 Data Reduction 5-7

5.8 TDR Systems 5-8
5.8.1 Introduction 5-8
5.8.2 Description of System 5-8
5.8.3 Calibration Method 5-8
5.8.4 Installation Method 5-8
5.8.5 Data Reduction 5-9

5.9 Neutron Probe Moisture Measurements 5-9
5.9.1 Introduction 5-9
5.9.2 Description of System 5-9
5.9.3 Calibration 5-9
5.9.4 Installation Method 5-9
5.9.5 Data Reduction 5-9

5.10 The Pressure Field 5-9
5.10.1 Introduction 5-9
5.10.2 Description of System 5-9
5.10.3 Calibration 5-10
5.10.4 Installation Methods 5-10
5.10.5 Data Reduction 5-11

5.11 The Thermocouple System 5-11
5.11.1 Introduction 5-11
5.11.2 Description of System 5-11
5.11.3 Calibration 5-11
5.11.4 Installation Technique 5-11
5.11.5 Data Reduction 5-11

5.12 The Weather Station 5-11
5.12.1 Introduction 5-11
5.12.2 Description of System 5-11
5.12.3 Calibration 5-12
5.12.4 Installation Technique 5-12
5.12.5 Data Reduction 5-12

5.13 Soil Sample Collection 5-12
5.13.1 Introduction 5-12
5.13.2 Samples Used for Hydraulic Properties 5-12
5.13.3 Samples Used for Initial Moisture Contents 5-12
5.13.4 Samples Used for Geologic Cross-Section Construction 5-13

6.0 RESULTS AND DISCUSSION 6-1

6.1 Water Flow Results 6-1
6.1.1 Introduction 6-1
6.1.2 Manually-Collected Infiltration Data 6-1
6.1.3 Infiltrometer Supply Tank Pressure Transducer Data 6-1

6.2 TDR Moisture Results 6-1
6.2.1 Introduction 6-1
6.2.2 TDR Moisture Data 6-1
6.2.3 Discussion 6-1

6.3 Neutron Probe Results 6-2
6.3.1 Introduction 6-2
6.3.2 Neutron Count Data 6-2
6.3.3 Discussion 6-2

6.4 Pressure Field Results 6-2
6.4.1 Introduction 6-2
6.4.2 Tensiometer Data 6-2
6.4.3 Discussion 6-3

6.5 Thermocouple Results 6-3
6.5.1 Introduction 6-3
6.5.2 Thermocouple Data 6-4
6.5.3 Discussion 6-4

6.6 Weather Station Results 6-4
6.6.1 Introduction 6-4
6.6.2 Weather Station Data 6-4

6.7 Soil Sample Results 6-5

7.0 NUMERICAL STUDIES 7-1

7.1 Theoretical Background 7-1
7.1.1 Governing Equations 7-1
7.1.2 Scott's Model of Capillary Hysteresis 7-3
7.1.3 Numerical Implementation of the Richards Equation 7-4
7.1.4 Basic Algorithm for Determining the Hysteretic Curves 7-5

7.2 Pre-Test Numerical Modeling 7-5
7.2.1 Model Problem 7-6
7.2.2 Initial and Boundary Conditions 7-6
7.2.3 Hydraulic Properties 7-6
7.2.4 Undisturbed Sample 7-6
7.2.5 Text Book Values 7-7

7.3 Numerical Grid System 7-7
7.3.1 Effect of Grid Resolution 7-7
7.3.2 Numerical Verifications 7-7

7.4 Two-Dimensional Axisymmetric Simulations 7-8
7.4.1 Non-hysteretic Calculations 7-8
7.4.2 Hysteretic Calculations 7-9
7.4.3 Calculations Using Text Book Values 7-9

7.5 Summary 7-10

8.0 SUMMARY AND CONCLUSIONS 8-1

9.0 REFERENCES 9-1

FIGURES

TABLES

LIST OF FIGURES

Figure 3.1: General Location Map of SNL/NM

Figure 3.2: SNL/KAFB Location Map

Figure 3.3: Plan View of Infiltration Site and Surrounding Area

Figure 4.1.1: Vadose Zone Hydrogeologic Settings

Figure 4.2.1: Southwest-Northeast Geologic Cross-Section

Figure 4.2.2: Northwest-Southeast Geologic Cross-Section

Figure 4.2.3: South-West Geologic Cross-Section

Figure 4.2.4: North-East Geologic Cross-Section

Figure 4.2.5: Plan View Showing the Locations of the Southwest-Northeast and Northwest-Southeast Geologic Cross-Sections

Figure 4.2.6: Plan View Showing the Locations of the South-West and North-East Geologic Cross-Sections

Figure 5.2.1: Schematic Plan View of Infiltration Site (Not to Scale)

Figure 5.2.2: Schematic Plan View of Infiltration Site Detail (Not to Scale)

Figure 5.2.3: Plan View of Instrument Array Showing Layout of Instrument Arrays

Figure 5.4.1: Infiltrometer and Infiltrometer Deck Details

Figure 5.6.1: 500 Gallon Infiltrometer Water Supply Tanks

Figure 5.6.2: Resistive Water Level Recording Device

Figure 5.6.3: Pressure Transducer in PVC Tee

Figure 5.7.1: Water Temperature Probes in PVC Pipe

Figure 5.8.1: TDR Probe Detail

Figure 5.8.2: Results of Sampling and TDR Calibration in the Red, Silty Loam

Figure 5.10.1: Tensiometer Detail

Figure 6.1.1: Infiltration Rates from Manually Measured Supply Tank Water Levels

Figure 6.1.2: Cumulative Infiltration from Manually Measured Supply Tank Water Levels

Figure 6.1.3: Infiltrometer Water Supply Tanks Pressure Transducer Data

Figure 6.2.1: North Inner TDR Group Moisture Content Results

Figure 6.2.2: North Medial TDR Group Moisture Content Results

Figure 6.2.3: North Outer TDR Group Moisture Content Results

Figure 6.2.4: Northeast Radial TDR Array Moisture Content Results

Figure 6.3.1: Center Neutron Access Tube Moisture Count Results

Figure 6.3.2: Northeast 2.5 m Neutron Access Tube Moisture Count Results

Figure 6.3.3: Northeast 4.5 m Neutron Access Tube Moisture Count Results

Figure 6.3.4: Northeast 5.5 m Neutron Access Tube Moisture Count Results

Figure 6.4.1: North Inner Tensiometer Group Transducer Potential Results

Figure 6.4.2: North Medial Tensiometer Group Transducer Potential Results

Figure 6.4.3: North Outer Tensiometer Group Transducer Potential Results

Figure 6.4.4: North Geology Tensiometer Group Transducer Potential Results

Figure 6.5.1: 1 Meter (1m) Thermocouple Data

Figure 6.5.2: 2 Meter (2m) Thermocouple Data

Figure 6.5.3: 3 Meter (3m) Thermocouple Data

Figure 6.5.4: 4 Meter (4m) Thermocouple Data

Figure 6.6.1: Weather Station Air Temperature Data

Figure 6.6.2: Weather Station Barometric Pressure Data

Figure 6.6.3: Weather Station Precipitation Data

Figure 6.6.4: Weather Station Relative Humidity Data

Figure 7.1 The suction-moisture content curves for the Main Wetting Curve (MWC) and Main Drainage Curve (MDC) forming the hysteresis loop

Figure 7.2 The suction-moisture content curves for the main hysteresis loop and two scanning curves

Figure 7.3 Schematic of the model problem in axi-symmetric cylindrical coordinates

Figure 7.4 Pressure versus moisture content curves for TA-1 Undisturbed Sample (MDC from data, MWC predicted from MDC)

Figure 7.5 Pressure versus moisture content curves for a typical silt (MDC from RETC manual, MWC predicted from MDC)

Figure 7.6 Moisture Content as a function of depth. Comparison of three different codes (1-D, nonhysteretic model, htop = -0.1 m)

Figure 7.7 Tijeras Arroyo Infiltration Simulation (Nonhysteretic, MDC, Time = 25 days)

Figure 7.8 Tijeras Arroyo Infiltration Simulation (Nonhysteretic, MDC, Time = 50 days)

Figure 7.9 Tijeras Arroyo Infiltration Simulation (Nonhysteretic, MDC, Time = 75 days)

Figure 7.10 Tijeras Arroyo Infiltration Simulation (Nonhysteretic, MDC, Time = 100 days)

Figure 7.11 Profile Along the Axis of Symmetry (Non-hysteretic MDC)

Figure 7.12 Tijeras Arroyo Infiltration Simulation (Nonhysteretic, MWC, Time = 25 days)

Figure 7.13 Tijeras Arroyo Infiltration Simulation (Nonhysteretic, MWC, Time = 50 days)

Figure 7.14 Tijeras Arroyo Infiltration Simulation (Nonhysteretic, MWC, Time = 75 days)

Figure 7.15 Tijeras Arroyo Infiltration Simulation (Nonhysteretic, MWC, Time = 100 days)

Figure 7.16 Profile Along the Axis of Symmetry (Non-hysteretic MWC)

Figure 7.17 Tijeras Arroyo Infiltration Simulation (Hysteretic, Time = 25 days)

Figure 7.18 Tijeras Arroyo Infiltration Simulation (Hysteretic, Time = 50 days)

Figure 7.19 Tijeras Arroyo Infiltration Simulation (Hysteretic, Time = 75 days)

Figure 7.20 Tijeras Arroyo Infiltration Simulation (Hysteretic, Time = 100 days)

Figure 7.21 Profile Along the Axis of Symmetry (Hysteretic)

Figure 7.22 Tijeras Arroyo Infiltration Simulation (Nonhysteretic, MDC, Time = 25 days, Text Book Values)

Figure 7.23 Tijeras Arroyo Infiltration Simulation (Nonhysteretic, MDC, Time = 50 days, Text Book Values)

Figure 7.24 Tijeras Arroyo Infiltration Simulation (Nonhysteretic, MDC, Time = 100 days, Text Book Values)

Figure 7.25 Tijeras Arroyo Infiltration Simulation (Nonhysteretic, MWC, Time = 25 days, Text Book Values)

Figure 7.26 Tijeras Arroyo Infiltration Simulation (Nonhysteretic, MWC, Time = 50 days, Text Book Values)

Figure 7.27 Tijeras Arroyo Infiltration Simulation (Nonhysteretic, MWC, Time = 100 days, Text Book Values)

Figure 7.28 Tijeras Arroyo Infiltration Simulation (Hysteretic, Time = 25 days, Text Book Values)

Figure 7.29 Tijeras Arroyo Infiltration Simulation (Hysteretic, Time = 50 days, Text Book Values)

Figure 7.30 Tijeras Arroyo Infiltration Simulation (Hysteretic, Time = 100 days, Text Book Values)

LIST OF TABLES

Table 5.1: Descriptors for Figure 5.2.3

Table 5.2: Water Flow Monitoring Components

Table 5.3: Water Temperature Monitoring System Components

Table 5.4: TDR Moisture System Components

Table 5.5: Pressure System Components

Table 5.6: Thermocouple System Components

Table 5.7: Weather Station Components

Table 6.1: Moisture Content Results of Soil Samples Taken from the Geology Holes

Table 6.2: Gravimetric Moisture Content Results of Soil Samples Taken from the 4.5 m Neutron Access Tubes

Table 7.1: Fitting Parameters for the van Genuchten model using undisturbed samples

Table 7.2: Fitting Parameters for the van Genuchten model for a typical silt

Table 7.3: Two-dimensional grid system used to perform the simulation of the model problem

Tijeras Arroyo Infiltration Experiment

1.0 INTRODUCTION

This report describes the Tijeras Arroyo Infiltration Experiment (TAIE) conducted at Sandia National Laboratories/New Mexico (SNL/NM). The TAIE was performed by the SNL/NM Geohydrology Department (Organization 6115) as part of the vadose zone characterization portion of the Site-Wide Hydrogeologic Characterization (SWHC) Project. The SWHC Project was established to assist the SNL/NM Environmental Restoration (ER) Project by characterizing the hydrogeologic system of Kirtland Air Force Base (KAFB).

The TAIE is designed to characterize the vadose zone response to situations in which fluids are spilled or dumped in the vadose zone at a rate higher than the saturated hydraulic conductivity of the geologic media. The TAIE thus provides an analogue to leaky tank or pipeline and similar intermediate-scale effluent discharge scenarios.

This report is organized as follows. The remainder of Section 1 provides a brief description of the SNL/NM ER Project background and the role of the SWHC Project in the context of ER, and also outlines the overall vadose zone characterization task of the SWHC Project. Section 2 explicitly states the TAIE project objectives. The general experimental design is outlined in Section 3. The TAIE site geology and subsurface hydrogeologic characterization efforts are described in Section 4. Section 5 provides details on site preparation and instrumentation. Selected results from pre-infiltration monitoring, infiltration event response, and post-infiltration redistribution are summarized in Section 6, and modeling results are contained in Section 7. Section 8 contains a summary and conclusions.

1.1 Context of the TAIE within the SNL/NM Environmental Restoration Project

The Sandia ER Project is concerned with identifying, characterizing, and if necessary remediating, potential contamination sites at SNL/NM following the Resource Conservation and Recovery Act (RCRA) Corrective Action process. For a thorough overview of SNL/NM or the ER Project, the reader is directed to the *Program Implementation Plan for Albuquerque Potential Release Sites* (SNL/NM, 1994a).

In addition to performing site-specific characterization, the ER Project has recognized the need to understand better the regional hydrogeologic framework. Consequently, the SWHC Project was established in part to assist SNL/NM ER task leaders in understanding the hydrogeology at each ER site by characterizing the regional hydrogeologic system.

The TAIE described in this report is intended to provide information on vadose zone response to intermediate-scale spills and leaks and to increase our understanding of and ability to assess scenarios with hydraulic loading.

1.2 Context of the TAIE within Current Understanding of Vadose Zone Processes

The precise mode(s) of deep water flow through the thick alluvial sediments (such as those underlying SNL/KAFB) is poorly understood. In the vadose zone, fine-grained material (small pores) may act as the preferred pathway for moisture movement while coarse-grained material (larger pores) can act as a barrier to flow (Ross, 1990; Oldenburg and Pruess, 1993). Layers and lenses could cause preferential flow to occur as well as enhancing dispersion processes (McCord and Goodrich, 1995). The presence of paleochannels and paleosols could also impact flow paths through the vadose zone. Development of conceptual models for contaminant movement through the vadose zone requires an understanding of the thickness, lateral extent, and bedding plane aspects of different geologic units.

The horizontal layering of the geologic media in the vadose zone probably causes spatially variable

natural surface fluxes to be smoothed into a fairly uniform downward drainage below a few meters of depth. Bulbs of high saturation develop beneath large fluid sources such as intensively used septic tank leach fields. Furthermore, there is the possibility that even natural, non-uniform surface wetting may act synergistically with the media's unsaturated hydraulic characteristics (e.g. unsaturated conductivity-moisture content relationships, water-entry and air-entry pressures) to permit non-uniform flow to propagate to great depths. Unsaturated "finger flow" or channeling of fluids to the water table may even occur (see studies by Glass et al., 1988). In such cases, the expected time of contaminant transport from the ground surface to the ground-water system may be greatly reduced.

In addition to the TAIE described here, other large-scale infiltration experiments have been undertaken in recent years to assess vadose zone processes in similar geologic settings. The two most detailed studies are the Las Cruces Trench Experiment (Wierenga et al., 1991) and the New Mexico Tech infiltration experiment (e.g., Stephens et al., 1988). Those two studies considered response to source flux rates which were much smaller than the soil's saturated hydraulic conductivity. A third large scale infiltration test was conducted near the Mixed Waste Landfill within Technical Area III at SNL/NM where instantaneous profile techniques were applied (Goering et al., 1996). In contrast to the first two studies, the TAIE looks at flow beneath a ponded source, and, in contrast to the third, lateral flow at the TAIE was not inhibited by artificial barriers. A fourth infiltration experiment was conducted as part of the Surface Water activities (SNL/NM, 1996, Appendix "A")

1.3 TAIE Site History and Timeline

The conceptual design for induced infiltration tests at SNL/NM began several years ago as an approach to studying and solving vadose zone hydrology problems for the SNL/NM ER and other projects (Parsons, et al., 1993 and Holt, 1992). The TAIE evolved from similar field infiltration experiments performed by the SNL/NM Geohydrology Department (Department 6115) at Fernald, Ohio in 1993 and 1994, and the Preliminary Infiltration Test in Sandia's Technical Area III west of the Mixed Waste Landfill in 1994 (see Appendix E of the 1994 SWHC Annual Report, SNL/NM, 1995).

1.3.1 Scope of Report

This report covers selected data collected during the pre-infiltration phase and from the beginning of the infiltration on Tuesday, November 7, 1995 to Monday, January 15, 1996.

1.3.2 Summary of Accomplishments

Four primary goals achieved during the include the following: 1) implementation of the infiltration experiment, 2) mapping of the geology below the infiltration site, 3) determination of hydraulic properties from samples collected at the site, and 4) numerical simulations incorporating non-hysteretic and hysteretic conditions. Accomplishments of these goals helps to provide some basis to understanding vadose zone response to large scale spills and leaks at SNL/NM ER sites.

2.0 TIJERAS ARROYO INFILTRATION EXPERIMENT PROJECT OBJECTIVES

The overall project objective is to study the physics of unsaturated flow in complicated heterogeneous vadose zone materials. This is of importance for understanding flow and transport within the vadose zone at many SNL/NM ER sites and more generally within Kirtland Air Force Base. This study will consider in particular near-surface alluvial fan deposits believed to be representative of deposits at depth. Detailed objectives of the Tijeras Arroyo Infiltration Experiment are as follows.

1. To design and implement an infiltration test to measure the 3-dimensional behavior of the flow field within near-surface alluvial fan deposits, the results of which can be applied to similar deposits found at depth.
   The infiltration test will be performed in near-surface deposits where surface material will be removed to gain access to deposits not affected by recent weathering. Controlled surface boundary conditions will be initiated while monitoring the wetting front location with time, and recording temporal changes in moisture, pressure (tension), and temperature fields. The scale of measurements will range from several to 500 cubic meters and will be defined by the spatial resolution and extent of instrumentation. Measurement systems must incorporate a dense array of probes and be capable of producing high temporal resolution.

2. To test conceptual models concerned with unsaturated flow in naturally occurring heterogeneous deposits.
   Geologic features likely to affect the flow field (e.g., zones of calcium carbonate cement and contacts between layers exhibiting different textures) will be identified and carefully mapped within the expected flow field. Conceptual models will be tested by correlating wetting front advance rates, as well as differential changes in the moisture content/pressure field during redistribution, with mapped geologic features.

3. To use results from the infiltration test to further understand relationships between small scale sample measurements and large-scale field response.
   Meeting this objective requires numerical simulations to examine flow field behavior using hydraulic properties (e.g., saturated hydraulic conductivity and pressure/saturation curves) from three sources: 1) published values from similar materials found at the site, 2) undisturbed samples collected from the site (original pore structure is preserved), and 3) repacked samples (original pore structure is destroyed). Hysteretic effects will be investigated by contrasting hysteretic and nonhysteretic flow field simulations.

4. To evaluate the error associated with hydraulic properties from field and laboratory measurements:
   This objective includes evaluation of error from field systems providing moisture, pressure, and temperature data as well as saturated hydraulic conductivity and pressure/saturation curves from laboratory measurements.

5. To compare and contrast field and laboratory measured hydraulic properties:
   Comparisons will be made between pressure/saturation curves form field measurements and laboratory measurements to provide a foundation for understanding the relationship between *in situ* and laboratory derived hydraulic properties.

3.0 GENERAL EXPERIMENT DESIGN

In order to meet the objectives presented in section 2.0, several criteria had to be met in selecting a site. First, the site had to be located on an areally extensive alluvial fan exhibiting textural heterogeneities and pedogenic features common to other alluvial fan deposits within Kirtland Air Force (KAFB). This approach will assure relevance to SNL/NM ER sites as well as to vadose zone hydrologic processes across KAFB in general. Second, the site had to be near exposed outcrops to aid in optimal site selection and provide opportunities for collecting additional geostatistical information. Finally, the site had to be situated such that a 3-dimensional view of the subsurface could be easily obtained while minimizing personnel exposure to hazardous working conditions. For these reasons, the infiltration test will be conducted at the end of a ridge extending from the north escarpment of Tijeras Arroyo. The site is to be located between Pennsylvania Blvd. and Technical Area IV (Figures 3.1, 3.2, & 3.3).

A certain amount of material will be removed from the surface of the site to expose materials unaffected by recent weathering. The amount of material removed will be determined from a preliminary geologic survey which will identify a desirable section of the profile to be infiltrated. Enough surface material will be removed to optimize the placement of instruments within the selected profile.

Detailed geologic descriptions and mapping of individual geologic units bounded by contacts between contrasting textures and/or pedogenic features will be used to correlate units between trenches. Continuous core samples extracted from the infiltration site during instrumentation will provide a means to construct a 3-dimensional view of the site geology through correlations of the individual units.

The infiltration site is to be equipped with several arrays of instruments. Instrumentation will include time domain reflectometry (TDR) moisture probes, pressure transducer-equipped tensiometers, thermocouples, and neutron access tubes. All data acquisition, other than neutron data, will be accomplished with automated multiplexed systems allowing high temporal resolution. These instruments will be installed in an axisymmetric pattern about the center of the infiltrometer. Shadowing of the flow field will be minimized by staggering groups of instruments and placing deeper instruments within groups further from the infiltrometer. Pairs of TDR probes and tensiometers will be installed adjacent to each other and at the same depth to provide simultaneous measurements of moisture contents and matric potential. Initial conditions will be obtained from grab and split spoon samples collected during installation of instruments.

The infiltration test will involve applying water to the freshly exposed alluvial fan materials through a ponded source while monitoring flow rates. When the wetting front approaches the outer-and/or the lower-most TDR probes, infiltration will be stopped and the redistribution phase will begin. Redistribution will be allowed to continue for an indefinite period of time.

Undisturbed soil samples (samples in which the original pore structure is preserved) will be collected in the trenches from each of the geologic units. Sample collection will involve carving soil pedestals from the trench walls and encasing the samples inside brass rings with injections of expandable foam. These samples will be subjected to standard laboratory tests to obtain saturated hydraulic conductivity and pressure/saturation curves. These tests will be repeated after each sample is removed from the ring and repacked in a new ring.

4.0 SITE SETTING

The SWHC Project Annual Reports (McCord et al., 1993; SNL/NM, 1994; SNL/NM, 1995; SNL/NM, 1996) describe our current understanding of the regional geology and hydrology in detail. A condensed version of the regional hydrogeology from the annual reports follows, with an emphasis on the vadose zone. This is followed by an overview of the subsurface geology at the site.

4.1 Regional SNL/KAFB Hydrogeologic Setting

The SNL/KAFB area is located in central New Mexico, in the Albuquerque basin, as shown in Figure 3.1. The Albuquerque basin is one of several north/south trending basins in the Rio Grande Rift system.

This area has a semi-arid climate, characterized by low precipitation, wide temperature extremes, frequent drying winds, occasional intense rain showers often with erosive effects, and an erratic, seasonal distribution of precipitation. Water generally enters the subsurface from rainfall and arroyo channel losses and either leaves through evapotranspiration or recharges the underlying aquifer. Due to the low precipitation and high evapotranspiration conditions for the SNL/KAFB area, recharge rates to the ground-water system from areal infiltration are low. Results to date (see SNL/NM, 1996, Appendix B) suggest interfluve (undisected highlands between drainages) ambient recharge rates are generally less than a millimeter per year and vertical downward seepage velocities less than 1 cm /year. Downward fluid fluxes beneath arroyos are markedly larger (see SNL/NM, 1996, Appendix A).

There are no continuously running streams in the SNL/KAFB area, although there is a system of arroyos that flow ephemerally, primarily during or after large thunderstorm events. The Surface Water task of the SWHC project has studied the magnitude of arroyo flow loss due to infiltration into the vadose zone resulting in possible recharge to the groundwater. These arroyo flow losses are projected to range between approximately 60 and 180 cm/yr. Tijeras Arroyo and Arroyo del Coyote may be the largest localized recharge sources in the SNL/KAFB vicinity. Thus, the portions of landfill sites and firing range sites which lie within arroyos can expect to experience much greater downward water and solute fluxes.

The major vegetation types in the SNL/KAFB area tend to vary with elevation, slope, and aspect. Generally, woodlands are found in the eastern portion of the area in the Manzanita Mountains and canyons while grasslands cover the western portion of the area on the lower elevations. Vegetation type, surface slope, and the slope aspect all affect surface runoff characteristics and evapotranspiration rates in the area. Soils in the SNL/KAFB area are developed in fluvial, alluvial fan, colluvial, and eolian surficial deposits. Variations in soil properties reflect differences in sediment characteristics, length of exposure to surface weathering, and local climate.

The presence of pedogenic calcic horizons may significantly affect downward percolation of water through the vadose zone. Pleistocene deposits typically have moderately- to well-developed calcic horizons within five or six feet of the surface, whereas Holocene deposits generally lack calcic horizons (GRAM/Lettis, 1995). The Soil Conservation Service (Hacker, 1977) designated the surficial permeabilities and available water storage capacities of the soils in the area, based on the mapped soil textures. Soil permeabilities are mainly moderate (0.2 to 6 inches/hour [0.5 to 15.2 cm/hour]), while the canyon bottoms and the Tijeras Arroyo flood plains exhibit rather high (6.0 to 20.0 inches/hour [15.2 to 50.8 cm/hour]) permeabilities. Vegetation type, slope magnitude and aspect, and surface soil permeability and storage capacity were used by Parsons et al. (in press) to define a set of nine prototypical vadose zone hydrogeologic settings which are representative of the vadose zone across the entire SNL/KAFB study area (Figure 4.1.1). According to this map TAIE is within the “slightly sloping, medium to high permeability grassland” setting, which is representative of nearly half of the SNL/KAFB area, and which underlies nearly 50% of the SNL ER sites.

The vadose zone in the SNL/KAFB area is generally comprised of unconsolidated valley fill deposits (Lozinsky, 1988; Hawley and Haase, 1992). The valley fill consists of unconsolidated and semi-consolidated sands, gravels, silts, and clays of the Santa Fe Formation, with additional poorly consolidated clastics associated with modern alluvial fans overlying the Santa Fe. On the east side of the SNL/KAFB area, the valley fill is composed of highly heterogeneous alluvial fan, fluvial, and aeolian deposits. Farther west of SNL facilities, the distal alluvial fan materials interfinger with and overlie the ancestral axial channel and overbank Rio Grande sediments. In the eastern portion of the SNL/KAFB area, there may be areas where the vadose zone is composed of bedrock materials (e.g., Precambrian, Pennsylvanian, or Permian formations) that are of relatively low permeability but may be highly fractured.

The vadose zone thickness in the SNL/KAFB area is generally quite large (from 50 to greater than 500 ft [15 to greater than 152 meters]); consequently, most contaminants released near the ground surface must travel a long distance before reaching the ground-water system. The depth to ground water, and hence vadose zone thickness, appears to be strongly controlled by the Sandia Fault, Hubbell Spring Fault, and Tijeras Fault systems. In areas west of the faults, the vadose zone is typically on the order of 300 to 500 feet (91 to 152 meters) thick. East of the faults the vadose zone thickness ranges from about 50 to 140 feet (15 to 43 meters), according to water levels recorded in monitor wells (SNL/NM, 1994). East of the fault zone, there are significant areas where bedrock is outcropping and some locations where seeps and springs indicate much smaller depths to ground water.

4.2 TAIE Site Geology

The TAIE is located at the end of a ridge extending from the north escarpment of Tijeras Arroyo south of Technical Area IV and north of Pennsylvania Boulevard. Based on detailed regional maps published in the final geologic report for the SWHC Project (GRAM/Lettis, 1995), the TAIE site is situated within Pleistocene alluvial fan. This section first provides general information on the geology of alluvial fans and terraces, and then describes in detail the shallow subsurface materials as mapped in trenches excavated at the TAIE site.

4.2.1 Alluvial fans and terraces on SNL/KAFB

The site is typical of much of SNL/KAFB as it is located on the medial portion of an alluvial fan, which makes understanding alluvial fan processes and deposits important for remediation. As a brief review, alluvial fans have a smaller number of processes and yield a smaller variety of deposits than most depositional settings. They are cone-shaped alluvial deposits, typically beginning at a mountain front, bedrock constriction, or incised sections of stream valleys. Alluvial fans consist of poorly sorted, laterally and vertically discontinuous sand, silt, and gravel beds, and are usually more than 10 feet thick. Sediments are deposited on the fan surface by several processes. In semi-arid climates debris flows and upper regime streamfloods occur during short-lived monsoon storms. As a stream emerges from the constriction of the canyon and flows onto the alluvial fan surface, its velocity decreases and it looses the ability to move large amounts of sediment. Bifurcation and deposition occur at this point. As the stream branches again farther down the fan, the coarse debris-flow deposits become less frequent and sheet-flow deposits, which are typically finer-grained and better sorted, become more common.

The TAIE site is located in the Tijeras Arroyo geomorphic subprovince of the Rift-Margin Range Province, on the medial portion of a thick and laterally extensive Pleistocene age alluvial-fan (Unit Pf3.ta). This alluvial fan is inset into and overlies upper Santa Fe Group deposits. It is also inset into older alluvial fans to the northwest of the site. Pf3.ta is exposed in the northern and southern walls of Tijeras Arroyo and Arroyo Coyote. These deposits are as much as 18 m thick at Pennsylvania Blvd. and

thicken towards the east and thin towards the west. In general, the deposits are poorly consolidated and contain thick layers of silty sand and sandy silt with intervening gravel beds. Pf3.ta has numerous buried soils, some showing significant evidence of development, indicating a complex depositional history.

4.2.2 TAIE site shallow subsurface as revealed in trenches

The site geology at the TAIE site was mapped in detail to help understand how geologic features affect fluid flow and transport in the poorly consolidated porous materials underlying essentially all SNL/NM ER sites. The TAIE site was located at the top of a knoll providing ready access to the geologic materials through the excavation of five trenches along radial transects (Figure 5.2.2). The trenches began at a distance of roughly 6 m from the center of the infiltration site, and they continued for 6 m down the slopes of the knoll. These trenches allowed detailed mapping of site stratigraphy and geologic features to depth in excess of 7 to 10 m below the level of the infiltrometer in addition to subsurface access at radial distances of more than 5 m. The geology within the area to be infiltrated was revealed through continuous core samples collected from instrument boreholes. The core data, combined with observations from the geologic trenches, provides a fairly detailed snapshot of the geology at the TAIE site.

The seven geologic units identified and described in T165 (see section 5.2 for a description of the site layout) were correlated with units in the other trenches and in continuous core samples collected from the infiltration site. These seven units are described below.

4.2.3 T165 Geologic Units

The descriptions start at Unit 1 located at the bottom of the trench. Approximate thickness of each unit, brief textural description, colors according to the Munsell color charts, and composition are given below.

Unit 1 (Unknown Thickness)
Pebble to granule conglomerate with interbeds, poorly to moderately well indurated, very calcareous.
Munsell color descriptor: 5YR 8/1.

- Cobbles, Pebbles and granules: poorly sorted with very fine sand to pebbles (clasts).
  Composition: approximately 20% quartz, 40% feldspar, 30% lithic fragments of quartz and feldspar, 10% biotite flakes and other minerals.
  Clasts are angular to subangular and resembles transported grus.
  Cobbles and pebbles mostly red sandstone (derived from Permian and /or Triassic red beds found within the mountainous drainage basin to the east).
- Interbeds: poorly sorted very fine to fine sand with abundant biotite flakes, generally fines upward, some illuvial features preserved.
- Upper contact irregular: inset channel fill at top; appears sharp to gradational.
- Lower contact obscured.

Unit 2 (0.75 to 1 m thick)
Poorly sorted, sandstone with pebbles and granules disseminated in lower part, poorly indurated, calcareous.
Munsell color descriptor: 2YR 6/4.

- Lower part: probable incipient illuviation structures with local hints of possible horizontal stratification.
- Upper part: blocky texture (illuviation) and incipient carbonate nodules.
  Upper contact sharp where overlain by channels, diffuse to gradational elsewhere.

Unit 3 (0.3 to 0.5 m thick)
Varies laterally from sandstone to conglomerate.

Munsell color descriptor: 5YR 7/3.

- Sandstone, poorly sorted medium to very fine sand,
  Composition: approximately 20% quartz, 40% feldspar, 30% lithic fragments of quartz and feldspar, 10% biotite flakes and other (?) minerals.
  Very calcareous
  Upper contact gradational to absent.

- Pebble to granule conglomerate, with some cobbles, shows weak arcuate lamination with slight dip, fines upward.
  Pebbles/granules are disseminated and floating; appear crudely aligned in subhorizontal zones.
  Pebble and granule composition: 20% quartz, 30% feldspar, 40% granitic lithic fragments, 8% other lithics including greenstone (Tijeras Greenstone), gray limestone (Pennsylvanian Madera?), red sandstone (Permian and/or Triassic Red Beds) 2% biotite.
  Upper contact gradational with caliche.
  Lower contact sharp to gradational.

Unit 4 (0.3 to 0.5 m thick)
Caliche - moderately well indurated with little to no vertical fabric but crude subhorizontal fabric present.
Munsell color descriptor: 5YR 8/1

- Lower part: developed on and into underlying unit.
- Upper part patchy and irregular, shows some subhorizontal stringers
  Upper contact: highly irregular sharp to diffuse.

Unit 5a and 5b (0.75 to 1.0 m thick)
Sandstone, very fine to medium poorly sorted sand, generally fines upward,

- Upper part (5b): blocky texture, entire unit is calcareous. Local hints of subhorizontal layering, upper contact gradational. Munsell color descriptor: 5YR 6/4.
- Lower Part (5a): pebbles and granules
  Pebbles/granules generally floating
  Composition: approximately 20% quartz, 30% feldspar, 40% granitic lithic fragments, 8% other lithics, 2% biotite. Munsell color descriptor: 7.5YR 6/6.

Unit 6 (1.0 to 1.5 m thick)
Interbedded very thin to medium thin beds of sandstone with pebble/granule conglomerate, strata are discontinuous to continuous, shows local low angle cross-cutting relationships, some ripples, and slumping. All materials are poorly indurated. Munsell color descriptor: 10 R 5/4.

- Little to no pedogenic textures, poorly sorted, calcareous.
- Pebble composition: approximately 20% quartz, 30% feldspar, 5% Madera limestone, 3% biotite, 40% granitic lithics, 2% other
- Upper contact gradational

Unit 7 (1.5 to 1.75 m thick)
Sandstone, silt to fine sand, poorly indurated, calcareous, generally structureless with hints of subhorizontal strata near base, blocky texture near top (illuviation). Munsell color descriptor: 2.5YR 6/3.

- upper contact obscure.

4.2.4 Geologic Cross-Sections
Four geologic cross-sections were constructed from continuous core samples taken from the infiltration

site (See Section 5.13 for details on sampling technique). Cross-sections are presented in Figures 4.2.1 through 4.2.4 and plan views showing the cross-sectional traces are shown in Figures 4.2.5 & 4.2.6. Each core is designated according to the hole it came from and the holes are indicated by the designator at the base of the core in the cross-section (see Section 5 for details on the instrument layout and hole designations).

The Southwest-Northeast and the Northwest-Southeast cross-sections (Figures 4.2.1 & 4.2.2) pass through the center and are orthogonal to each other while the South-West and North-East (Figures 4.2.3 & 4.2.4) cross-sections on the south and west and the north and east perimeter of the infiltration site, respectively. The longer cores in Figures 4.2.1 through 4.2.4 were obtained from the 2.5 m neutron access tube holes, while the shorter cores were obtained from TDR probe holes.

5.0 SITE LAYOUT, INSTRUMENTATION, AND DATA ACQUISITION

This section gives an overview of the Tijeras Arroyo Infiltration Experiment (TAIE) site, a detailed description of instrument arrays, information on data acquisition systems, and an overview of soil sampling methods.

5.1 Overview of Site and Preparation Activities

5.1.1 Site Selection

The Tijeras Arroyo Infiltration Experiment (TAIE) was located at the end of a ridge extending from the north escarpment of Tijeras Arroyo (Figure 3.3). This site was chosen for three reasons. First, the deposits exhibit textural heterogeneities which are analogous to other near-surface deposits found within KAFB due to similar depositional and pedogenic processes and histories. Second, the site was located on the end of a ridge which allows easy and safe access to the subsurface on the hill slope below the site. Finally, well-exposed continuous outcrops in the vicinity provide the opportunity to collect geostatistical data which may be integrated with the results of the infiltration test to determine expected variations and trends of hydraulic properties within this and similar deposits.

5.1.2 Monitoring Equipment

Instruments installed at the site consisted of 36 surface and 48 subsurface time domain reflectometry (TDR) probes, with attached thermocouples, 96 tensiometers paired with the 48 subsurface TDR probes, 16 "geology" tensiometers installed in specific geologic units 13 neutron access tubes. These arrays of probes were installed in a predetermined symmetrical pattern around a 2-meter diameter infiltrometer. Instrument layout was designed to minimize potential flow field shadowing from other instruments.

Additional monitoring equipment included water flow meters, water temperature sensors, air temperature probes placed in selected tensiometer casings, and a weather station. A 12-volt photovoltaic system was installed to supply power for the data acquisition systems.
An overview of instruments installed at the site is given in section 3.0.

5.1.3 Site Preparation Activities

Site preparation began in May 1995. A backhoe and bobcat were used to level the infiltration site, to excavate five trenches on the hill slope below the site to expose the geology, and to construct an access road along the ridge leading to the site. Other preparation activities included moving a semi-trailer to the site for storage, assembling a water supply system, setting up a sun shelter, and surveying two informal concrete datums at the site: one on the north side of the site near the photovoltaic system (north datum) and the other on the south side of the site adjacent to the infiltration pad (south datum) (Figure 5.2.1 & 5.2.2). All boreholes for instruments were drilled with either a Geoprobe, augered with a Big Beaver drill rig, or augered by hand. All subsurface TDR probes, tensiometers, and neutron access tube elevations were measured relative to the south datum using a Topcon Auto Level Model AT-G7 (Paramus, NJ) and a surveying rod. In this report, the infiltration surface is used as a reference datum for discussing subsurface instrument locations. This surface was defined as the height of the ground surface at the center of the infiltrometer relative to the south datum.

5.2 Infiltration Site Setup

5.2.1 Introduction

This section provides an overview of the infiltration site and a description of the instrument arrays. The locations of the trenches relative to the infiltration pad are also presented in this section.

5.2.2 Overview of Site

A staging area was located at the beginning of the access road constructed along the ridge leading to the infiltration site (Figure 5.2.1). This staging area contained four 2500-gallon reserve water tanks, a trailer for equipment storage, and the weather station.

The infiltration site was located on a ridge approximately 10 vertical meters below the Tijeras Arroyo escarpment. Details of the infiltration site are given in Figure 5.2.2, which locates trenches, all the data acquisition systems, the photovoltaic system, the infiltrometer water supply tanks and the infiltrometer supply line (including temperature probes and flow meters), the north and south infiltration site datums, the pits used to calibrate TDR probes and the neutron probe, and the shade structure.

5.2.3 Subsurface Paired TDR and Tensiometer Array

A plan view depicting the infiltrometer and the instrument arrays is given in Figure 5.2.3, and explanations of the descriptors are given in Table 5.1. All TDR probes, tensiometer porous cups, and neutron access tubes have been located in space relative to the center of the infiltrometer. depths below the south datum for each of the subsurface instruments was obtained using a transit level and a leveling rod. All plan view locations were obtained with a tape measure and angle measurements from true north using either a transit level or a Brunton compass. Instrument arrays presented in Figure 5.2.3 and Table 5.1 are described next.

The subsurface TDR-tensiometer array is comprised of 12 groups of four TDR-tensiometer pairs (TTP) **(**Figure 5.2.3 & Table 5.1**)**. Each TTP is comprised of a TDR probe, with attached thermocouple, adjacent to two pressure transducer equipped tensiometers. Each group contains four TTPs installed at different depths. In all, eight holes were augered for each group: four "inside holes" in which the TDR probes were installed, and four perimeter holes in which 8 tensiometers (two in each hole) were installed at the same depth as the associated (paired) TDR probe. All holes were augered 0.3 meters apart. All tensiometer tops are below the ground surface. A 0.35 length of 6 in. diameter Schedule 40 PVC pipe was used as a casing for the tensiometers. A circular piece of 2 in. thick open cell foam was cut to fit snugly inside the casing and glued to a 8 in. square piece of 3/8 in. plywood to provide a removable weatherproof cap. Additional insulation is provided by another 2 in. open cell foam plug sandwiched between the top of the tensiometers and the cap.

The TTP nearest to the infiltrometer and to the left, as seen from the center of the infiltrometer, is located approximately one meter below the ground surface **(**Figure 5.2.3 & Table 5.1**)**. The other TTPs in the group are located, in a counterclockwise direction from the 1-meter TTP, approximately 2, 4, and 3 meters below the ground surface, respectively. The centers of the 12 TTP groups are located in three "rings" 1.5, 2.5, and 3.5 meters from the center of the infiltrometer. These rings are referred to as the inner, medial, and outer rings, the inner being the nearest to the infiltrometer. The inner ring TTP groups are located in the primary compass directions relative to the center of the infiltrometer. The four groups in each ring are orthogonally arranged and each group is sequentially staggered counterclockwise from the inner ring TTP group. This arrangement produces four spiraling arms, each consisting of three TTP groups. The TTP groups are identified according to which spiral arm and ring they are in, and they retain the compass direction of the TTP group nearest to the infiltrometer. Thus, the north spiral arm contains the North Inner (NI), North Medial (NM), and the North Outer (NO) TTP groups.

In this report, the individual TTPs are identified according to the depth to the nearest meter at which they were installed. For example, the TTPs buried at 2 meters are identified as "the 2m TTP" and the thermocouple attached to the 2-meter deep TDR probe will be called "the 2 m TTP thermocouple". Pairs of tensiometers (tensiometers in the same hole) were installed so that one is nearer to the infiltrometer than the other to aid in identification. The tensiometer nearest the infiltrometer is the inner tensiometer

(I), while the other is the outer tensiometer (O). Thus the 2-meter deep inner tensiometer is referred to as the 2-I tensiometer.

5.2.4 Surface TDR Array

The TDR surface array consists of four orthogonal radial sets, each consisting of 9 TDR probes **(**Figure 5.2.3 & Table 5.1**)**. These probes are designated according to their trend as viewed from the center of the infiltrometer. Thus, the northeast surface set is designated NES. The probes are sequentially numbered NES1 to NES9 from the innermost probe to the outermost probe. Probes in a radial set are located approximately 0.3 meters apart and the probe nearest to the infiltrometer is located 0.3 meters from the wall of the infiltrometer.

5.2.5 Geology Tensiometers

Four groups of four transducer-equipped "geology" tensiometers were installed 2.5 meters from the center of the infiltrometer behind each one of the inner TTP groups **(**Figure 5.2.3 & Table 5.1**)**. The geology group tensiometers are designated according to their compass direction as viewed from the center of the infiltrometer. For example, the geology tensiometers located behind the NI group are designated NG. The geology tensiometer tops were also installed below the ground surface in the same manner as the TTP tensiometers.

The geology tensiometers were cut to predetermined lengths to place the porous cups within specific geologic units. Tensiometers within each group are designated by adding the numbers 1 through 4 to the designator, according to the depth of the porous cup, with 1 indicating the shallowest and 4 the deepest. For example, the shallowest tensiometer in the north geology group is designated NG1 and the deepest NG4.

The geology tensiometers targeted the three upper most units described in the trenches (see Section 4.2.3 for details about the geology). Starting with the surface, these units are as follows: Unit 7 (consisting mostly of silt and very fine sand), Unit 6 (fine to coarse sand, pebbles, and gravels), and Unit 5 (fine to very fine sand). All XG1 tensiometers were located in the middle part of Unit 7, while XG2 tensiometers were placed in the lower part of Unit 7 very near the contact with Unit 6 (X represents the missing descriptors N, E, S, or W). XG3 tensiometers were placed within Unit 6 and XG4 tensiometers were installed in Unit 5b.

5.2.6 Neutron Access Tubes

A total of 13 neutron access tubes were installed at the infiltration site **(**Figure 5.2.3 & Table 5.1**)**. Access tubes were installed in rings at 2.5, 4.5, and 5.5 meters from the center of the infiltrometer. Four tubes were orthogonally placed on each ring. The access tubes are designated according to the compass quadrant in which they are located and their distance from the center of the infiltrometer. Thus, the tensiometers in the northeast quadrant are designated NE2.5, NE4.5, and NE5.5. A neutron access tube was installed in the center of the infiltrometer and is designated CTR. The CTR and all XX2.5 tubes were installed to approximately 6 meters below the surface, while the XX4.5 and XX5.5 tubes were installed to 4 meters below the surface. (XX represents the missing descriptors NE, SE, SW, or NW.) .

5.2.7 Trenches

Trenches are designated according to the azimuth bearing of the trench as seen from the center of the infiltrometer (Figure 5.2.3 & Table 5.1). The trench with an azimuth of 125 is designated T125 with an arrow pointing in the direction of the trench.

5.3 Water Supply System

The water supply system was designed to provide a constant-head pond of water within the 2-meter diameter infiltrometer. The water supply system consisted of four reserve water tanks located at the staging area on the escarpment above the site, infiltrometer water supply tanks, a water supply line connecting the reserve and infiltrometer supply tanks, and a water delivery system from the infiltrometer supply tanks to the infiltrometer (Figure 5.2.1 & 5.2.2). Two water flow monitoring systems were implemented: a manual system which involved recording water heights in the infiltrometer supply tanks and infiltrometer, an automated datalogging system incorporating pressure transducers for recording the drop in water height in the infiltrometer supply tanks, in-line flow meters for monitoring high flow rates which were expected during early infiltration times, and a resistive water level device for monitoring water levels in the infiltrometer.

Water for the infiltration test was supplied by the Kirtland Air Force Base water supply system and obtained from a fire hydrant near the entrance to Technical Area IV. The water was transported in a 300 gallon HDPE tank via pickup truck and off-loaded to the four 2500-gallon HDPE reserve water supply tanks located on the escarpment above the infiltration site. When needed, water from the reserve tanks was drained to the two 500-gallon HDPE infiltrometer water supply tanks though a 2" diameter flexible plastic irrigation pipe (Figure 5.2.1).

5.4 Infiltrometer and Ground Surface Evaporation Barrier

The surface was covered to limit evaporation from the infiltrometer and the subsurface during and after infiltration. Details of how this was accomplished is discussed next along with a brief description of the infiltrometer construction and installation.

5.4.1 Infiltrometer and Infiltrometer Deck

The infiltrometer was constructed from three polyethylene sheets (measuring 0.4 by 2.44 meters) bolted end-to-end to provide a 2-meter diameter infiltrometer. The infiltrometer was installed in a 15-cm deep oversized trench and backfilled with an uniform mixture of 50% powdered bentonite and 50% sifted sand. A cover for the infiltrometer was constructed from 3/4 inch plywood and was supported by a Unistrut frame (Figure 5.4.1). The deck was sealed with fiberglass resin. Several layers of 3/8" by 3" weather stripping provided a water-tight seal between the infiltrometer and the deck. A weather-tight hatch located in the center of the deck allowed access inside the infiltrometer. Four heavy duty 3/4 inch brass stock tank float valves mounted on a 2" diameter PVC pipe manifold were fastened to the top of the deck. A short piece of garden hose (one for each valve) was inserted through tightly fitting holes drilled in the deck and connected to the valve spigot. Floats were attached to the valves by feeding pivot arms through slots cut in the deck. Duct tape loosely placed on the slots and float arms provided a seal without inhibiting the movement of the arms. A 3-sided cover constructed out of 3/8 in. plywood was installed to cover the valves, to assure that water from rain storms would not enter the infiltrometer (Figure 5.4.1).

5.4.2 Ground Surface Evaporation Barrier

Evaporation from the subsurface and infiltration from precipitation were prevented by a vapor barrier consisting of two polyurethane ground tarps. The first tarp was spread across the infiltration site and holes were cut for the infiltrometer, tensiometer casings and neutron access tubes. The tarp was then pushed to the ground and sealed to the protruding objects with thick roofing tar. This tarp was then covered with 0.1 to 0.15 m of dirt. The second tarp was installed in the same manner and was also covered with 0.1 to 0.15 m of dirt. The area covered by the evaporation barrier is shown in Figure 5.2.3.

5.5 Data Acquisition and Reduction Overview

Most data at the TAIE were collected by one of two types of automatic data acquisition systems: data loggers and laptop computers. Water flow, water temperature, thermocouple, tensiometer, and weather station systems were controlled by data loggers that stored data in removable storage modules. Data from these systems were uploaded from the data storage modules to a laptop computer in the field and transferred to a personal computer (PC) for reduction. Laptop computers controlled the TDR systems and all data were stored on the hard drives. Data were transferred to floppy disks in the field and then transferred to a PC for reduction. Two sets of manual data were also collected at the TAIE: water flow data obtained by recording water levels in the water tanks and infiltrometer, and neutron probe data. Manually collected data were recorded on forms and reduced on PCs. All data collection times were converted to "time relative to start of infiltration (Days)" (TRSI) during data reduction procedures. On all plots of data versus time, time implies TRSI. Selected data sets are presented and briefly discussed in Section 6.0.

5.6 Water Flow Monitoring Systems

5.6.1 Introduction

The water flow system incorporated in-line supply tank pressure transducers for monitoring water heights, flow meters installed in the infiltrometer supply line, and a resistive water level device mounted in the infiltrometer. Water heights in the supply tanks were also obtained manually.

5.6.2 Description of System

The automatic water flow monitoring system used a data logger to monitor the following equipment:

1. Six differential pressure transducers installed in each of the two infiltrometer water supply tanks to record changes in water levels with one in each tank held in reserve (Figures 5.6.1),
2. Four flow meters installed in series in the infiltrometer water supply line (Figure 5.2.2), and
3. A resistive water level sensing device to monitor the water level in the infiltrometer (Figure 5.6.2).

A complete description of water flow monitoring components is given in Table 5.2.

Manually obtained data included those obtained by logging water levels (and times) in the infiltrometer water supply tanks as well as in the infiltrometer. Measurements were recorded at the beginning and end of each refill cycle and between refills.

5.6.3 Calibration Method

The pressure transducers were calibrated in the laboratory using a 2-meter manometer. A pressure pump and the pressure transducers were connected to one end of the manometer. A multiplexed data logger system was used to obtain millivolt readings from the pressure transducers. Pressure in the system was increased in 20 consecutive steps over 2 m. At each step millivolt readings were obtained from the multiplexed data logger and water heights were read off of an adjacent tape measure. Linear regression of the millivolt data versus centimeters of water height provided a slope and intercept for each pressure transducer.

The flow meters required no calibration. A multiplier was provided by the manufacturer that allowed the raw data to be converted into liters per minute within the data logger.

The distance from the bottom of the resistive water level device to the infiltration surface was measured and accounted for during data reduction.

5.6.4 Installation Method

A PVC pipe assembly provided a method for placing the pressure transducers in the bottom of the infiltrometer supply tanks while protecting the electrical connectors from moisture and allowing atmospheric-pressure head differentials to be measured. Two pressure transducers were installed in each "arm" of a tee, and the "leg" of the tee was cemented to a 1 in. diameter PVC pipe 1.5 m in length (Figure 5.6.1**)**. Each pressure transducer was cemented into a hole drilled through a plug at the end of the arm leaving the other pressure transducer port free. The pressure transducer wires and two 1/8 in. I. D. plastic tubes connected to the free transducer ports were run back through the pipe. The transducer end of the assembly was then placed in the bottom of the supply tank with the other end of the pipe extending above the top of the tank. The wires were connected to the data logger with extension cables incorporating weatherproof connectors. Two of these assemblies (a total of 4 pressure transducers) were installed in each tank.

The four flow meters were installed in series just before the infiltrometer float valve manifold. The 2 in. diameter PVC supply line was reduced to 1 inch to accommodate the flow meter fittings. The line was enlarged to 2 inches to accommodate the float valve manifold.

The resistive water level device was installed vertically in the infiltrometer so that water would be in contact with pairs of pins. A hole drilled in the deck within the area covered by the deck roof accommodated the cable for the infiltrometer water level device. The water level device was fastened to the neutron access tube with a mounting bracket and stainless steel hose clamps.

Water levels in the infiltrometer water supply tanks could be seen easily through the translucent HDPE material. Water levels in the tanks were measured with two aluminum meter sticks placed end-to-end and taped vertically on the east and west infiltration tanks.

5.6.5 Data Reduction

The raw data file was uploaded to a personal computer and accessed by a Basic program which, 1) converted millivolt readings from the infiltrometer water level device into infiltrometer water level above the infiltration surface and, 2) saved it in a new data file containing flow meter and pressure transducer data. This new file was then imported into a spreadsheet where raw millivolt pressure transducer data from the supply tanks were converted to cm of water through linear regression coefficients. The flow meter data did not require conversion. This final file was imported into a graphing program where plots of flow rates from the flow meters, heights of water in the infiltrometer supply tanks, and water levels in

the infiltrometer were plotted versus time.

Manually collected data included water heights in the infiltration supply tanks and water heights in the infiltrometer along with the time of the readings. These data were entered into spreadsheets where infiltration rates and cumulative infiltrated volumes were calculated. The cumulative infiltration data were then imported into a graphing program and plotted versus time.

5.7 Water Temperature Monitoring System

5.7.1 Introduction

The water temperature monitoring system provided data on water temperature in the supply line and the infiltrometer, and air temperature within the infiltrometer.

5.7.2 Description of System

The water temperature monitoring system consisted of a data logger and eight temperature probes. Pairs of temperature probes were installed at the following locations:

1. In the water line close to the infiltrometer water supply tanks,
2. In the water line between the flow meters and the float valve manifold,
3. In the infiltrometer above the water line, and
4. In the water in the infiltrometer.

Complete descriptions of the temperature monitoring components are given in Table 5.3.

5.7.3 Calibration Method

The temperature probes used in this system did not require calibration. A multiplier provided by the manufacturer, converted millivolt readings to degrees Celsius.

5.7.4 Installation Method

Two 2-inch PVC tees were used to install the two pairs of temperature probes in the infiltrometer supply line. A PVC internal reducer was cemented into the "leg" of each tee. Two temperature probes were fed into each reducer and located so that the probes would be in the stream of water, but not touching the walls of the tee. The probes were taped to the reducer to hold them in place and to prevent leakage of epoxy during the next step. The tee was clamped in a vice with the "leg" facing down and epoxy was poured into the reducer from the inside of the tee. The tee was not removed until the epoxy was cured. The tees were installed in straight sections of the water supply line in two locations: one near the infiltrometer supply tanks and the other between the flow meters and the float valve manifold (Figure 5.7.1). Portions of the supply line were either buried in a trench or covered with dirt to help moderate temperature swings.

The two pairs of temperature probes were installed in the infiltrometer by drilling holes in the area of the deck protected by the raised roof and inserting the probes through the roof. The air temperature pair was suspended above the expected ponded surface and bonded in place with epoxy, while the water temperature pair was allowed to lay flat on the infiltration surface.

5.7.5 Data Reduction

The raw data file was imported into a spreadsheet where the time format was changed to time. This new file was then imported into a graphing program where the temperature data were plotted versus time.

5.8 TDR Systems

5.8.1 Introduction

Eighty-four time domain reflectometry (TDR) probes were installed in surface and subsurface arrays to track the wetting front advance and measure soil moisture contents. Data from the probes were collected using three separate automated data acquisition systems. Section 5.2.3 gives a complete description of the TDR arrays.

5.8.2 Description of System

Three TDR data acquisition systems were used to monitor the arrays of TDR probes. All three systems incorporated a laptop computer, Tektronix signal generator and either 16- or 24-port multiplexers. Two identical systems monitored the 48 subsurface probes through a 24-port multiplexer, while the third monitored the 36 surface probes through three 16-port multiplexers incorporating a four-port signal splitter. Specific equipment details are given in Table 5.4. Weather-tight enclosures provided protection from the elements for all three systems (Figure 5.8.1).

TDR probes were constructed out of 0.8 cm (5/16 inch) by 15 cm (6 inch) stainless steel rods, polycarbonate blocks, and Alpha RG58-A low noise coaxial cable (Figure 5.2.2).

5.8.3 Calibration Method

The TDR probes were calibrated in a pit excavated in the hillside adjacent to the infiltration site Figure (5.2.2) to expose undisturbed silts and fine sands of Unit 6 (See Geology Section 4.2.3). Several days elapsed after cessation of excavation activities and before installation of the TDR probes to allow the soil to dry out. An array of 24 TDR probes was installed in the pit floor. Soil samples were collected adjacent to TDR probes with brass sample rings that were pressed into the ground and carefully removed to assure that the ring was fully filled with sample. All rings were capped with plastic caps and taped with electrical tape immediately upon removal from the pit. The volumetric moisture content was determined using standard laboratory procedures. An initial suite of samples and corresponding data from the probes were collected before flooding the pit. Five additional suites of samples were collected over a period of several weeks during drying of the pit.

Moisture content data were linearly regressed against dielectric data from the TDR probes to obtain a linear equation relating the soil moisture content as a function of the dielectric constant. In a comparison with results from the well-known Topp equation (Topp et al. 1980), the regression results yielded a better fit as indicated by R squared values (Figure 5.8.2).

5.8.4 Installation Method

All TDR probes were driven into undisturbed material at the bottom of boreholes. A rubber mallet was used to seat the surface probes in the bottom of shallow holes. A sledge hammer and a "TDR probe installer" consisting of extensions of 36 in. lengths of 1/8 in. thick walled square steel tube were used for seating the subsurface probes. A plate was welded on one of the extensions to provide a seat for holding the TDR probe during installation. Each probe was checked for operation before and after installation. Once installed, depth readings to the top of the probe were taken with a transit and survey rod (Section 5.1). Approximately 800 cc of sifted dirt from the site was poured over the top of the probes. All holes were completely backfilled with a uniform mixture of 25% powdered bentonite and 75% sifted dirt from the site. The surface TDR probe holes were backfilled with dirt from the site.

5.8.5 Data Reduction
Data were transferred from floppy disks to PCs and reduced using spreadsheet macros. The reduced data were then imported into a graphing program where calculated moisture contents were plotted versus time.

5.9 Neutron Probe Moisture Measurements
5.9.1 Introduction
A neutron moisture probe was used to monitor the wetting front advance about an array of access tubes at the site. The neutron moisture measurements presented in this report are limited to qualitative data on wetting front advance rather than estimates of actual moisture contents.

5.9.2 Description of System
Readings were taken from an array of 13 access tubes (Figure 5.2.3) at 0.3 m depth intervals "stops" prior to and after wetting front arrival. Raw count readings were recorded at each stop and for each tube.

5.9.3 Calibration
Calibration of the neutron probe has not been completed and will not be discussed in this report.

5.9.4 Installation Method
A hole was bored in the center of the infiltrometer with a 3.25 in. diameter auger while all other neutron access tube holes were made with a 2.75 in. diameter auger. All of the 2.5 m (installed 2.5 m from the CTR access tube) and the center of infiltrometer (CTR) access tubes were installed to approximately 6 m below the ground surface while the 4.5 and 5.5 tubes (installed at 4.5 and 5.5 m from the CTR access tube, respectively) were installed to approximately 4 m depth. The tops of all of the tubes were installed at the same height that was measured relative to the south datum (Section 5.1). Installation was completed after filling the space between the neutron access tubes and the wall of the hole with 100% powdered bentonite.

5.9.5 Data Reduction
All readings were manually logged and entered in a preexisting spreadsheet where stop numbers were converted to depths below the infiltration surface. The updated spreadsheet was then imported into a graphing program where raw count values were plotted on the X-axis and depth below the infiltration surface was plotted on the Y-axis.

5.10 The Pressure Field
5.10.1 Introduction
The pressure field monitoring system incorporated multiplexed data loggers that monitored two arrays of tensiometers. One array included 96 tensiometers paired with 48 TDR probes (two tensiometers per TDR probe) arranged in rings around the infiltrometer. The other array included 16 tensiometers installed at four locations across the site (four tensiometers per "geology" hole) and targeted specific geologic units. Sections 5.2.3 and 5.2.5 discuss the tensiometer arrays in detail.

5.10.2 Description of System
Four separate data acquisition systems were used for the tensiometers, three of which were used to monitor the inner, medial, and outer ring TTP groups (one for each ring), and the fourth to monitor the 16 geology tensiometers. Table 5.5 gives details on the equipment used to monitor the tensiometers. Tensiometers were constructed in the laboratory by SNL/NM. Materials used in the construction of the tensiometers are specified in Table 5.5 and a schematic of a tensiometer is given in Figure 5.10.1.

5.10.3 Calibration

The pressure transducers were calibrated in the laboratory via an inverted U manometer measuring 7 m in height. A vacuum pump and 10 to 13 pressure transducers were connected to one end of the manometer while the other end was submerged in a 5 gallon bucket of water. The transducers were connected to one of the multiplexed data logger systems with a 40 ft extension cable duplicating all connectors and data acquisition equipment to be used in the field (Table 5.5). Vacuum in the system was increased in 20 consecutive steps to over 6.5 m. At each step millivolt readings were obtained from the multiplexed data logger and water heights were read off of an adjacent tape measure. The vacuum was then decreased to 0.0 m in the same number of steps, and millivolt and height readings were obtained again. This cycle was repeated two more times. Linear regression of the millivolt data versus water height measured in centimeters provided a slope and intercept for each pressure transducer. Faulty pressure transducers were identified by R^2 values significantly less than 0.95. All of the pressure transducers used at the TAIE had R^2 values greater than 0.95.

5.10.4 Installation Methods

All tensiometers were tested in the laboratory prior to field installation. Tensiometer testing involved filling the tensiometers with water, capping off one end, and monitoring vacuum in the tensiometer with a multiplexed data logger. Evaporation of water from the porous cups results in a continuously increasing vacuum in the tensiometer until the air-entry value of the porous cup is exceeded. At this time the vacuum drops sharply and the tensiometer "fails". Leaks at cemented joints are a common cause for premature tensiometer failure. Tensiometers that failed before reaching -600 cm of water were not used at the TAIE.

Tensiometer installation proceeded after the casings were installed and the holes were bored to the desired depth (see Section 5.2.3 and 5.2.5 for a description of the casing and layout of tensiometer holes). Depths of holes were measured with the surveyor's level and surveying rod relative to the south datum. Each tensiometer was drained and partially refilled with 50 ml of water and tensiometer transducers were connected to the data logger before installation. Silica flour was mixed with water to form a slurry. Approximately 800 cc of silica flour slurry was poured in the hole immediately before installing the tensiometers (two each per hole in the TTP array, and four per hole in the "geology" hole, each at a different depth). After the tensiometers were gently pushed into the silica slurry, 500 cc of sifted dirt from the site was poured into the hole. All holes were backfilled with a uniform mixture of 75% powdered bentonite and 25% sifted dirt. The TTP tensiometer holes were backfilled with the bentonite mixture to the surface, while the geology holes were backfilled to the next desired tensiometer location. Additional tensiometers were installed in the geology holes using the same procedure as above. After installation all tensiometer/transducers were checked for correct connection sequence to the data loggers and for correct operation.

Tensiometers were not filled with water until data from paired TDR probes indicated the wetting front had arrived. The post-wetting-front-arrival filling of the tensiometers precluded the possibility of tensiometer failure, which, due to draining of water from the tensiometer, may have resulted in an expanding bulb of moisture intersecting the adjacent TDR probe.

5.10.5 Data Reduction
The raw data files were entered in a spreadsheet where raw millivolt readings from pressure transducers were converted to cm of water through linear regression coefficients. The new data were appended to an existing file containing earlier data. This updated file was then imported to a graphing program to create plots of the pressure transducer data versus time.

5.11 The Thermocouple System
5.11.1 Introduction
An array of thermocouples was installed to monitor subsurface soil temperature changes resulting from infiltration. Thermocouples were taped to each of the TDR probes in the TTP. Air temperatures inside tensiometer casings were also monitored with this system. Section 5.2.3 gives a description of the TTP and thermocouple arrays. Table 5.6 gives details on the equipment used to monitor the thermocouples.

5.11.2 Description of System
The thermocouple system consisted of 48 thermocouples and 8 air temperature probes connected to a multiplexed data logger. Air temperature probes were installed to monitor the air temperature in selected tensiometer access casings. The data logger, multiplexer, and data storage module were protected from the elements inside an equipment enclosure, which in turn was enclosed with a silicone-sealed, foam-insulated plywood box.

The system was designed to measure temperature in degrees Celsius (°C). According to the manufacturer the limits of error of the thermocouples are 1.0 °C or 0.75% above freezing and 1.0 °C or 1.5% below freezing.

5.11.3 Calibration
No calibration of the thermocouples or temperature probes was needed. All raw data were stored as temperature in degrees Celsius.

5.11.4 Installation Technique
The thermocouples were installed along with the TTP TDR probes (Table 5.1). Thermocouple wires were tied together in groups and buried in shallow trenches. The air temperature probes were installed in the air space within tensiometer casings.

5.11.5 Data Reduction
The raw data file was imported into a spreadsheet where the time was converted to TRSI. This file was then uploaded to a graphing program where plots of temperature versus time were created.

5.12 The Weather Station
5.12.1 Introduction
A weather station was installed at the site to measure a variety of climatic conditions present at the site. Weather station data may be used to make adjustments to data that are influenced by ambient temperature and pressure fluctuations. This section describes the weather station equipment and installation.

5.12.2 Description of System
The weather station consists of a data logger, a 2 m tall tripod, and a variety of instruments for collecting climatic data. A complete list of the weather station equipment is given in Table 5.7.
The data logger was programmed to provide the air temperature data in degrees Celsius (°C), the relative humidity in percent, the barometric pressure in millimeters of mercury, and the precipitation in millimeters. Data collected from the other equipment listed in Table 5.7 will not be covered in this report.

A solar panel and a 12-volt marine battery provided power for the weather station.

5.12.3 Calibration
No special calibrations were needed for any of this equipment. All instruments came factory-calibrated and ready for field use.

5.12.4 Installation Technique
The weather station was installed on the escarpment above the TAIE (Figure 5.2.1). The location was selected because it was near the site, but not so close as to have weather readings adversely impacted by site activities and local topography. In general, all equipment was mounted on or near the tripod in accordance with Campbell recommendations. The air temperature/relative humidity probe was installed about 6 ft above the ground surface inside the radiation shield. The barometric pressure sensor was installed inside the Campbell enclosure (about 4.5 ft above the ground surface). The rain gage was installed on its own stake about 4 ft high and 16 feet west of the tripod. The entire weather station area was roped off and posted.

5.12.5 Data Reduction
The raw data files were loaded into a spreadsheet program where the barometric pressure was converted from millimeters of mercury to centimeters of water. Data were plotted using a graphing/plotting program.

5.13 Soil Sample Collection
5.13.1 Introduction
Five sets of soil samples, each set employing different sampling methods, were collected during the site preparation and instrumentation phase of the project. These samples provided initial gravimetric and volumetric moisture contents, saturated and unsaturated hydraulic properties, as well as information required for constructing geologic cross-sections. An overview of the sampling methods and data obtained from each sample set follows.

5.13.2 Samples Used for Hydraulic Properties
Thirty-four "undisturbed" samples were collected from the trenches in Units 4 through Unit 7. These were incased in a 3.5 cm high by 6 cm diameter brass ring with expanding insulation foam. Moisture characteristic curves, saturated hydraulic conductivity, and bulk density have been obtained from 14 of these samples at the Hydrology Laboratory (Organization 7584) at the time of this report.

5.13.3 Samples Used for Initial Moisture Contents
While boring the geology holes, thirty samples were collected at 0.3 m intervals using a split spoon sampler that incorporates removable brass sample rings. All sample rings were capped and taped with electrical tape immediately after removal from the sampler. Gravimetric moisture contents were obtained from these samples as well as volumetric moisture contents when samples remained intact so that reliable bulk density measurements could be made.

Thirty-seven additional grab samples were collected while boring for the XX4.5 neutron access tubes. These samples were collected at .5 m intervals and placed in brass sample rings as they were removed from the auger. The sample rings were capped and taped with electrical tape.

5.13.4 Samples Used for Geologic Cross-section Construction
Samples were collected using a truck-mounted hydraulically powered percussion soil-probing unit

that incorporates a 1.5" inside diameter by 48" long continuous core sampler with a removable clear acetate lining (i.e., a geoprobe). These continuous core samples were collected from the twelve 4 m TTPs, the four XX2.5 neutron access tubes and the CTR access tube. These samples remained in the acetate liner and provided distances from the surface to each of the geologic units identified in the trenches. The geoprobe samples are identified according to which TTP group they came from (see section 5.2.3) with the suffix 4C (where C indicates the hole is located on a corner of a group) appended to the group abbreviation. Thus, the core sample from the North Outer group is designated NO4C.

Continuous core "grab" samples from the holes used for the geology tensiometers (see Section 5.2.5), collected during boring, augment data from the geoprobe samples. These samples were collected by using a length of 2" diameter PVC pipe cut in half lengthwise to provide a casing for grab samples removed from the auger. One end of the PVC pipe was marked "top" which corresponded to the ground surface. Samples were placed in the half-sections of PVC at distances from the top that corresponded to the sample collection point below the ground surface. Once filled, the two halves were taped together and transported without disturbing the sample.

6.0 RESULTS AND DISCUSSION

Selected data from the TAIE are presented in this section. All instrument arrays discussed below are described in detail in Section 5.2 while descriptions of the data acquisition systems and installation methods are presented in Section 5.5 through 5.12.

6.1 Water Flow Results

6.1.1 Introduction

In this section we present selected results from the water flow systems described in Section 5.6. Manual water height readings and pressure transducers data from the infiltration supply tanks are presented. Data from the flow meters and infiltrometer water level device will not be covered.

6.1.2 Manually-Collected Infiltration Data

Infiltration rates and cumulative infiltration were calculated from manually collected water height data from the infiltrometer supply tanks. Graphs of infiltration rates, starting 6 hours after the beginning of the infiltration event, and cumulative infiltration data are presented in Figures 6.1.1 and 6.1.2, respectively. Infiltration rates appear to increase from approximately 0.5 to 0.9 m^3/day during the first 12 days of infiltration, after which the infiltration rates appear to level off. Approximately 24 cubic meters (about 6300 gallons) of water were applied between 1500 hours on Tuesday, November 7, 1995 and 0950 hours on Monday, December 4, 1995.

6.1.3 Infiltrometer Supply Tank Pressure Transducer Data

Water height data from a pressure transducer located at the bottom of each tank are presented in Figure 6.1.3. Water was primarily supplied to the infiltrometer from the east supply tank that was refilled every other day. Water was supplied to the infiltrometer from the west tank only when refilling the east tank. The only exception to this occurred on day 24 when water was inadvertently supplied to the infiltrometer from the west tank for approximately 10 hours.

6.2 TDR Moisture Results

6.2.1 Introduction

This section provides selected TDR system results. Three TDR systems, described in Section 5.8, were used to measure soil moisture contents before, during, and after the infiltration period. The data presented here are representative of data from other locations. A brief discussion of the results is given.

6.2.2. TDR Moisture Data

Figures 6.2.1, 6.2.2, 6.2.3, and 6.2.4 are plots of volumetric moisture contents versus time obtained from TDR probes installed in the North Inner (NI), North Medial (NM), North Outer (NO), and Northeast Surface array (NES), respectively. Wetting front arrival times are marked by an increase in moisture content from the initial condition, and some probes (such as NI2, NM2, and NO1) may be recording a slight drop-off in moisture content after infiltration ceased on day 26.

6.2.3 Discussion

Three irregularities are readily apparent on the plots. First, initial volumetric moisture contents vary from an unrealistic value just below 0.0 to approximately 15%. Possible explanations for the observed variability include the following:

1. Mineralogical variability within the soils at the site may affect TDR readings to the point that a unique set of calibration coefficients must be determined for each type of material,
2. Some of the TDR probe prongs may have been bent during installation thereby producing unreliable readings, and
3. Water from rainstorms entered the instrument holes before they were refilled with bentonite.

The negative values obtained from some probes suggest either a calibration problem or damage to the probe. However, introduced water from rainstorms cannot be discounted as a cause for some of the observed variability. Additional TDR calibration studies may resolve this issue.

A second area of concern is the unrealistically high moisture content values exhibited by some probes shortly after arrival of the wetting front. One plausible explanation for these peaks is that the wetting front mobilizes soluble ions that cause the signal attenuation observed in the data. As a result, moisture contents are overestimated during analysis. Because realistic moisture contents usually return within one or two days with continued infiltration, the soil must contain limited quantities of soluble minerals that are apparently flushed from the system with continued infiltration.

6.3 Neutron Probe Results

6.3.1 Introduction

A neutron probe was used to measure soil moisture content in 13 access tubes at the site. The neutron probe was used during the pre-infiltration period to establish baseline moisture contents and to monitor changes prior to infiltration. Because the neutron access tubes were installed with a backfill of bentonite mix (Section 5.9), existing calibration data could not be used to obtain moisture contents. Therefore, only raw neutron count data are presented in this report.

6.3.2 Neutron Count Data

Neutron count data from four access tubes (Center (CTR), NE2.5, NE4.5, and NE5.5) are presented in Figures 6.3.1 to 6.3.4, respectively. The data presented here are representative of data from the other access tubes. The legend for Figures 6.3.1 to 6.3.4 is given in Figure 6.3.5

6.3.3 Discussion

Figures 6.3.1 and 6.3.2 show neutron counts from the center and NE2.5 access tubes, respectively. These data start 88 days before the start of infiltration and end 70 days after the start of infiltration. These profiles illustrate the continual downward movement of the wetting front with time. In contrast, raw counts from the NE4.5 and NE5.5 access tubes show that the lateral movement of the wetting front was greatest in a zone approximately 1.5 to 2.75 m below the surface. The region in which this lateral movement occurred consists of fine to coarse sands with some gravels. This coarse layer is bounded on the top and bottom by finer-textured materials (see section 4.2 for a description of the site geology).

6.4 Pressure Field Results

6.4.1 Introduction

Pressure transducer-equipped tensiometers (Section 5.10) were used to measure soil tensions during the infiltration experiment. The tensiometers were filled when the arrival of the wetting front was indicated by data from the adjacent (paired) TDR probe. The decision to fill the geology tensiometers was based on data from adjacent neutron access tubes.

6.4.2 Tensiometer Data

The tensiometer data presented here include data collected from 26 to 70 days after the start of infiltration. All tensiometer data presented here have been converted from raw millivolt data to centimeters of water using calibration coefficients. As such, the data give the potential at the pressure transducers. Figures 6.4.1 through 6.4.4 show results from the North Inner (NI), North Medial (NM), and North Outer (NO) TTP groups and the North Geology (NG) tensiometers, respectively. Periods of misreading occurred due to condensation build-up within the connection between the pressure transducer and the extension cable. These connectors were located in the tensiometer casings and were exposed to

high humidity, especially after arrival of the wetting front.

6.4.3 Discussion

Six tensiometers (three pairs with each pair installed in the same hole at the same depth) from the NI group were phased in during infiltration (Figure 6.4.1). They include the 1 m, 2 m, and 3 m pairs with the porous cups installed approximately 1, 2 and 3 meters below the ground surface, respectively. Data from the 4 m pairs have not been included here because they were not filled during the 44-day time period covered in this report. A discussion of the data presented in Figure 6.4.1 follows.

The data are grouped into three pairs showing markedly different potentials. Each pair contains data from two tensiometers installed in the same hole at the same depth. The uppermost pair of curves are from the 1 meter deep tensiometers, the middle pair from the 2 meter tensiometers, and the lowest from the 3 meter tensiometer pairs. This is consistent with the fact that the pressure transducers are measuring both the capillary potential of the water in the soil and the pressure potential from the hanging column of water in the tensiometers. Consequently, the longer the tensiometer, the longer the column of water, and the more negative the reading. Capillary potential data from all of the tensiometers can be used to develop 2 and 3-dimensional pressure fields across the site.

The data presented in Figure 6.4.1 include approximately 12 hours of observations collected before infiltration halted, which is marked by a sudden drop in the pressure transducer potential near the end of day 26. Initially, the pressure potential drops off quickly and, with time, attenuates. The initial pressure drop with time also appears to be greatest in the tensiometers nearest the infiltrometer.

Tensiometer pairs in the NM and NO TTP groups (Figures 6.4.2 and 6.4.3) as well as the NG tensiometers (Figure 6.4.4) share similarities with the NI tensiometer. Paired tensiometers can be identified (where all data are present) and the pressure drop is initially rapid and attenuates with time. Additionally, the initial rate of decrease in pressure in the tensiometers nearest the infiltrometer appears to be greater than that of tensiometers located further away. The pressure potential appears to be increasing in the NO group until infiltration halts and the trend is reversed. This reversal in trend can also be observed with careful inspection of the NI and NM tensiometers.

The differences in readings from the paired tensiometers are probably due to incorrect intercept coefficients in their calibration curves because the paired tensiometers are installed in the same hole and at the same depth. This error may be due to the slight differences in cable length and resistance across the connectors between the cable used for calibration and the cable used in the field.

6.5 Thermocouple Results

6.5.1 Introduction

The thermocouple system described in Section 5.6.5 monitored subsurface soil temperatures before, during, and after infiltration. Data are available from July 25, 1995 through January 15, 1996 (105 days before the start of infiltration to 70 after ending infiltration), during which time only a few relatively short periods of data are missing. Data were collected every half hour except for a period early in the infiltration event when data were collected every 15 minutes. In this report data are presented from 11 days before start of infiltration to 70 days after the start of infiltration.

6.5.2 Thermocouple Data

The thermocouple system consisted of 48 thermocouples attached to the TTP TDR probes. Of these 48

probes, 7 malfunctioned for unknown reasons. Thermocouple results from the 1 m, 2 m, 3 m, and 4 m probes are presented in Figures 6.5.1 through 6.5.4, respectively.

6.5.3 Discussion

Diurnal temperature fluctuations of approximately 1 degree Celsius are observed in all thermocouple data. The temperature swings appear constant with depth and no lag time in peaks is observed between probes at different depths. These observations suggest that the diurnal swings are an artifact from the data acquisition system. Thermocouple temperatures are measured relative to reference thermistors located on the multiplexer and the datalogger panel. Data from these thermistors recorded diurnal temperature swings in the enclosures. Attempts to reduce the diurnal temperature fluctuations by insulating the thermocouple enclosure met with limited success.

Thermocouple data presented in this report show a consistent cooling trend while data taken during the summer months (these data are not presented here) show a consistent warming trend. Comparisons among Figures 6.51 through 6.63 show that the probes nearest the surface recorded larger temperature changes than deeper probes.

Arrival of the wetting front at each of the probes seems to be recorded in the thermocouple data. Wetting front arrival is correlated with temperature data that gradually deviate from the established trend. The deviations of data from individual probes have been correlated with wetting front arrival data at the associated TDR probes. Data from some of the probes reach a minimum value about the time that infiltration halted (26 days after the start of infiltration). Other data more or less follow the previous trend but are offset to one side or the other. One probe in the 4 m group deviated significantly away from previous readings after the infiltration period. The fact that the temperature data from all probes do not consistently increase or decrease suggests that another factor other than temperature may be affecting the readings.

6.6 Weather Station Results

6.6.1 Introduction

The weather station described in Section 5.6.6 was used to measure and record a variety of site weather conditions before, during, and after infiltration. In this report, ambient air temperature, barometric pressure, rainfall, and relative humidity data are presented. In general, data are available from July 25, 1995 through January 15, 1996 (105 days before the start of infiltration to 70 days after the end of infiltration). Although there are some early periods for which data are not available, the data set is complete between September 5, 1995 and January 15, 1996. Weather data were collected hourly during the entire period. Data presented here include the period from 70 days before infiltration to 70 days after the start of infiltration.

6.6.2 Weather Station Data

Air temperature data are shown in Figure 6.6.1. During the study period the air temperature ranged from about -10 to 35 Celsius. Barometric pressure data are shown in Figure 6.6.2. The barometric pressure ranged from about 838 to 864 centimeters of water. This small range in barometric pressure may be due to a conversion error. Precipitation data are shown in Figure 6.6.3. Twenty measurable rainfall events occurred during the study period. The largest of these events was 14 mm on September 7, 1995. No measurable events occurred during the infiltration period. Relative humidity data are shown in Figure 6.6.4. Relative humidity ranged from about 8% to 100%.

The four soil temperature probes and the wind speed sensor did not function.

6.7 Soil Sample Results

Soil sampling methods and locations were described briefly in Section 5.13. Data obtained from the soil samples included gravimetric and volumetric moisture contents, and bulk density.

Table 6.1 contains soil sample data obtained from the geology boreholes. Each of these samples was analyzed for gravimetric moisture content. When a reliable bulk density measurement of a sample was possible, volumetric moisture content was also calculated. Table 6.2 provides gravimetric moisture content values from soil samples obtained during the installation of the 4.5 meter neutron access tubes.

7.0 NUMERICAL STUDIES

This section describes numerical predictions of the infiltration process for the TAIE made using a finite difference Richards equation solver capable of simulating both non-hysteretic and hysteretic situations.

7.1 Theoretical Background

Prediction of water flow and solute transport in vadose zones requires solving coupled unsaturated flow and advective transport equations. The equation for flow through unsaturated porous media is known as the Richards equation. Because of the highly non-linear nature of the Richards equation, numerical techniques are typically used to arrive at a solution. The most popular numerical methods are the finite difference and finite element approaches. The finite difference approach was used in our current study and is discussed below.

The importance of soil hysteresis effects are recognized in studying subsurface flow phenomenon at ER sites. Many experiments have been performed to examine hysteretic flow behavior in soils. The experiments performed by Topp and Miller (1966) on glass-bead material, Topp (1969) on silty loam, Topp (1971) on sandy loam, Vachaud and Thony (1971) on sand, Dane and Wierenga (1975) on layered clay loam on top of sand, and Gillham et al. (1976) on dune sand are a few examples of the observed hysteresis of soil moisture content.

Since the advent of electronic computing, many soil scientists and hydrologists have used numerical methods to model the effect of soil-water hysteresis. Unfortunately, computing limitations have limited many historical calculations to one-dimensional gravity-driven flows. One-dimensional models, however, have provided interesting results. The numerical simulations clearly demonstrate the discrepancies which arise if hysteresis is ignored. Kaluarachchi and Parker (1987) performed a series of finite element simulations of flow in one- and two-dimensional unsaturated soils. They showed effects of hysteresis for one-dimensional analyses are markedly influenced by surface boundary conditions and to a lesser extent by initial conditions. Furthermore, the authors demonstrated that predicted soil water changes for two-dimensional problems were much higher for non-hysteretic simulations than for hysteretic simulations. Jones and Watson (1987) simulated the effect of soil water hysteresis on solute movement during intermittent leaching. They determined that when hysteresis data are included in the analysis, the solute mass profiles indicate that the solute moves through the soil profile in a series of well-defined peaks. This is in noticeable contrast to the situation in which hysteresis is neglected. For this case, the well-defined peaks disappear after the first infiltration event, and the solute becomes more uniformly distributed deeper in the profiles.

7.1.1 Governing Equations

The partial differential equation describing fluid flow, in partially saturated porous media, is known as the Richards equation. Richards equation is a modification to Darcy's law as proposed by Buckingham in 1907. Richards equation can formally be written as:

$$\frac{\partial \theta}{\partial t} = \nabla \bullet \left[K(\theta) \nabla (\psi + z) \right] = \nabla \bullet \left[K(\theta) \nabla \psi \right] + \frac{\partial K(\theta)}{\partial z} \qquad (7.1)$$

where, θ is the soil moisture content, $K(\theta)$ is the soil hydraulic conductivity, ψ is the matric pressure potential, and z is the vertical direction. The left hand side of Equation (7.1) shows the variation of

moisture content as a function of time. On the other hand, the right hand side contains the spatial derivatives of matric potential and the hydraulic conductivity. It is customary to rewrite the transient portion of Richards equation in terms of the pressure potential. Using the chain rule, we can write:

$$\frac{\partial\theta}{\partial t} = \left(\frac{\partial\theta}{\partial\psi}\right)\left(\frac{\partial\psi}{\partial t}\right) = C(\theta)\frac{\partial\psi}{\partial t} \tag{7.2}$$

where, $C(\theta)$, the slope of the θ-ψ relationship, is known as the water capacitance function. Therefore, the vector form of the Richards equation, in terms of matric potential becomes:

$$C(\theta)\frac{\partial\psi}{\partial t} = \nabla \bullet \left[K(\theta)\nabla\psi\right] + \frac{\partial K(\theta)}{\partial z} \tag{7.3}$$

Equation (7.3) represents the general vector form of the Richards equation. For our applications, we are interested in the two-dimensional axisymmetric cylindrical form of this equation. We can thus, rewrite Equation (7.3) as:

$$C(\theta)\frac{\partial\psi}{\partial t} = \left\{\frac{1}{r}\frac{\partial}{\partial r}\left[rK(\theta)\frac{\partial\psi}{\partial r}\right]\right\} + \left\{\frac{\partial}{\partial z}\left[K(\theta)\left(\frac{\partial\psi}{\partial z}+1\right)\right]\right\} \tag{7.4}$$

where r and z refer to the radial and axial directions, respectively. By ignoring the radial part of the equation, Equation (7.4) can be used to model problems in the one-dimensional axial direction.

In order to solve Richards equation, we must also specify the constitutive relations between the dependent variable (pressure potential) and the nonlinear terms (moisture content, water capacitance, and the hydraulic conductivity). For this study, we will use van Genuchten's (1990) relationship for the soil moisture content, which can be stated as:

$$\theta = \theta_r + (\theta_s - \theta_r)\left\{\frac{1}{\left(1+|\alpha\psi|^n\right)}\right\}^m \tag{7.5}$$

where θ_r and θ_s define the soil residual and saturated moisture content, respectively. Parameter, α, is equivalent to the inverse of the air-entry pressure (the concept of air-entry pressure will be defined in the next section), and n and m=1-1/n are soil shape parameters. The soil parameters, θ_r, θ_s, α, and n, need to be experimentally measured under wetting and drying conditions. Thus, the unique characteristics of each soil are defined through these parameters. The water capacitance function, $C(\theta)$, can be easily found by differentiating Equation (7.5) with respect to the pressure potential.

In this study, we use Mualem's (1976) mapping, to describe the variations of soil hydraulic conductivity as a function of moisture content:

$$K(S_e) = K_s\sqrt{S_e}\left[1-\left(1-S_e^{1/m}\right)^m\right]^2 \tag{7.6}$$

where K_s is the saturated hydraulic conductivity of the soil, and S_e describes the effective saturation of the soil. S_e can be stated as:

$$S_e = \frac{\theta - \theta_r}{\theta_s - \theta_r} \tag{7.7}$$

Equations (7.5), (7.6), and (7.7) provide the closure required to solve Equation (7.4).

7.1.2 Scott's Model of Capillary Hysteresis

As Equation (7.7) indicates, the soil moisture content-pressure relationship is the primary constitutive relation for describing the flow in the unsaturated zone. This is true, because the water capacitance and hydraulic conductivity relations are directly obtained using the knowledge of soil moisture content. Further the soil dependent parameters have to be determined experimentally. Hillel (1971) explains that the soil moisture content relation can be obtained in two ways. The first way, known as the wetting (sorption) process, entails gradually wetting an initially dry soil sample by reducing the suction (increasing the matric potential). The second way, commonly referred to as the drying (desorption) process, involves increasing the suction (decreasing the matric potential) in an initially saturated soil sample.

During each of the processes (i.e. wetting or drying), we can experimentally collect the moisture content as a function of potential pressure, thus developing the corresponding curves. The two curves are not generally identical. As it turns out, for a given moisture content, the equilibrium soil suction is greater for the drying process than in the wetting process. This phenomenon is graphically depicted in Figure 7.1. The dependence of the equilibrium moisture content and the state of the soil water upon the direction of process (i.e. wetting or drying) is known as the capillary hysteresis.

During repeated wetting and drying cycles of the soil, the process just described can result in different wetting and drying curves and thus display hysteresis of the soil moisture content. In fact as the wetting-drying cycles continue, different scanning curves are obtained. In hydrological parlance, the higher order wetting and drying curves are referred to as the Scanning Wetting Curves (SWC) and Scanning Drying Curves (SDC), respectively. Figure 7.2 displays a typical hysteresis loop that includes one SDC and one SWC.

Regardless of the approach, each model results in various equations that predict the higher order SDCs and SWCs. As a part of this project, we evaluated the ability of three often-used hysteresis models. These models included simple models that use MWC and MDC to scale higher order scanning curves as well as more complex domain dependent models. These models were implemented in the unsaturated flow code, MOIS_HEAD and tested against a series of experimentally determined hysteresis curves. Our conclusion from the model evaluation was that all three models behaved similarly. Therefore, we decided to use the model that is computationally least intensive to perform a series of transient flow analyses.

The model that will be used in the current study is known as Scott's model, developed by Scott et al. (1983). Scott's model defines the MWC and MDC (the curves forming the main hysteresis loop) by using Equation (7.5) along with the parameter vectors $\{\theta_r, \theta_s, n, \alpha\}^W$ and $\{\theta_r, \theta_s, n, \alpha\}^D$, respectively. Superscripts W and D represent the wetting and drying curves, respectively. Therefore, a total of eight parameters are required to initiate the Scott's model.
If we set Equations (7.5) and (7.7) equal to each other, it is easy to show that the effective saturation, S_e,

can be written as:

$$S_e(\psi) = \left\{ \frac{1}{\left(1 + |\alpha\psi|^n\right)} \right\}^m \tag{7.8}$$

Once a reversal from wetting to drying occurs, the curve describing SDC can be computed using Equation (7.5) and the corresponding drainage curve parameters, $\{\theta_r, \theta_{sd}, \alpha, n\}^D$. According to Kool and Parker (1987), the new saturation point, θ_{sd}, on the new drainage path, can be found by:

$$\theta_{sd} = \frac{\theta_{RW} - \theta_r^D \left[1 - S_e^D(\psi_{RW})\right]}{S_e^D(\psi_{RW})} \tag{7.9}$$

where the subscript RW indicates the reversal point from a wetting curve and the superscript D, as before, signifies the drainage curve. The effective saturation at the reversal pressure, ψ_{RW}, can be easily evaluated using Equation (7.8) to obtain the appropriate input parameters.

Using θ_{sd} as the natural saturation point on a wetting curve, the moisture content equation for SDC becomes:

$$\theta_{SDC} = \theta_r^D + \left(\theta_{sd} - \theta_r^D\right) S_e^D(\psi) \tag{7.10}$$

Employing a similar method, once a reversal on a drainage curve to a wetting curve occurs, the corresponding wetting scanning curve can be stated using the set of parameters, $\{\theta_{rw}, \theta_{sw}, \alpha, n\}^W$. The wetting phase residual moisture content, θ_{rw}, according Kool and Parker (1987) becomes:

$$\theta_{rw} = \frac{\theta_{RD} - \theta_s^W \; S_e^W(\psi_{RD})}{\left[1 - S_e^W(\psi_{RD})\right]} \tag{7.11}$$

where the subscript RD describes the reversal point from a drying curve. The moisture content relationship for SWC can be written as:

$$\theta_{SWC} = \theta_{rw} + \left(\theta_{sw} - \theta_{rw}\right) S_e^W(\psi) \tag{7.12}$$

Higher order scanning curves are computed using Equations (7.10) and (7.12), for drying and wetting phases, respectively, as long as the appropriate residual and saturated moisture content values for each curve are known.

7.1.3 Numerical Implementation of the Richards Equation

A new multi-dimensional code (MOIS_HEAD) was developed which is capable of modeling the non-hysteretic and hysteretic infiltration-redistribution events. MOIS_HEAD can be used to model infiltration into extremely dry porous media by linearizing the non-linear components of the Richards equation. This code has shown to be capable of modeling sharp gradient problems easily - a problem that has plagued the

codes that are based on non-linear iterative techniques. Furthermore, since this code is an in-house tool, we can easily make further modifications to improve the code's capabilities. It is important to note that our linearized non-iterative scheme does not reduce the solution accuracy. In fact, Paniconi et al. (1991) report that second-order accurate non-iterative schemes appear to be attractive alternatives to the iterative methods.

7.1.4 Basic Algorithm for Determining the Hysteretic Curves

The hysteresis algorithm used was initially suggested by Klute and Heermann (1974), Gillham et al. (1979), and Kool and Parker (1987). The authors of these papers primarily kept track of the sign of the $\partial\psi/\partial t$ term (the derivative of pressure head with respect to time) to determine if a reversal between two consecutive cycles occurs. As long as the media is draining or wetting, $\partial\psi/\partial t \geq 0$, indicating that $\theta(\psi)$ should be updated on either a drainage or wetting (main or scanning) curve, respectively. When $\partial\psi/\partial t < 0$, a reversal has occurred. A reversal indicates that a new curve for computation of moisture content has to be followed. At the start of the problem, the initial curve (i.e., either the boundary wetting or drying curve) must be specified. Depending upon the initial choice, a hysteresis index, η, a hysteresis curve number, ξ, and boundary curve logical, δ, are assigned to every computational cell. If the media is initialized on the main drying curve the corresponding values are: η=-1, ξ=1, and δ=1 . Conversely, if the media is initialized on the main wetting curve the values assigned to the curves are: η=+1 and ξ=2, and δ=0. During the next cycle, once the pressure potential values have been updated, the pressure difference between two cycles are computed as:

$$\Delta\psi_{ijk} = \psi^{n}_{ijk} - \psi^{o}_{ijk} \tag{7.13}$$

where the superscripts, n and o, indicate the current and previous cycles, respectively, and the subscripts ijk refer to the nodal points in a generalized three-dimensional space. Kool and Parker (1987) suggest using the following criteria to determine whether a reversal has occurred:

$$\frac{\psi^{n}_{ijk} - \psi^{o}_{ijk}}{\eta^{o}_{ijk}} \leq \varepsilon \tag{7.14}$$

where ε is a small positive value used to ignore the effects of small local oscillations in pressure head. The authors used a value of ε=0.10 cm for their example calculations. However, our experience with using Kool and Parker's (1987) criterion revealed that their suggestion adds restrictions to the method. Therefore, it was decided to use the more general method, shown in Equation (7.13), where we are strictly dealing with the sign of pressure difference between two consecutive cycles. Once the reversal criterion has been determined, the algorithm updates the η, ξ, and δ values to determine the appropriate curve and the appropriate moisture content values are then computed based on Scott's model.

7.2 Pre-test Numerical Modeling

In order to determine the behavior of the flow process through the infiltration site, a series of one- and two-dimensional calculations were performed. The following sections describe the model problem along with the results obtained.

7.2.1 Model Problem

We are interested in predicting the infiltration and redistribution through a 6-meter thick layer of silt. The infiltration source is a disk that is 2 meters in diameter and maintains a 10-cm water level (head value for the ponded water). An axisymmetric cylindrical geometry that extends 6 meters in the radial direction must be assumed for this analysis. The basic geometry of the problem is shown in Figure 7.3. Using the geometry presented in Figure 7.3, we have the option of simulating one-dimensional flows in the axial direction as well as two-dimensional (r-z) calculations.

7.2.2 Initial and Boundary Conditions

The initial pressure potential in the vadose zone can range from a few meters to thousands of meters of tension. Hills et al. (1989) state that the pressure heads for dry desert soil can range from -10,000 cm to -300,000 cm. Soil samples collected from the Tijeras Arroyo on the Kirtland Air Force Base revealed that pressure potential values (as represented by the moisture retention curves) can be as low as -15,000 cm. Therefore, for our studies, the initial condition was considered to be uniform at a pressure head of -15,000 cm.

The boundary condition along the axis of symmetry (r = 0 m) and at r = 6 m are considered to be reflective (i.e. $\frac{\partial\psi(r=0)}{\partial r}=0$). The bottom boundary condition (z = 6 m) is also considered to be a no-flow boundary. The top boundary (z = 0 m), as Figure 7.3 illustrates, consists of two boundaries. The specified boundary, $0 \le r \le 1$ m, is set at $\psi = 0.1$ m for the duration of infiltration. Once the water is turned off and the moisture is allowed to redistribute itself, the boundary condition is changed to a no-flow condition. The second portion of the top boundary, $1 \le r \le 6$ m, is also treated as a no-flow boundary.

7.2.3 Hydraulic Properties

Several soil samples were collected from the infiltration site for the modeling activities. Although these samples do not represent the entire range of the material encountered at Tijeras Arroyo, they proved adequate for our initial modeling effort. The initial samples primarily exemplified the silty material observed on the top 3-5 meters. The experimental moisture retention curves for the undisturbed and repacked samples were fitted using the RETC curve fitting code (van Genuchten et al. 1990). The values for the hydraulic properties are presented in the next section.

7.2.4 Undisturbed Sample

The hydraulic properties of the silty material being modeled are listed in Table 7.1. It should be noted that the properties were derived for a water-saturated sample that was allowed to drain until an equilibrium condition was obtained. Therefore the properties refer to the main drying curve shown in Figure 7.1. No data for the main wetting curve are available. However, for the (non-hysteretic and hysteretic) studies, we assumed that the residual and saturated moisture content values are the same on both the drying and the wetting curves. Although this assumption is not accurate, it is adequate for our purposes. Furthermore, we assumed that the van Genuchten parameter n (a measure of the curve's flatness) is also the same on both curves. The only difference between the two curves is the values of the air-entry pressure(ψ_{ae}) and water-entry pressure(ψ_{we}) on the drying and wetting curve, respectively. According to Kool and Parker (1987) it is reasonable to assume $\psi_{ae} = 2\psi_{we}$. Since $\alpha_{ae}=1/\psi_{ae}$ and $\alpha_{we}=1/\psi_{we}$, we can then write $\alpha_{we}=2/\psi_{ae}$.

The moisture-retention curves for MDC and MWC using the values listed in Table 7.1 are shown in Figure 7.4.

7.2.5 Text Book Values

The typical values for the hydraulic properties of silt are listed in Table 7.2. These values are obtained from the RETC code manual. These typical values can be used to compare the numerical results obtained from the two sets of values. Moreover, the similarities and differences among the results can be used to determine whether other samples from the site have to be collected. It must be noted that the moisture-retention values listed in RETC code manual for the main drying curve and the main wetting curve values are found using the same procedure explained in the previous section.

The moisture-retention curves for MDC and MWC using the values listed in Table 7.2 are shown in Figure 7.5. Comparing the values listed in Tables 7.1 and 7.2, we can notice that the residual and saturated moisture contents as well as the n values are fairly similar. The a value, for the undisturbed sample (0.727 m^{-1}) appears to be roughly one-half of the text book value (1.6 m^{-1}). Furthermore the saturated hydraulic conductivity of the undisturbed sample (0.305 m/day) is higher by a factor of five from the text book values (0.06 m/day).

7.3 Numerical Grid System

This section describes the strategies used to optimize the numerical grid system. Our goal is to employ a minimum number of finite difference mesh points without compromising the solution accuracy.

7.3.1 Effect of Grid Resolution

In order to accurately resolve the movement of the moisture front through an unsaturated medium, it is appropriate to place more grid points near the infiltration source. Coarser grid spacing can be used farther away from the infiltration source. Based on the results of a grid sensitivity analysis which examined tradeoffs between prediction accuracy and computation time, we selected the grid listed in Table 7.3 for all simulations.

7.3.2 Numerical Verifications

To compare the results obtained by our code (MOIS_HEAD) to other unsaturated flow codes, we performed a series of one-dimensional calculations using MOIS_HEAD, HYDRUS, and VS2DT. The model problem, for conducting the comparison among the various codes, used the following basic setup. The model involves flow in an initially dry soil (uniform tension of 150.0 m) with the top boundary condition varying as a function of time. The bottom boundary was modeled using the no-flow condition. The time-dependent boundary condition entailed three days of continuous infiltration (constant head) followed by two days of redistribution (no-flow). Because the one-dimensional model primarily pertains to the gravity-driven flow in the soil profile, we believed it would be interesting to analyze the effect of constant-head condition on the flow. Therefore, a total of 12 different boundary values ranging from -0.1 m to 0.1 m were used. This range of boundary conditions also allows us to examine the convergence behavior of the three codes as the gradient at the top of the soil becomes more severe.

Figure 7.6 depicts the result of the one-dimensional model using an applied constant tension of -0.1 m. The figure illustrates the comparison among the three codes (MOIS_HEAD, HYDRUS, and VS2DT) when hysteresis is turned off. The soil hydraulic properties are predicted using the main drainage curve,

as listed in Table 7.1. All three codes employed the same number of grid points (JMAX=350) in the axial direction, and the time-step was set at 10^{-4} days. As the figure shows, the three codes essentially predict the same results. Because of the applied tension at the top boundary condition, the moisture front advances rather gently during the infiltration phase. Furthermore, all three codes predict the moisture front to be at a depth of 1.25 m at the end of the infiltration phase. Based on the results presented here, it is apparent that MOIS_HEAD can be used for all subsequent simulations.

7.4 Two-dimensional Axisymmetric Simulations

This section describes the results of the predictive modeling performed on the model problem. Based on our studies, one-dimensional simulations do not provide adequate representation of the moisture distribution. This is primarily due to the fact that one-dimensional flow problems are gravity-dominated with no assessment of the lateral spread of the moisture.

The initial and boundary conditions were previously described in this report. For the axisymmetric calculations reported in the following sections, the ponded condition was applied for 25 days of infiltration, after which the source was shut off and the moisture was allowed to redistribute for the following 75 days. Therefore, the total simulation time was 100 days.

The non-hysteretic and hysteretic calculations were performed for the undisturbed sample (Table 7.1) and the text book values (Table 7.2). Furthermore, separate non-hysteretic calculations were conducted using the main drainage curve (MDC) and the predicted main wetting curve (MWC).

7.4.1 Non-hysteretic Calculations

Figures 7.7 through 7.10 display the contour plots of moisture distribution through the material, using the MDC fitting parameters (Table 7.1), after 25, 50, 75, and 100 days, respectively. As a reminder, t = 25 days indicates the end of the infiltration phase. As these figures illustrate, the moisture content distribution through the soil is dominated by the capillary action and has a spherical shape. At the end of the simulation (Figure 7.10) the highest moisture content remains at the center of the plume. In Figure 7.11, the moisture content profiles along the axis of symmetry are illustrated for the times mentioned. As the figure indicates at the end of infiltration, the moisture front is roughly at five meters through the soil. During the redistribution phase the lower portion of the soil continues to get wetter as the upper portion drains. In fact, at the end of the simulation the moisture content is uniformly reduced to around 28%.

Figures 7.12 through 7.15 display the contour plots of moisture distribution through the material, using the MWC fitting parameters (Table 7.1), after 25, 50, 75, and 100 days, respectively. These figures indicate that a moisture distribution dominated by gravity. In this case, the moisture penetrates deeper into the soil compared to the previous case. Moreover, the moisture does not spread as much in the radial direction as the previous case. Thus, the moisture content plume has an elliptical shape as opposed to the hemispherical distribution observed when MDC is used. In Figure 7.16, the moisture content profiles along the axis of symmetry are illustrated for the times mentioned. As the figure indicates, at the end of infiltration the moisture front is roughly at six meters through the soil. During the redistribution phase, the lower portion of the soil continues to get wetter as the upper portion drains. In fact, at the end of the simulation the moisture content is uniformly reduced to around 30%.

7.4.2 Hysteretic Calculations

We next examine the results for the hysteretic calculations using the undisturbed sample and text book

values. The hysteretic calculations require that we initialize the problem on one of the bounding curves (MDC or MWC). For these calculations, it is initially assumed that the problem starts on a main drainage curve. As soon as the ponded source is turned on, the computational cells right under the boundary condition are wetting. The wetting process is represented by a sudden increase in the pressure potential. Therefore, the hysteretic curve is some scanning wetting curve (SWC) as computed based on Scott's model. Ultimately, as the moisture front penetrates through the soil, and more of the computational cells experience an increase in the pressure potential, they are moved from MDC to SWC. Meanwhile, the remaining portions of the soil continue to stay on the initial MDC.

Once the infiltration process is discontinued and the ponded source is turned off, the upper portions of the soil (near the top boundary) begin to drain. The drainage is indicated by a reduction in the pressure potential. Therefore, a new moisture-retention curve simulating this process must be used as dictated by the hysteresis algorithm in Scott's model. The new drying curve is some scanning drying curve (SDC). Meanwhile, due to the gravitational effects, the lower portions of the soil continue to get wetter. In other words, the moisture front will move further into the soil, both vertically and laterally.

Figures 7.17 through 7.20 present the results for the hysteretic model after 25, 50, 75, and 100 days, respectively. As the figures show, the overall moisture distribution is more similar to the non-hysteretic case when MWC is used. In other words, the flow is dominated by gravity during infiltration and flow therefore penetrates deeper into the soil. However, during the redistribution process, the center of mass of the plume is deeper into the soil, as opposed to the non-hysteretic cases where the center of mass is at the center of the plume. The behavior portrayed by the hysteretic simulation has been experimentally observed in the laboratory by Glass et al. (1989) and Norton et al. (1995) among others. This phenomenon is quite common when investigating flow instability and fingering in unsaturated media. The experimental observations by these authors have indicated that during unstable flow events, the tip of the plume remains saturated followed by a draining tail.

Finally, in Figure 7.21, the moisture content profiles along the axis of symmetry for the four calculations are shown. The times presented are at the end of the infiltration phase and the end of simulation. The differences during the infiltration phase were previously described. The interesting point to note from this figure is the differences between the non-hysteretic and hysteretic results at the end of the simulation. Using the MDC alone, there is more drainage as opposed to the MWC case. However, when the hysteretic scenario is used the overall drainage is even less. Furthermore, there are two distinct regimes. One regime is above the moisture front where the soil is draining and the other one is below the moisture front where wetting continues.

7.4.3 Calculations Using Text Book Values

Figures 7.22 through 7.24, 7.25 through 7.27, and 7.28 through 7.30, respectively, present the results for non-hysteretic MDC, non-hysteretic MWC, and hysteretic calculations when the text book values (Table 7.2) are used. The simulation times for each plot correspond to 25, 50, and 100 days. The overall behavior of the solution is similar to the one observed when the values from Table 7.2 are used. However, since the saturated hydraulic conductivity of the text book case is smaller (by a factor of five) than the undisturbed sample, there is much less moisture distribution through the media.

7.5 Summary

This section described numerical predictions of the infiltration process for the TAIE made using a finite difference Richards equation solver that is capable of simulating both non-hysteretic and hysteretic

situations. The code was developed in-house. It has been verified using other existing codes such as VS2DT (Lappala et al. 1993), SWMS_2D (Simunek et al. 1994), and HYDRUS (Kool and van Genuchten 1991) that are commonly used for modeling flow through unsaturated porous media. The problem geometry was considered to be two-dimensional in axisymmetric cylindrical coordinates, with a problem domain 8 meters deep and extending 6 meters in the radial direction. The material was assumed to be homogenous. We modeled the soil-moisture retention and relative permeability using van Genuchten's (1990) and Mualem's (1976) formulations.

To assess modeling approaches typically applied at ER sites, the initial calculations involved using two sets of hydraulic properties. The first set of hydraulic property data was based on undisturbed soil samples collected from the site. The second set of hydraulic property data was taken from van Genuchten (1990) and represented the text book values for silty materials with a qualitative description similar to the field soils. The initial condition was set at a uniform tension of 150 meters throughout the model domain. All boundary conditions are assumed to be no-flow conditions except for an infiltration source. The infiltration source was set to be a 2-meter radius disk using a constant head of 0.1 m. The source was allowed to infiltrate the material continuously for 25 days after which the source turned off. The simulation was continued for an additional 75 days--representing the redistribution process.

We also considered the importance of accounting for hysteresis when modeling spills at ER sites. Using each set of hydraulic properties (undisturbed sample and text book values) three different calculations were performed. For the first two calculations the effect of hysteresis was neglected and in the third calculation the effect of hysteresis was considered. The input parameters for the non-hysteretic calculations entailed using the Main Drainage Curve (MDC) and Main Wetting Curve (MWC). For both the non-hysteretic and hysteretic situations, the MWC was predicted using MDC based on a simple rule suggested by Kool and Parker (1987). The two curves, MDC and MWC form the bounding curves for the hysteresis loop. A constrained form of Scott's hysteresis model (Scott et al. 1983 and Kool and Parker 1987) was used to perform the hysteretic calculations.

Results indicated that during the infiltration phase, the moisture plume expands in accordance with the type of the moisture-retention curves used, clearly underlining the importance of using wetting curves for the imbibition process. During the redistribution phase, the upper portion of the soil starts to drain while the lower portions continue to wet and penetrate further into the soil; use of only a single pressure-saturation characteristic curve (e.g., MWC or MDC) clearly cannot account for this process. This can only be accounted for by explicitly considering hysteresis. The overall behavior of the results using the text book values was consistent with those observed for the undisturbed sample. However, because the saturated conductivity for the text book values was smaller by a factor of 5, the moisture plume invaded the profile much less than was predicted when using the properties of the undisturbed sample.

8.0 SUMMARY AND CONCLUSIONS

The Tijeras Arroyo Infiltration Experiment (TAIE) was designed to monitor vadose response to an intermediate-scale ponded infiltration event. The TAIE is analogous to infiltration events where the vadose zone is contaminated through intermediate-sized effluent discharge scenarios.

TAIE accomplishments include: 1) implementation of the infiltration test, 2) mapping of the geology underlying the site, 3) determination of hydraulic properties of soil samples collected at the site, and 4) completing numerical simulations incorporating non-hysteretic and hysteretic conditions.

Based on the data presented in this report, some general conclusions can be made concerning equipment performance and vadose zone response.

Conclusions regarding equipment performance include the following: The data acquisition equipment performed well and provides useful information on flow rates, wetting front advancement, and changes in soil tensions during the redistribution phase of the test. Although the TDR data acquisition systems operated correctly and provided a detailed record of wetting front arrival times, anomalous readings did occur making moisture content data suspect.

Conclusions concerning vadose zone response include the following: Neutron data suggest that the lateral movement of the wetted bulb slightly outpaced the downward movement. Also, lateral spread of the wetted bulb was more extensive in the a coarse textured layer which is sandwiched between two finer textured layers. Numerical simulations of homogenous material incorporating textbook values of hydraulic properties can misrepresent true conditions. However, when the undisturbed sample hydraulic properties were used, the computed wetting front advancement was more representative of the observed behavior.

9.0 REFERENCES

Dane, J. H., and P. J. Wierenga, 1975. Effect of Hysteresis on the Prediction of Infiltration, Redistribution, and Drainage of Water in Layered Soil, *J. Hydrology*, vol. 25, pp. 229-242.

Goering, T. J., M. D. McVey, W. R. Strong, and J. L. Peace, 1996. Analysis of Instantaneous Profile Test Data from Soils Near the Mixed Waste Landfill, Technical Area 3, Sandia National Laboratories/New Mexico. SAND95-1637. Sandia National Laboratories/New Mexico, Albuquerque, NM.

Gillham, R. W., A. Klute, and D. F. Heermann, 1976. Hydraulic Properties of a Porous Medium: Measurements and Empirical Representation, *Soil Sci. Soc. Am. J.*, vol. 40, pp. 203-207.

Gillham, R. W., A. Klute, and D. F. Heermann, 1979. Measurements and Numerical Simulation of Hysteretic Flow in a Heterogeneous Porous Medium, *Soil Sci. Soc. Am. J.*, vol. 43, pp. 1061-1067.

Glass, R. J., T. S. Steenhuis, and J. Y. Parlange, 1988. Wetting front Instability as a Rapid and Far-reaching Hydrologic Process in the Vadose Zone, *J. Contam. Hydrol*. vol. 3, pp. 207-226.

Glass, R. J., T. S. Steenhuis, and J. Y. Parlange, 1989. Mechanism for Finger Persistence in Homogenous Unsaturated, Porous Media: Theory and Verification, *Soil Science*, vol. 148, No. 1, pp. 60-70.

GRAM, Inc. and William Lettis & Associates, Inc., 1995. Conceptual Geologic Model of the Sandia National Laboratories and Kirtland Air Force Base. Sandia National Laboratories/New Mexico, Albuquerque, NM.

Hacker, L., 1977. Soil Survey of Bernalillo County and Parts of Sandoval and Valencia Counties, New Mexico, U.S. Department of Agriculture, Washington, D.C.

Hawley, J. W., and C. S. Haase (editors), 1992. Hydrogeologic Framework of the Northern Albuquerque Basin, New Mexico Bureau of Mines and Mineral Resources, Open-File Report 387, Socorro, NM.

Hillel, D., 1971. Soil and Water: Physical Principles and Processes, Academic Press, Inc., San Diego, Ca.

Hillel, D., 1980. Fundamental of Soil Physics. Academic Press, New York, 385p.

Hills, R. G., I. Porro, D. B. Hudson, and P.J. Wierenga, 1989. Modeling One-Dimensional Infiltration Into Very Dry Soils, I. Model Development and Evaluation, *Water Resour. Res.*, vol. 25, no. 6, pp. 1259-1269.

Hills, R. G., and P. J. Wierenga, 1991. Model Validation at the Las Cruces Trench, NUREG/CR5716. U.S. Nuclear Regulatory Commission Technical Report.

Hoagland, S.R., 1990. A Cultural Resources Survey and Review for Sandia National Laboratories, Area I, South of O Street, Kirtland Air Force Base, New Mexico. Chambers Group, Inc. Albuquerque, NM.

Holt, R., 1992. Vadose Zone Characterization Study Approach Outline, Draft.

IT Corporation, 1994. Report on the Sensitive Species Survey for the Infiltration Test Area South of Technical Area IV, letter report from N. Timothy Fischer of IT to Richard E. Fate of SNL/NM on

October 25, 1994. IT Project Number 301462.100.03.001.

Jones, M. J., and K. K. Watson, 1987. Effect of Soil Water Hysteresis on Solute Movement During Intermittent Leaching, *Water Resour. Res.*, vol. 23, no. 7, pp. 1251-1256.

Kaluarachchi, J. J., and J. C. Parker, 1987. Effect of Hysteresis with Air Entrapment on Water Flow in the Unsaturated Zone, *Water Resour. Res.*, vol. 23, no. 10, pp. 1967-1976.

Klute, A., and D. F. Heermann, 1974. Soil Water Profile Development Under a Periodic Boundary Condition, *Soil Science*, vol. 117, No. 5, pp. 265-271.

Kool, J. B., and J. C. Parker, 1987. Development and Evaluation of Closed-Form Expressions for Hysteretic Soil Hydraulic Properties, *Water Resour. Res.*, vol. 23, no. 1, pp. 105-114.

Kool, J. B., and M. Th. van Genuchten, 1991. HYDRUS: One-Dimensional Variably Saturated Flow and Transport Model, Including Hysteresis and Root Water Uptake, Version 3.31, U. S. Salinity Laboratory, USDA, Riverside, CA.

Lappala, E. G., R. W. Healy, and E. P. Weeks, 1993. Documentation of Computer Program VS2D to Solve the Equations of Fluid Flow in Variably Saturated Porous Media, U. S. Geological Survey, Water-Resources Investigation Report 83-4099, Denver, CO.

Lozinsky, R.P., 1988. Stratigraphy, Sedimentology, and Sand Petrology of the Santa Fe Group and Pre-Santa Fe Tertiary Deposits in the Albuquerque Basin, Central New Mexico, unpublished Ph.D. dissertation, New Mexico Institute of Mining and Technology, Socorro, NM.

McCord, J.T., and M.T. Goodrich, 1995. Monte Carlo Stochastic Analysis of Macrodispersivities for Non-Ergodic Transport through Heterogeneous Vadose Zones. In Proceedings of AICHE/ASME National Heat Transfer Conference Special Session on Multiphase Flow and Transport in Environmental Problems, Portland, OR.

McCord, J.P., J.T. McCord, J.D. Gibson, and H.L. King, 1993. Site-Wide Hydrogeologic Characterization Project Calendar Year 1992 Annual Report, SNL/NM Environmental Restoration Project, Albuquerque, NM.

Mualem, Y., 1976. A New Model for Predicting the Hydraulic Conductivity of Unsaturated Porous Media, *Water Resour. Res.*, vol. 12, no. 3, pp. 513-522.

Norton, D. L., 1995. Evaluation, Extension, and Application of a Full Field Light Transmission Technique for the Investigation of Hysteresis in Thin Homogenous Sand Slabs, Ph.D. Dissertation, University of Arizona.

Oldenburg, C. M., and K. Pruess, 1993. On Numerical Modeling of Capillary Barriers, *Water Resour. Res.*, vol. 29, no. 4, pp. 1045-1056.

Paniconi, C., A. A. Aldama, and E. F. Wood, 1991. Numerical Evaluation of Iterative and Noniterative Methods for the Solution of the Nonlinear Richards Equation, *Water Resour. Res.*, vol. 27, no. 6, pp. 1147-1163.

Parsons, A. M., R. J. Glass, and J. T. McCord, 1993. Vadose Zone Characterization Task Plan for the Site-Wide Hydrogeologic Characterization Project, Sandia National Laboratories/New Mexico, Albuquerque, NM.

Parsons, A. M., J. T. McCord, R. P. Thomas, and M. Furaus, (in press). Using a Geographic Information System to Select Vadose Zone Hydrogeologic Settings for Guiding Site Characterization, SAND93-1843, Sandia National Laboratories/New Mexico, Albuquerque, NM.

Roepke, C., R. J. Glass, J. Brainard, M. Mann, K. Kriel, R. Holt., 1995. Fernald 1994 Transport Processes Investigation: Data Report. Sandia National Laboratories/New Mexico Geohydrology Department 6115. Prepared for DOE Office of Technology Development, Fernald, OH.

Ross, B., 1990. The Diversion Capacity of Capillary Barriers, *Water Resour. Res.*, vol. 26, no. 10, pp. 2625-2629.

Scott, P. S., G. J. Farquhar, N. Kouwen, 1983. Hysteretic Effects on Net Infiltration, Advances in Infiltration, pp. 163-170, *Publ. 11-83*, Am. Soc. Agric. Eng. St. Joseph, MI.

Simunek, J., T. Vogel, and M. Th. van Genuchten, 1994. The SWMS_2D Code for Simulating Water Flow and Solute Transport in Two-Dimensional Variably Saturated Media, Research Report No. 132, U. S. Salinity Laboratory, USDA, Riverside, CA.

SNL/NM (Sandia National Laboratories/New Mexico), 1994. Site-Wide Hydrogeologic Characterization Project Calendar Year 1993 Annual Report, SNL/NM Environmental Restoration Project, Albuquerque, NM.

SNL/NM (Sandia National Laboratories/New Mexico), 1994a. Program Implementation Plan for Albuquerque Potential Release Sites, prepared for the U.S. DOE/Albuquerque Operations Office, Albuquereque, NM.

SNL/NM (Sandia National Laboratories/New Mexico), 1995. Site-Wide Hydrogeologic Characterization Project Calendar Year 1994 Annual Report, SNL/NM Environmental Restoration Project, Albuquerque, NM.

SNL/NM (Sandia National Laboratories/New Mexico), 1996. Site-Wide Hydrogeologic Characterization Project Calendar Year 1995 Annual Report, SNL/NM Environmental Restoration Project, Albuquerque, NM.

Stephens, D.B., A.M. Parsons, E.D. Mattson, K.Black, K. Flannigan, R.S. Bowman, and W. Cox, 1988. A Field Experiment of Three-Dimensional Flow and Transport in a Stratified Soil, in Proceedings of the Conference on Validation of Flow and Transport for the Unsaturated Zone, Ruidoso, NM, May 22-25, 1988.

Topp, G. C., 1969. Soil-Water Hysteresis Measured in a Sandy Loam and Compared with Hysteretic Domain Model, *Soil Sci. Soc. Amer. Proc.*, vol. 33, pp. 645-651.

Topp, G. C., 1971. Soil-Water Hysteresis: The Domain Model Theory Extended to Pore Interaction Conditions, *Soil Sci. Soc. Amer. Proc.*, vol. 35, pp. 219-225.

Topp, G. C., and E. E. Miller, 1966. Hysteretic Moisture Characteristics and Hydraulic Conductivities for Glass-Bead Media, *Soil Sci. Soc. Amer. Proc.*, vol. 30, pp. 156-162.

Topp, G. C., J. L. Davis, and A.P. Annan, 1980. Electromagnetic Determination of Soil Water Content: Measurements in Coaxial Transmission Lines, *Water Resour. Res.*, vol. 16, pp. 574-582.

Vachaud, G., and J. L. Thony, 1971. Hysteresis During Infiltration and Distribution in a Soil Column at Different Initial Water Contents, *Water Resour. Res.*, vol. 7, no. 1, pp. 111-127.

van Genuchten, M. Th., F. J. Leij, and S. R. Yates, 1991. The RETC Code for Quantifying the Hydraulic Functions of Unsaturated Soil, *EPA/600/2-91/065*, December.

Wierenga, P. J., R. G. Hills, D. B. Hudson, 1991. The Las Cruces Trench Site: Characterization, Experimental Results, and One-Dimensional Flow Predictions, *Water Resour. Res.*, Vol 27, no 10, pp. 2695-2705.

FIGURES

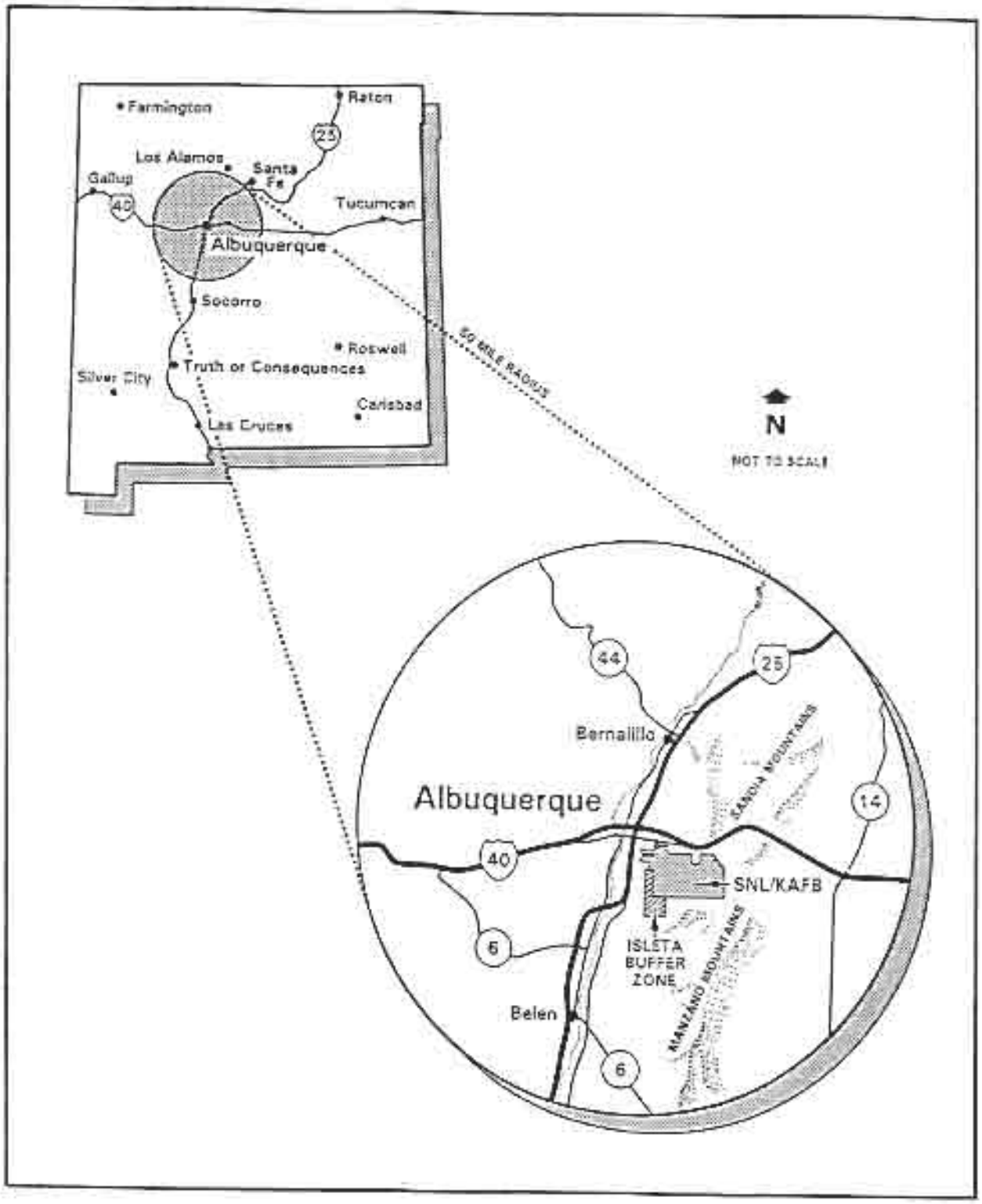

Figure 3.1: General Location Map of SNL/NM

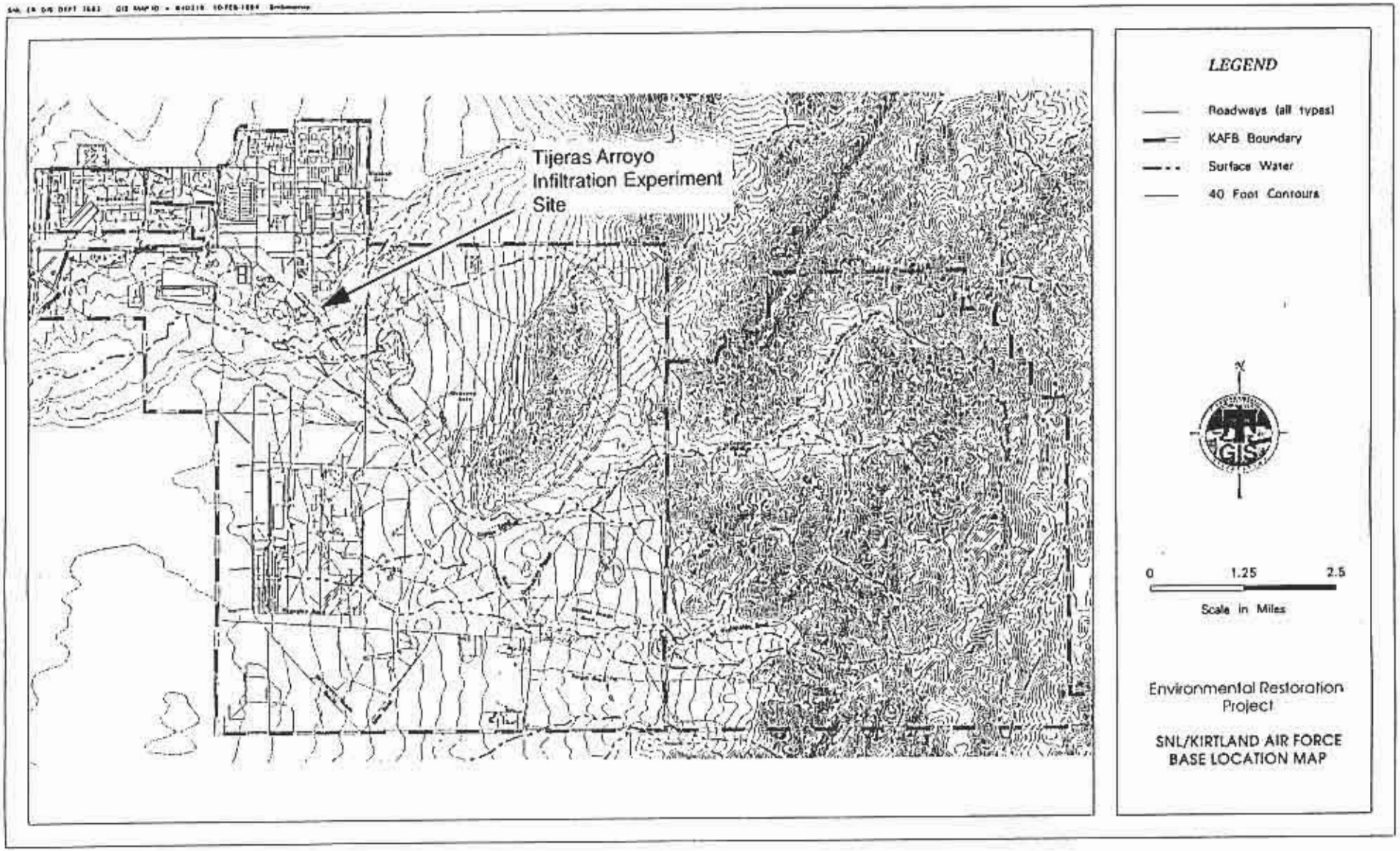

Figure 3.2: SNL/KAFB Location Map

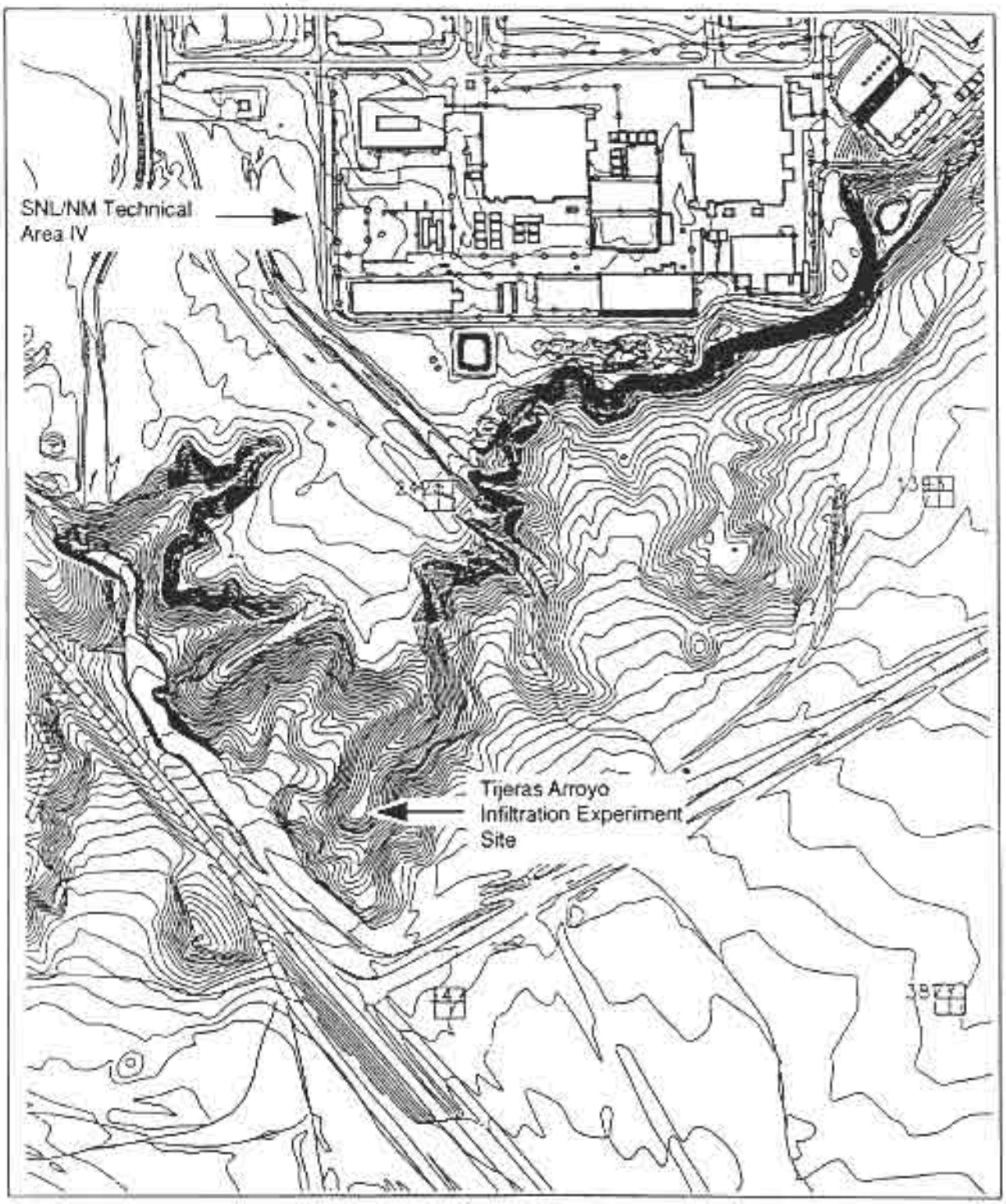

Figure 3.3: Plan View of Infiltration Site and Surrounding Area

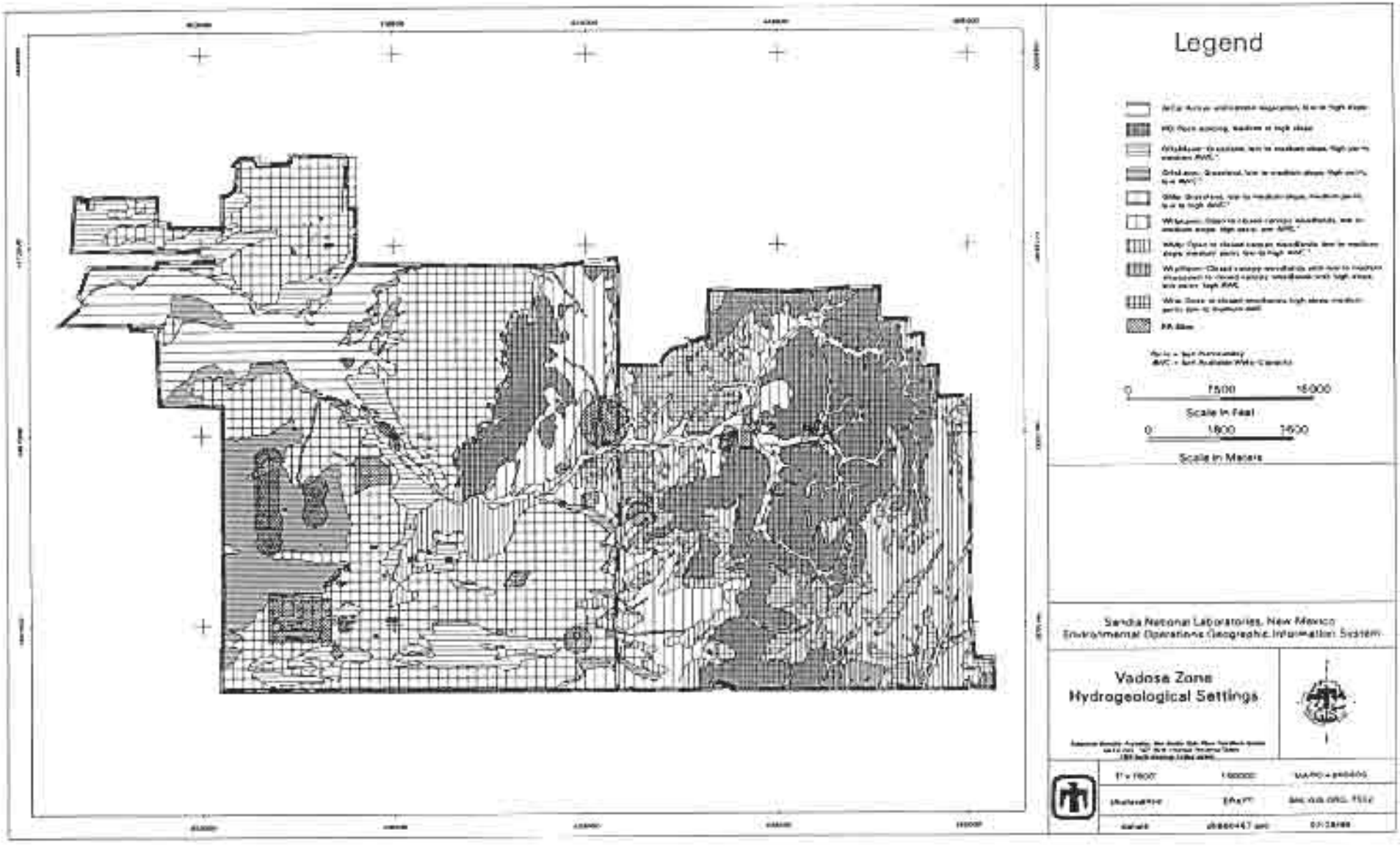

Figure 4.1.1: Vadose Zone Hydrogeologic Settings

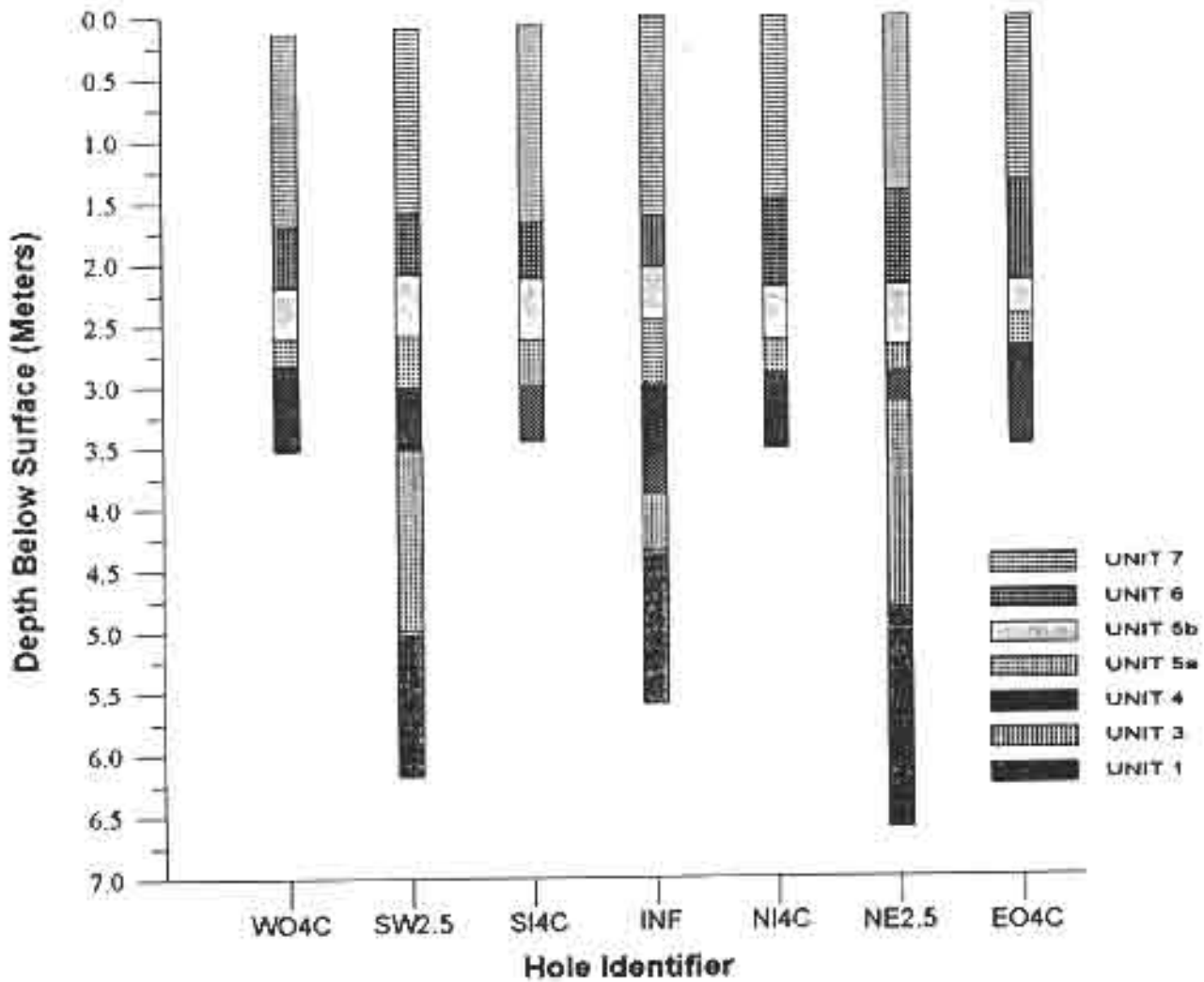

Figure 4.2.1: Southwest-Northeast Geologic Cross-Section (see Figure 4.2.6 for cross-section location)

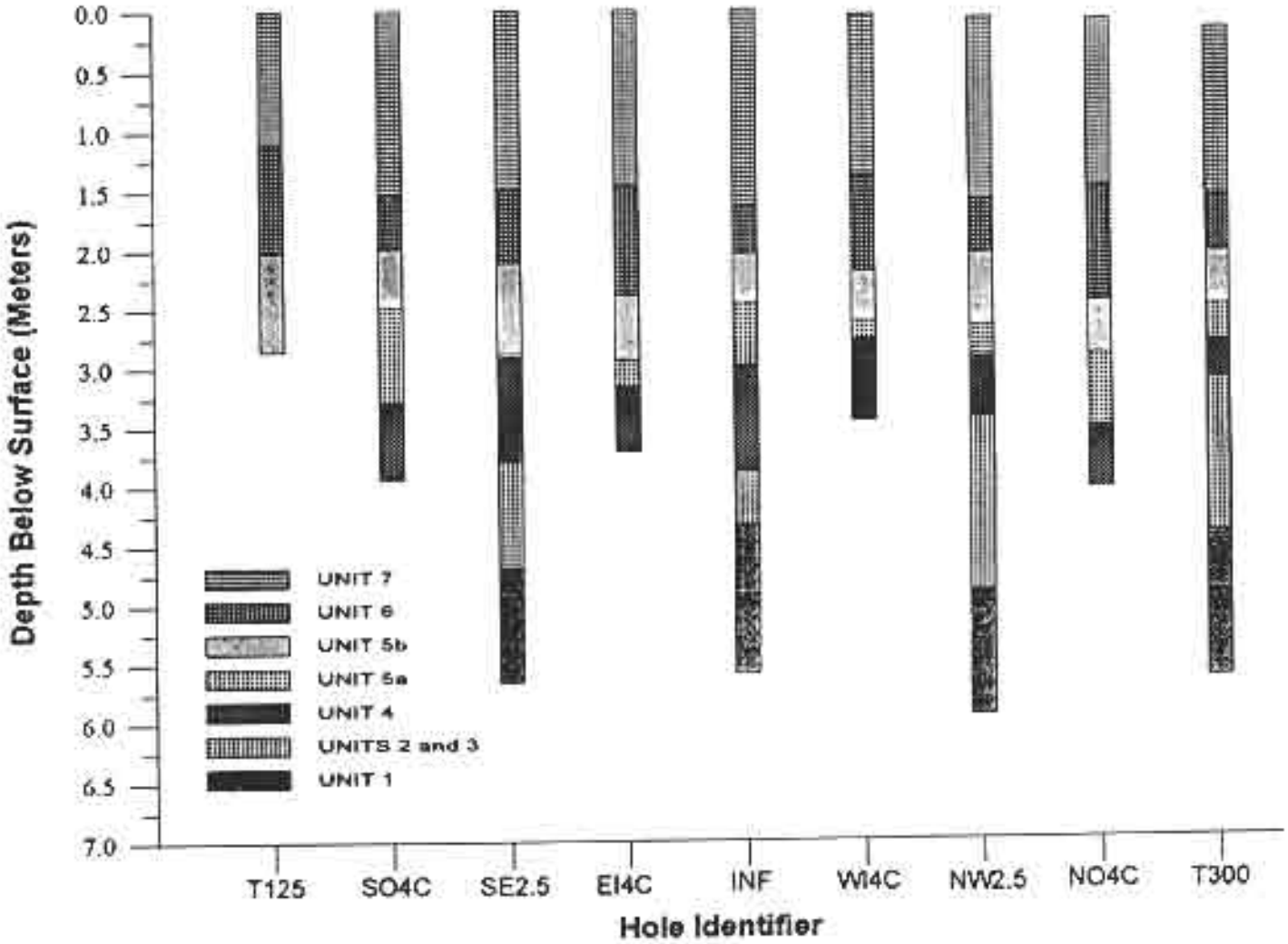

Figure 4.2.2: Northwest-Southeast Geologic Cross-Section (see Figure 4.2.6 for cross-section location)

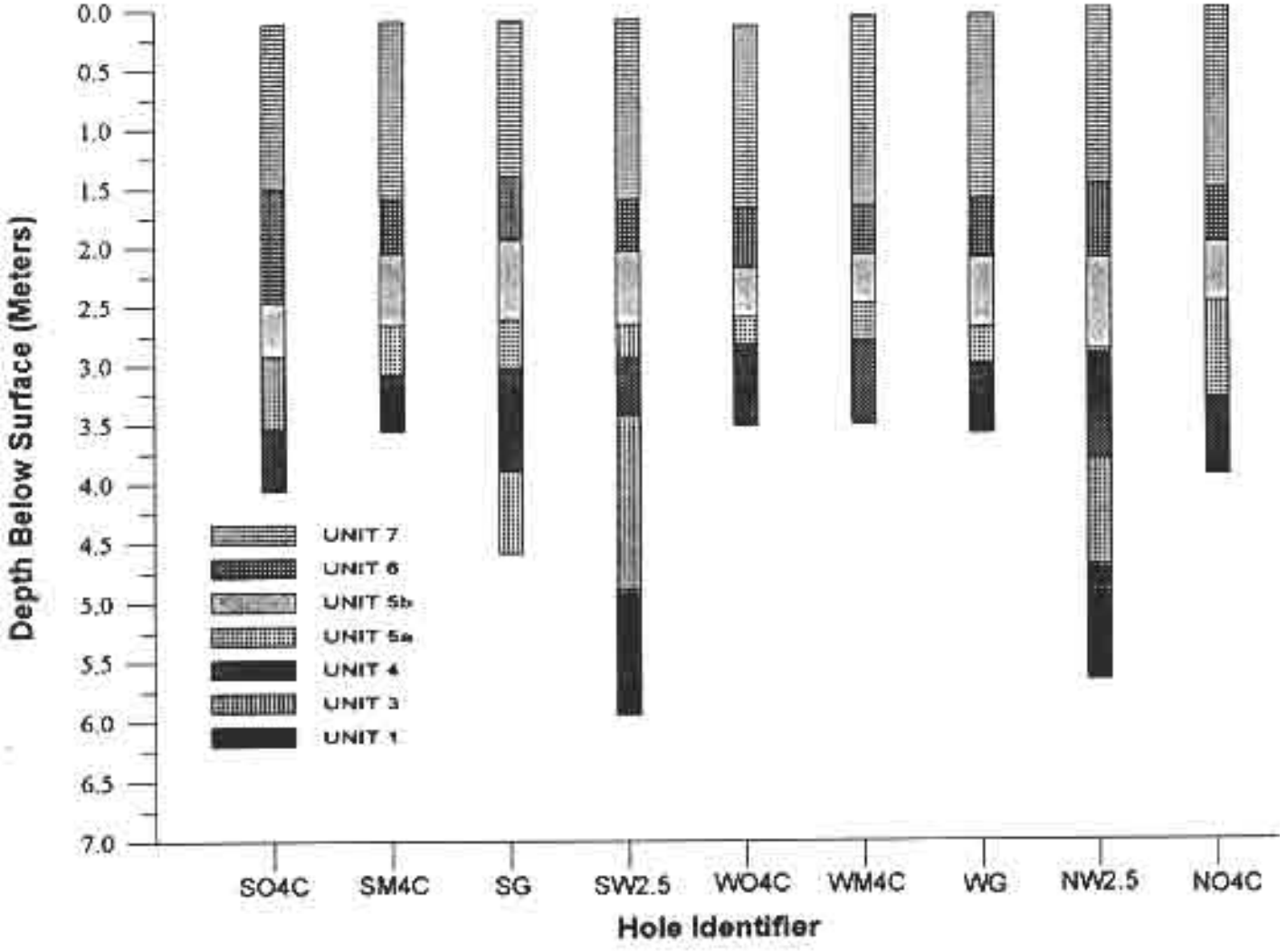

Figure 4.2.3: South-West Geologic Cross-Section (see Figure 4.2.5 for cross-section location)

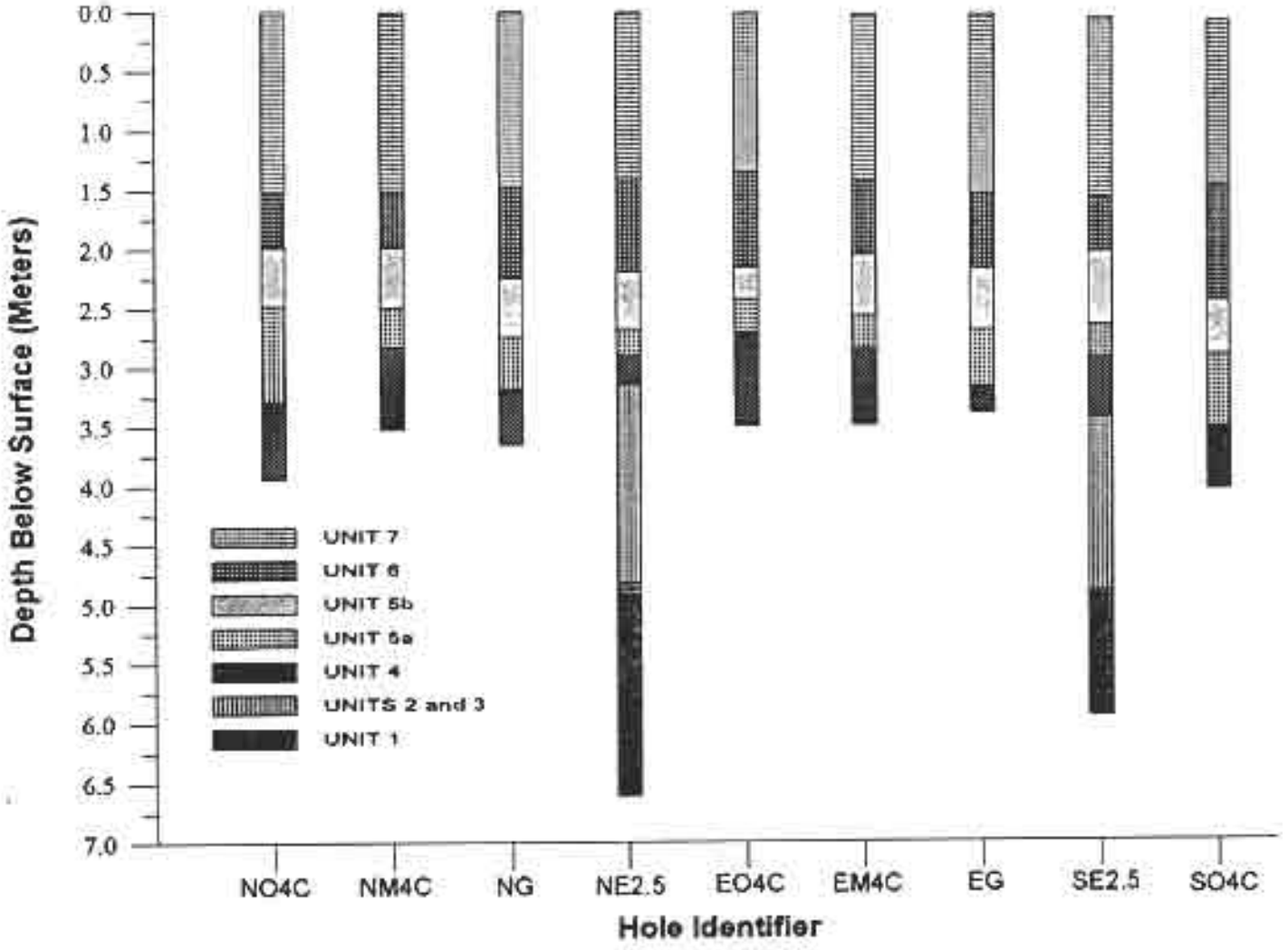

Figure 4.2.4: North-East Geologic Cross-Section (see Figure 4.2.5 for cross-section location)

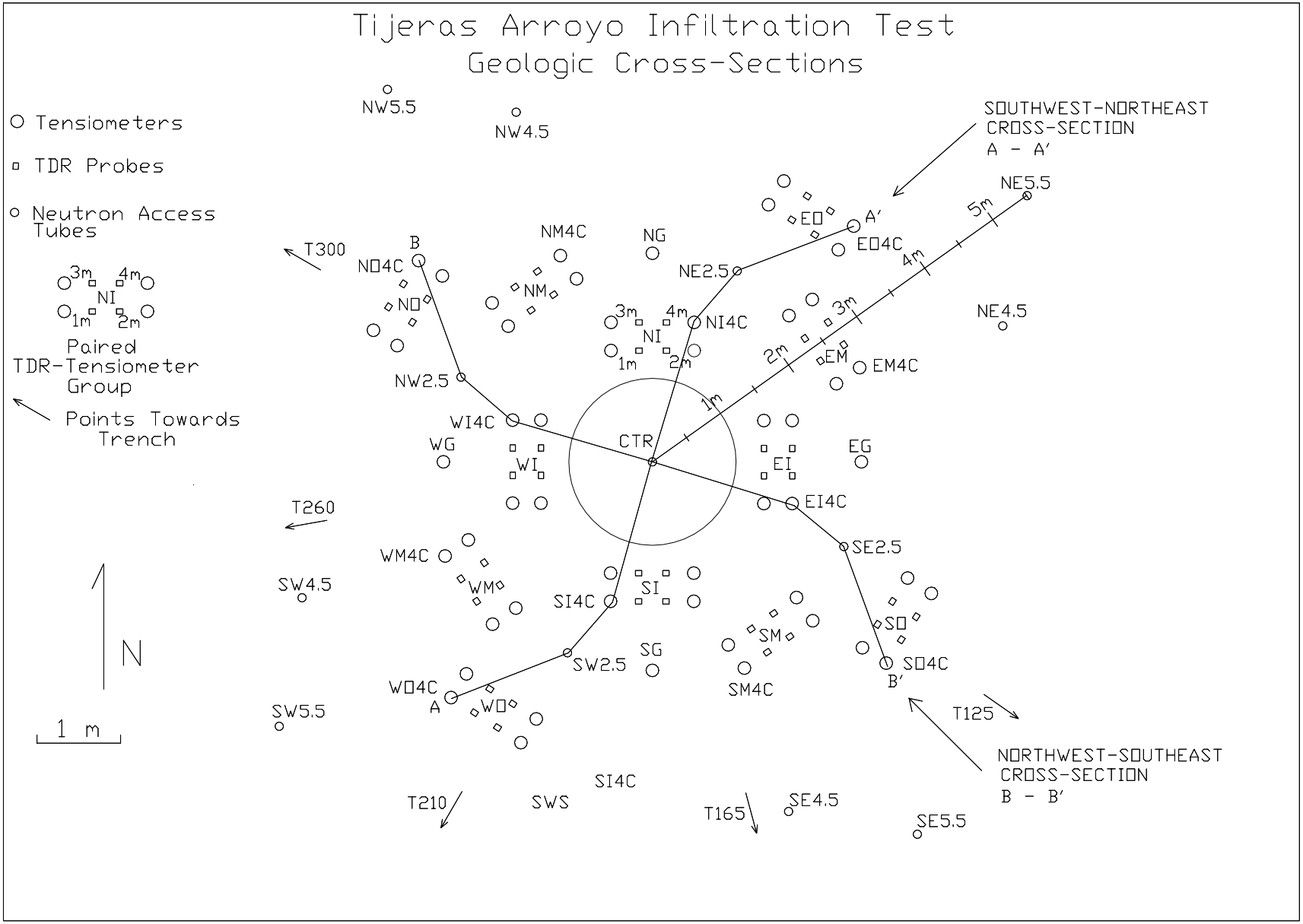

Figure 4.2.5: Plan View Showing the Locations of the Southwest-Northeast and Northwest-Southeast Geologic Cross-Sections

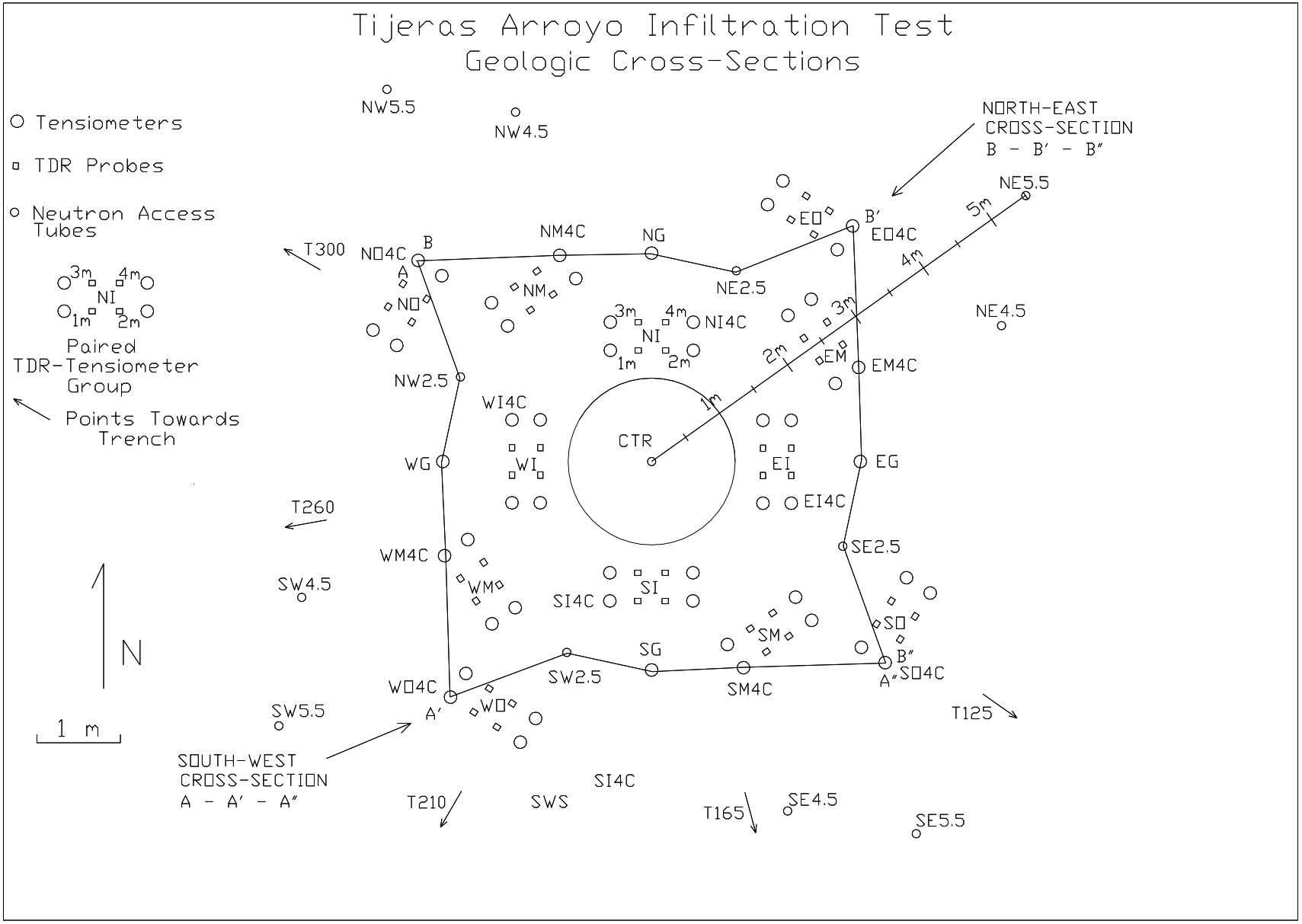

Figure 4.2.6: Plan View Showing the Locations of the South-West and North-East Geologic Cross-Sections

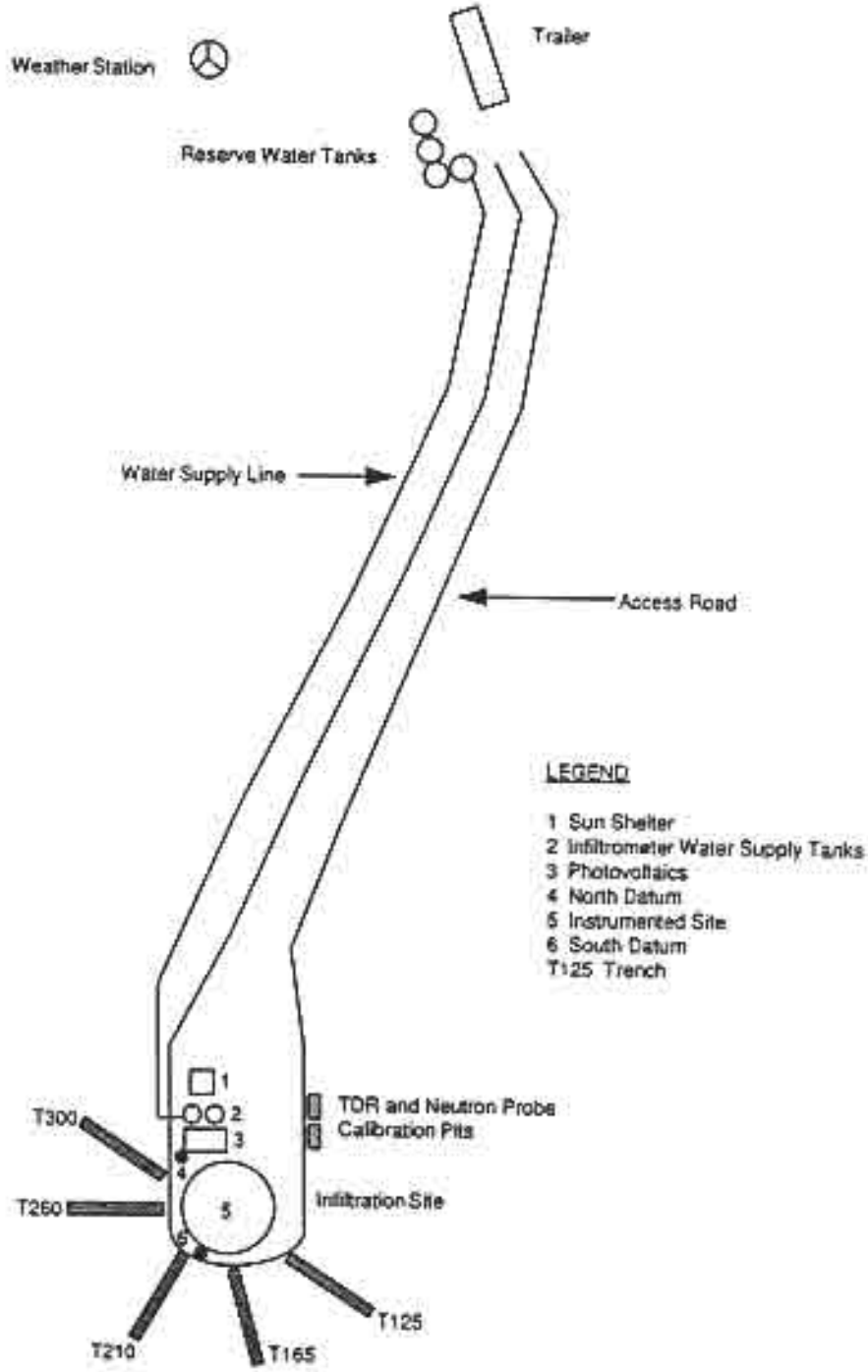

Figure 5.2.1: Schematic Plan View of Infiltration Site (Not to Scale)

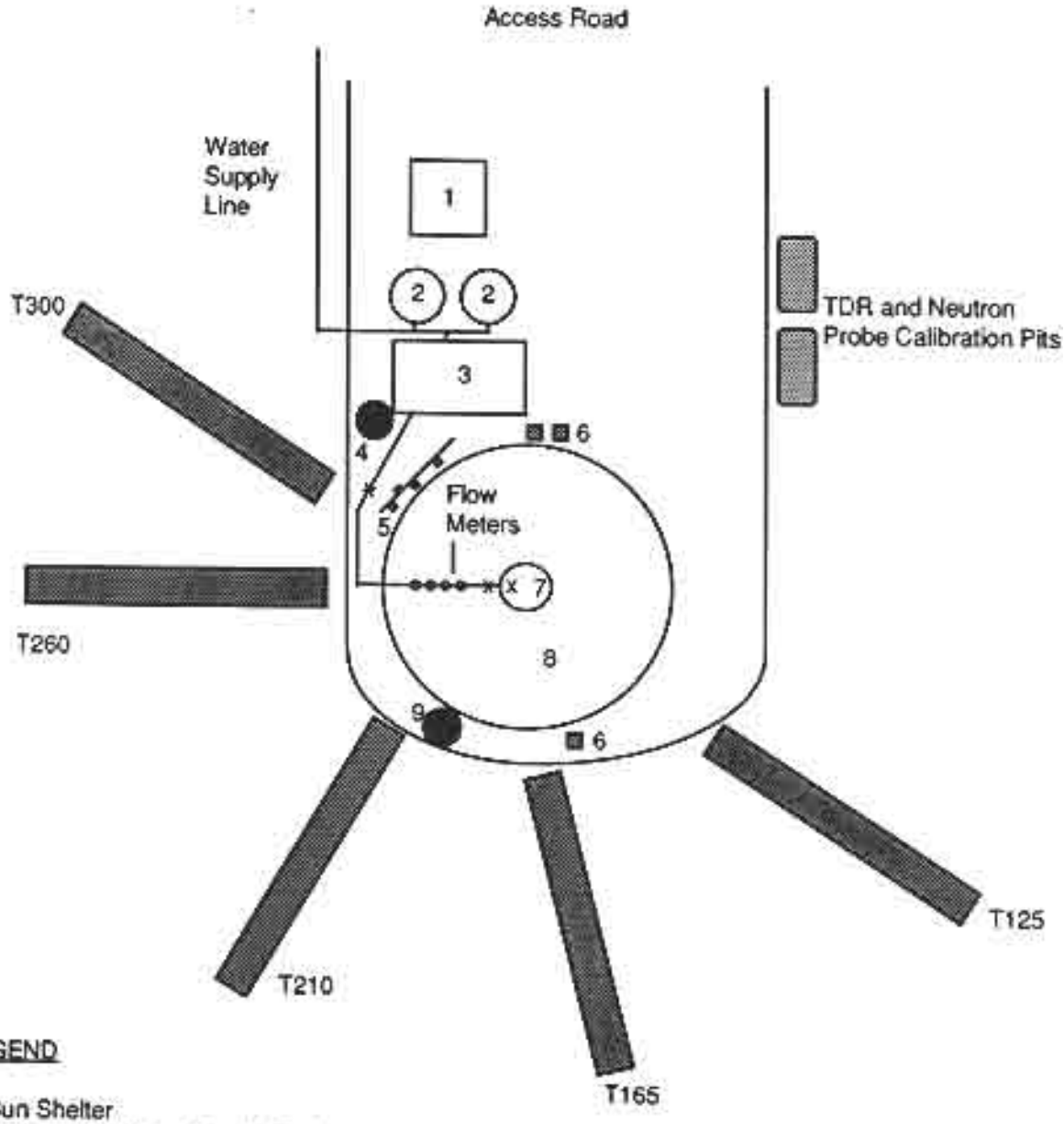

LEGEND

1 Sun Shelter
2 Infiltrometer Water Supply Tanks
3 Photovoltaics
4 North Datum
5 Tensiometer Data Acquisition Systems Board and Enclosures
6 TDR Data Acquistion Systems
7 Infiltrometer
8 Instrumented Site
9 South Datum
X Water Line Temperature Probe Locations
T125 Trench

Figure 5.2.2: Schematic Plan View of Infiltration Site Detail (Not to Scale)

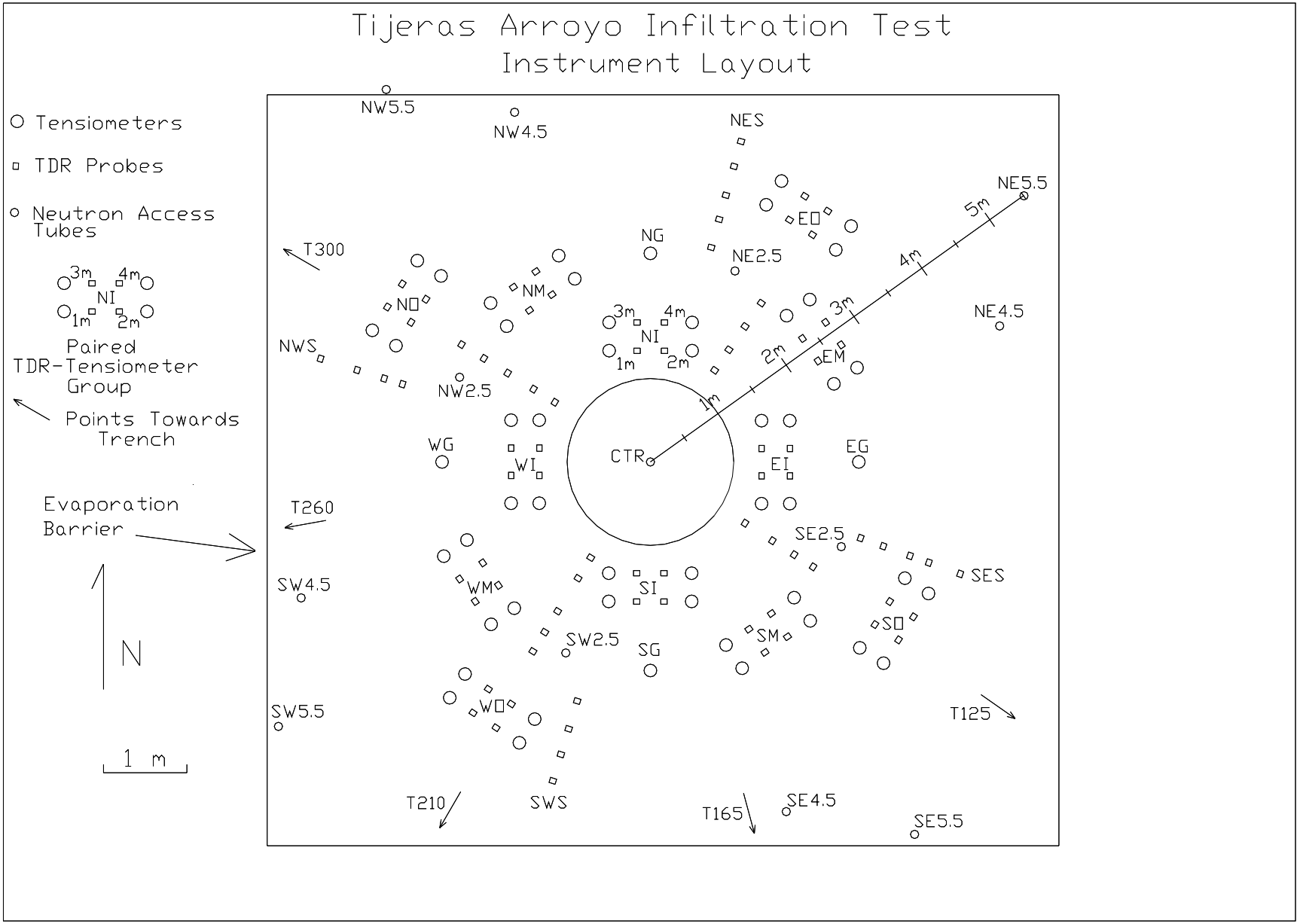

Figure 5.2.3: Plan View Showing Layout of Instrument Arrays (see Table 5.1 for Explanation of Abbreviations)

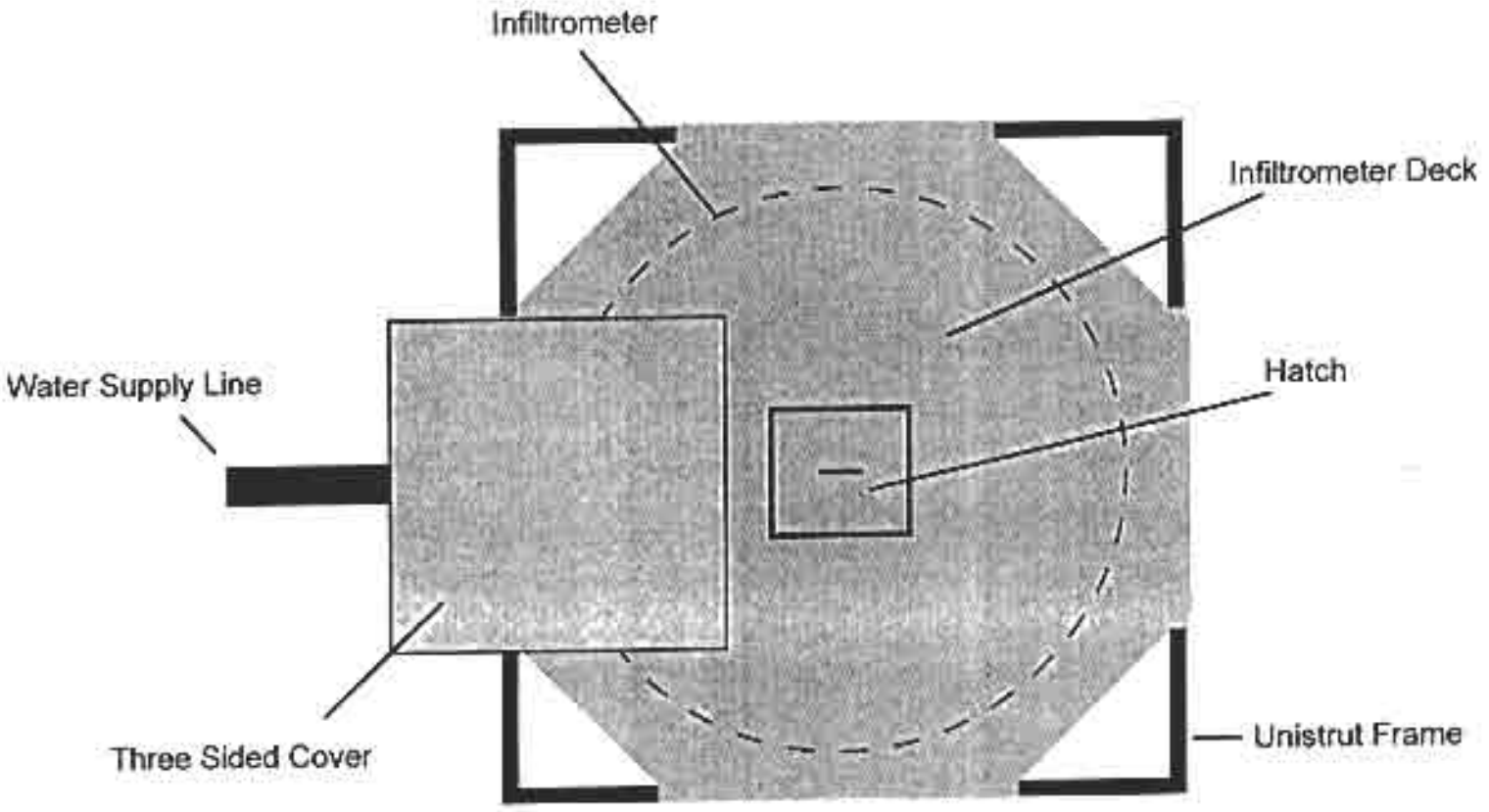

Figure 5.4.1: Infiltrometer and Infiltrometer Deck Detail

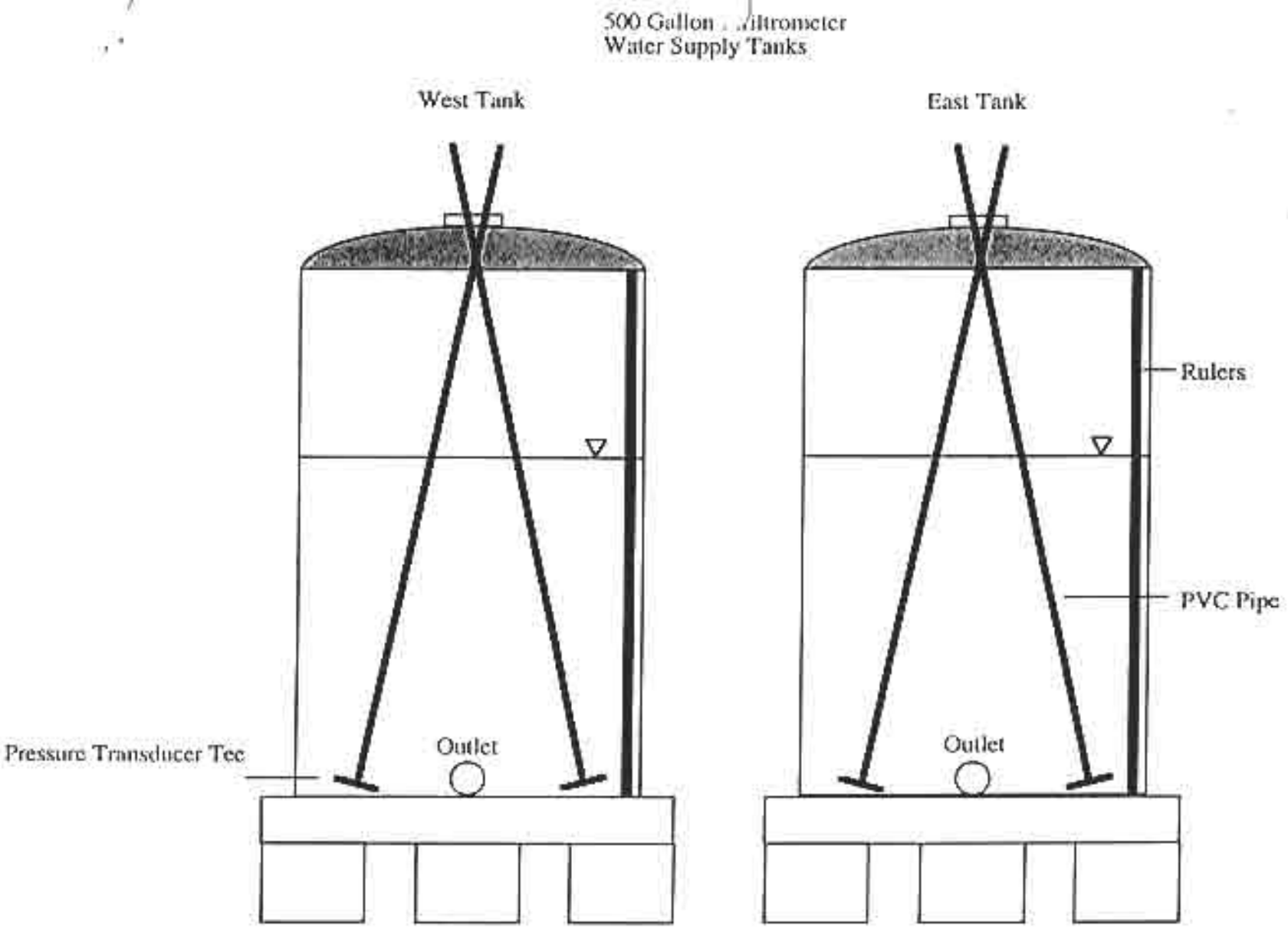

Figure 5.6.1: 500 Gallon Infiltrometer Water Supply Tanks

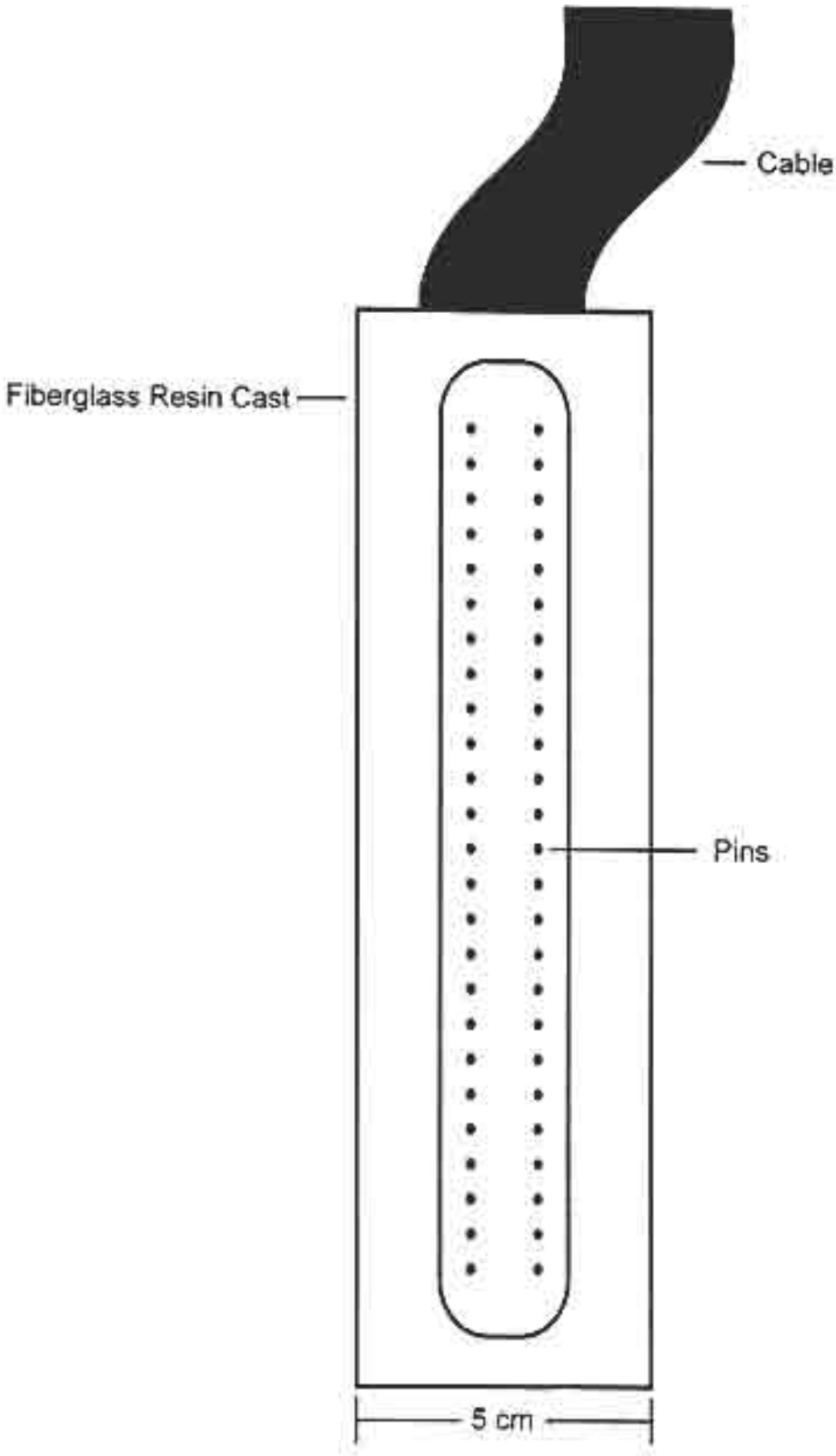

Figure 5.6.2: Resistive Water Level Recording Device

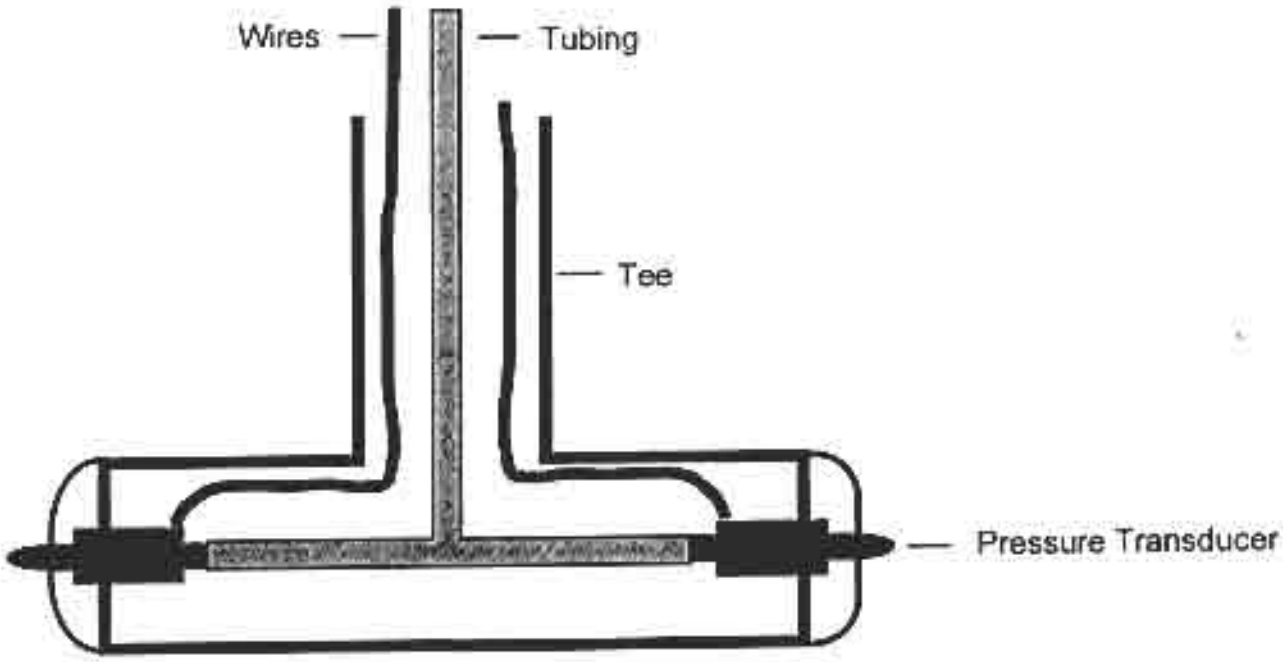

Figure 5.6.3: Pressure Transducer in PVC Tee

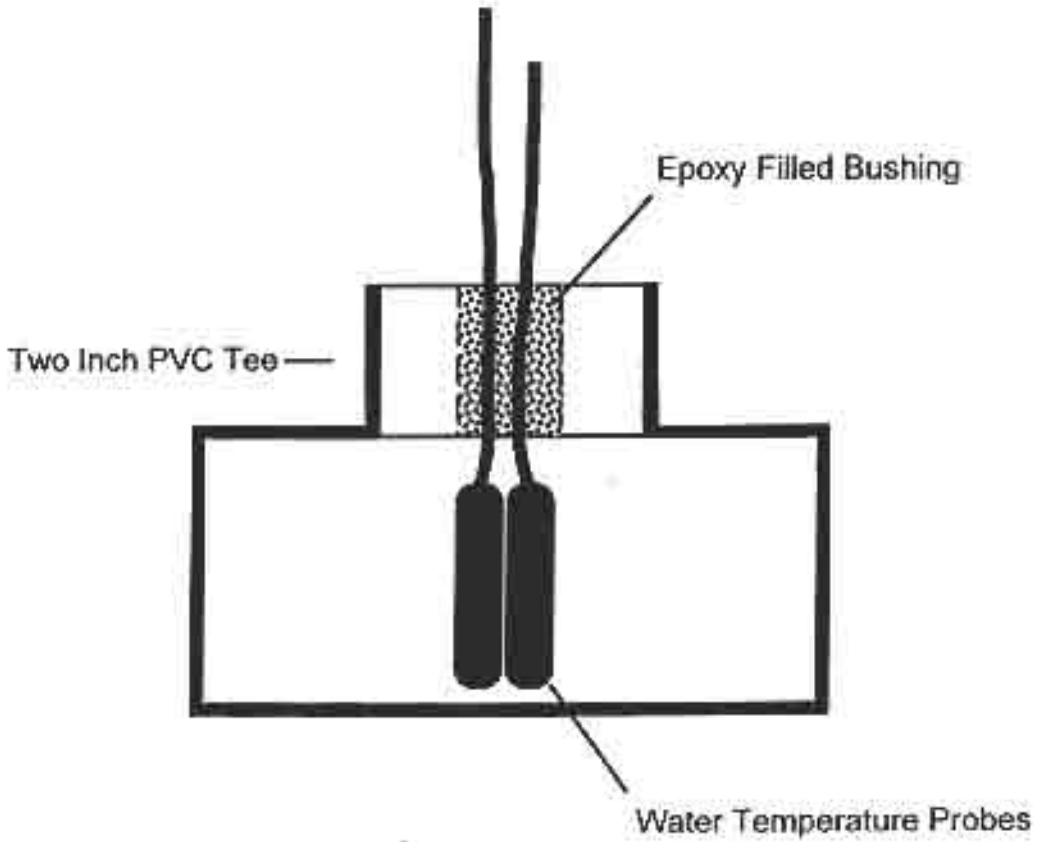

Figure 5.7.1: Water Temperature Probes in PVC Pipe

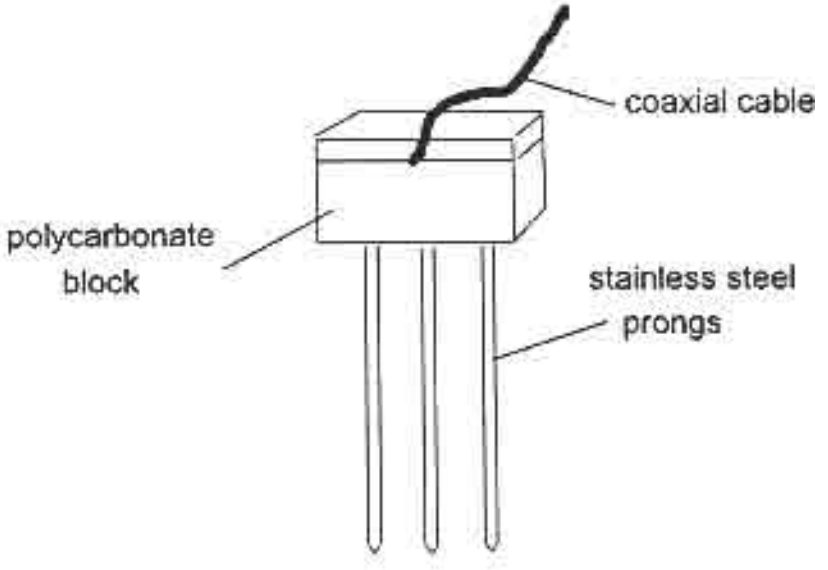

Figure 5.8.1: TDR Probe Detail

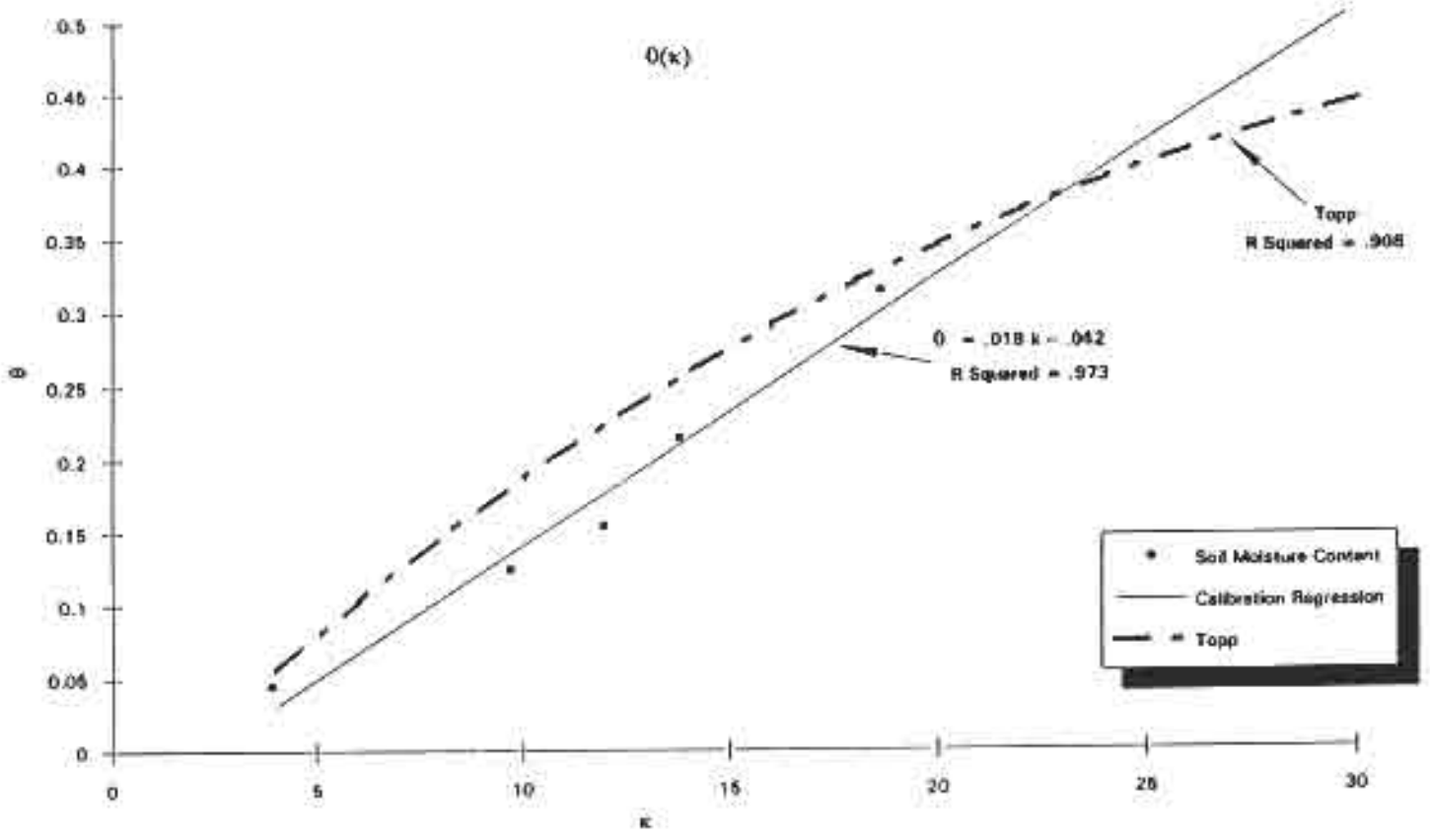

Figure 5.8.2: Results of Sampling and TDR Calibration in the Red, Silty Loam

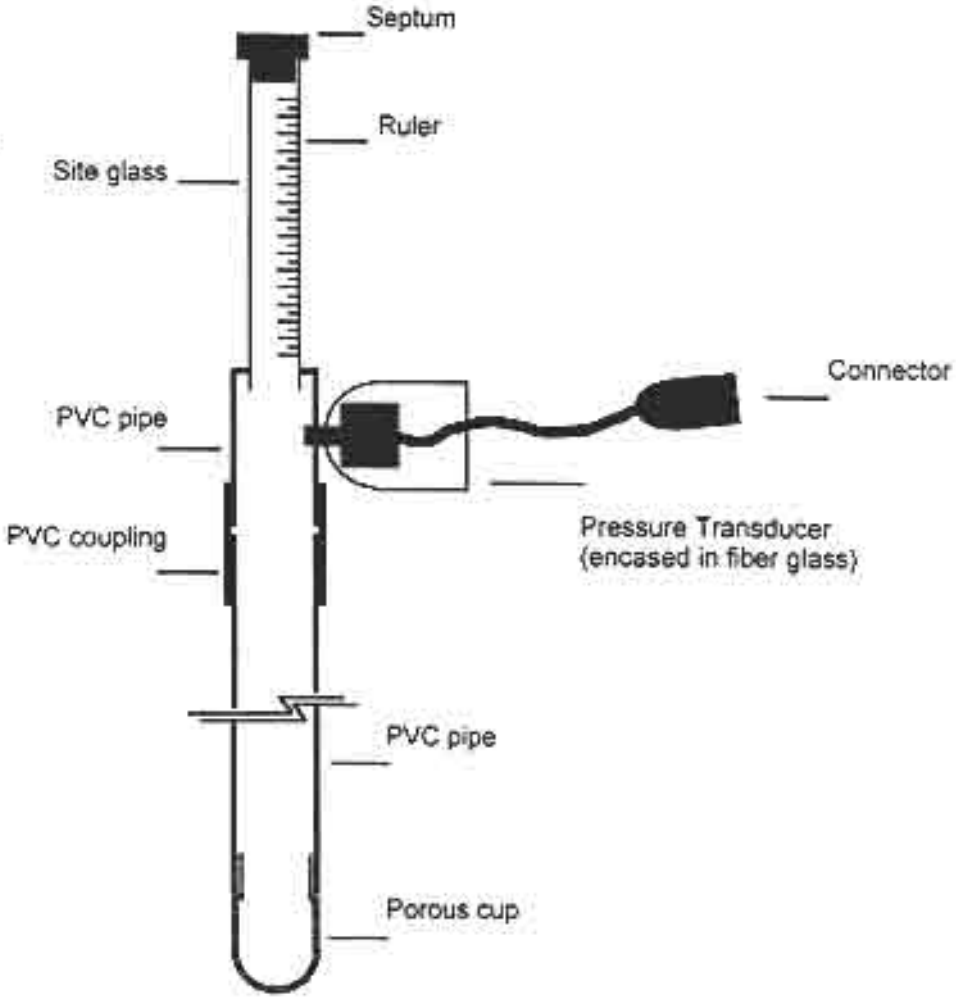

Figure 5.10.1: Tensiometer Detail

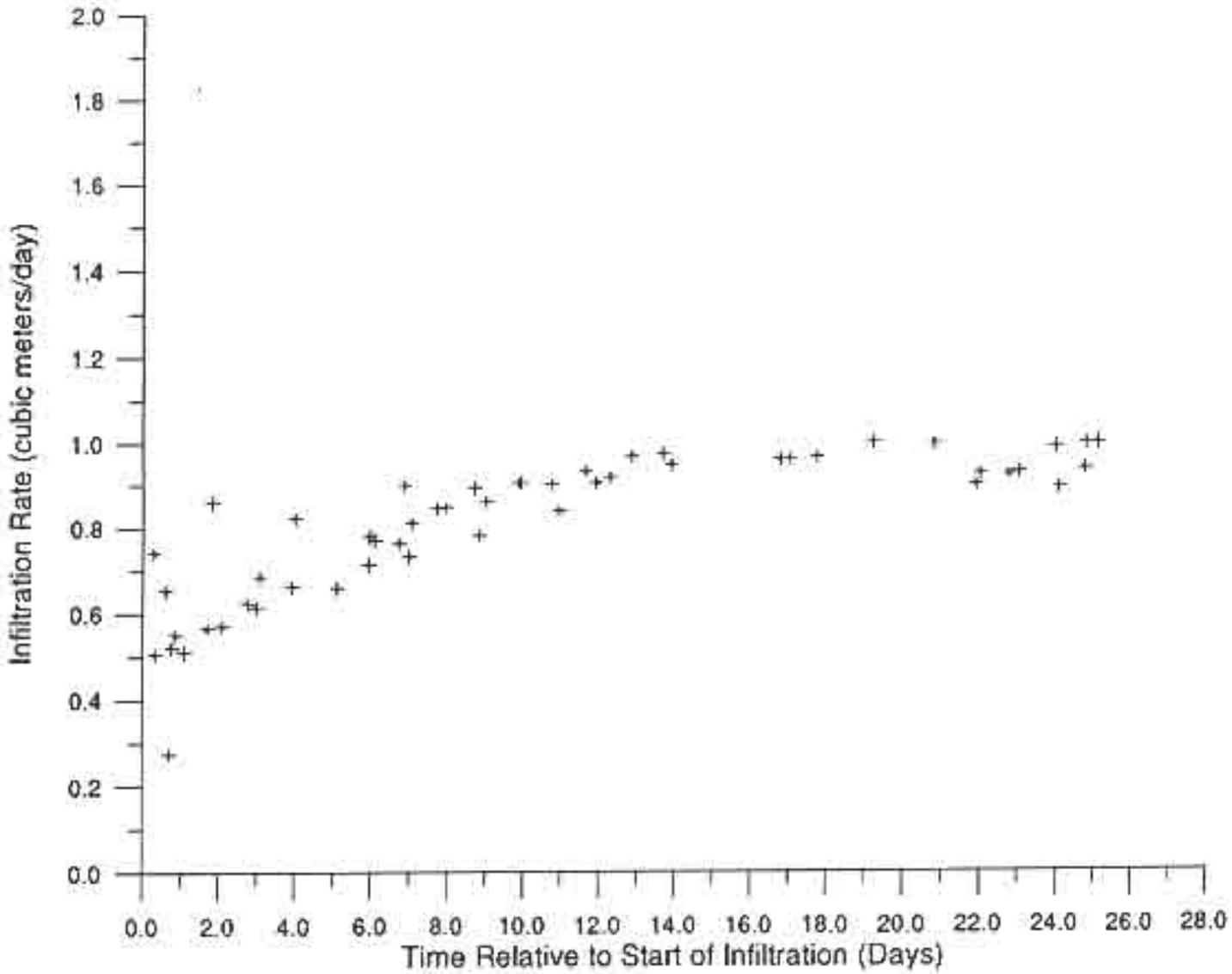

Figure 6.1.1: Infiltration Rates from Manually Measured Supply Tank Water Levels

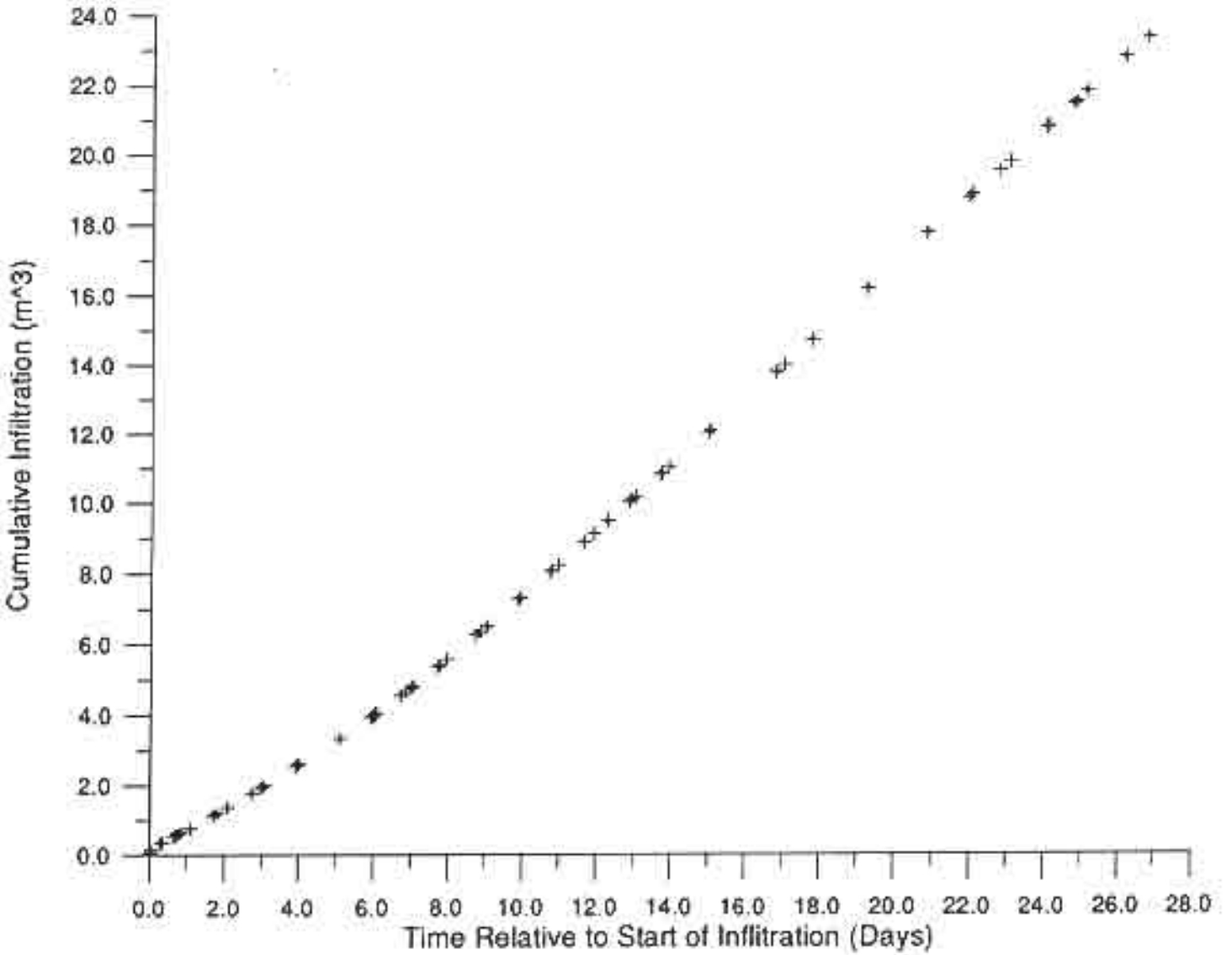

Figure 6.1.2: Cumulative Infiltration from Manually Measured Supply Tank Water Levels

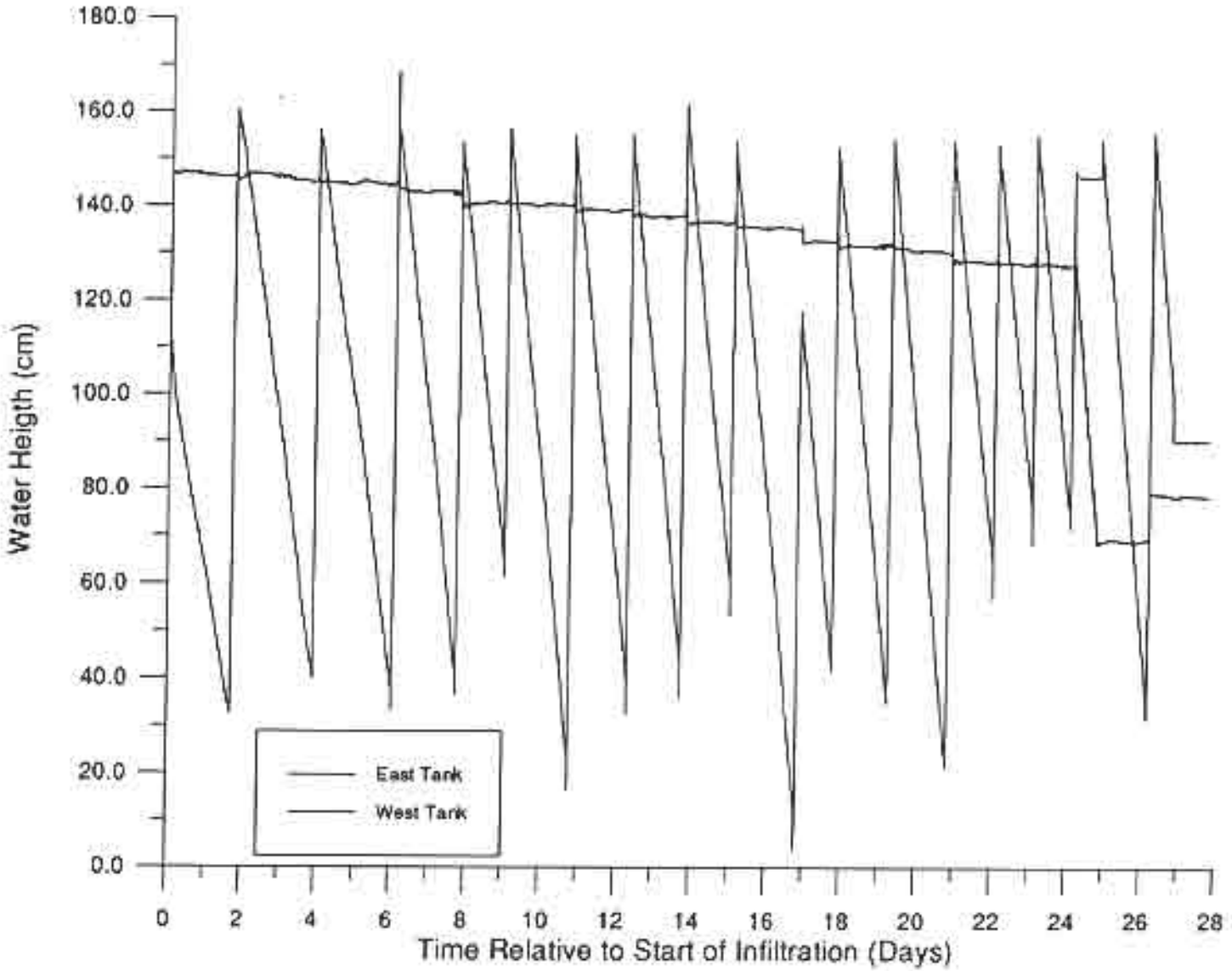

Figure 6.1.3: Infiltrometer Water Supply Tanks Pressure Transducer Data

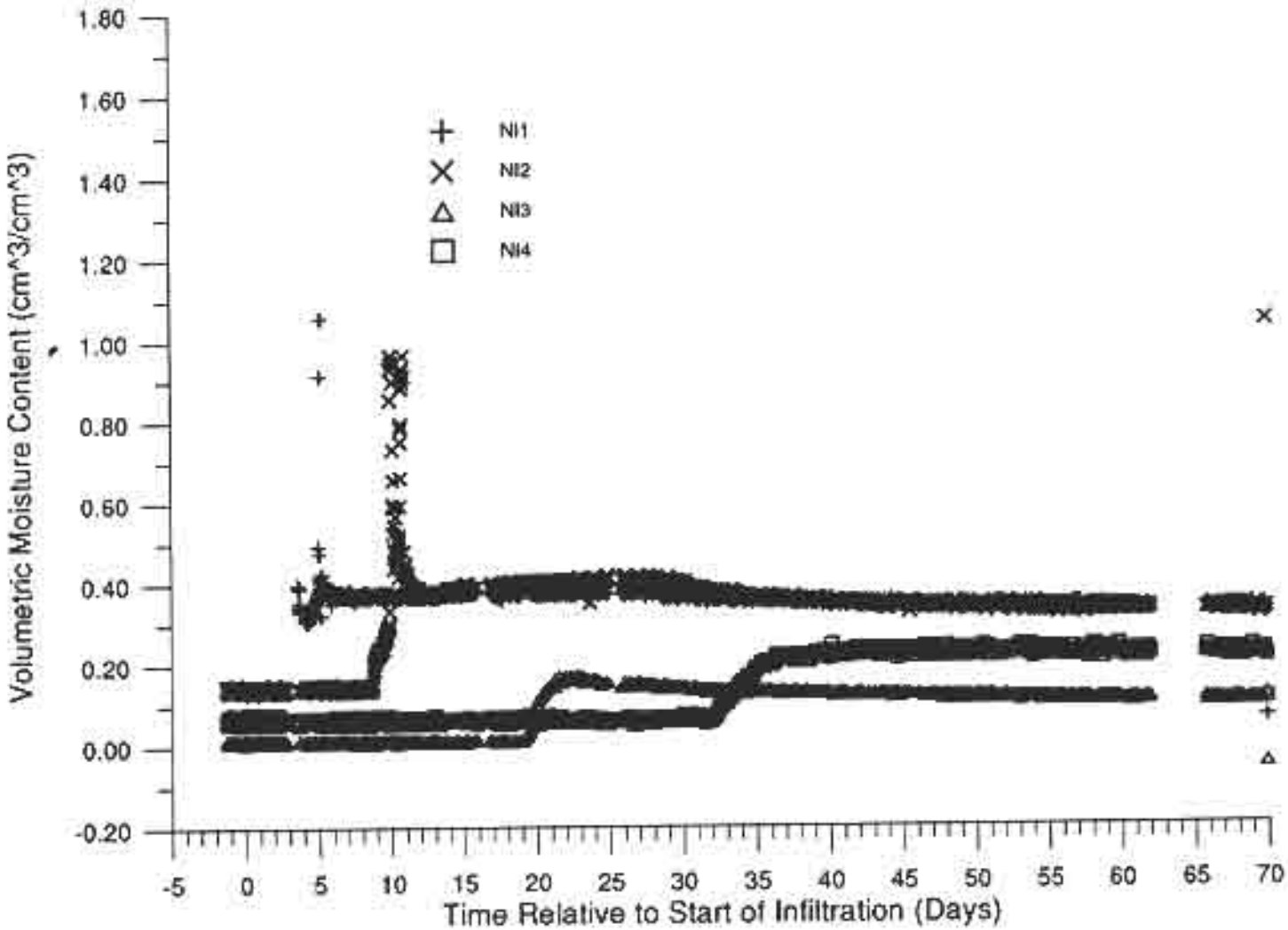

Figure 6.2.1: North Inner TDR Group Moisture Content Results

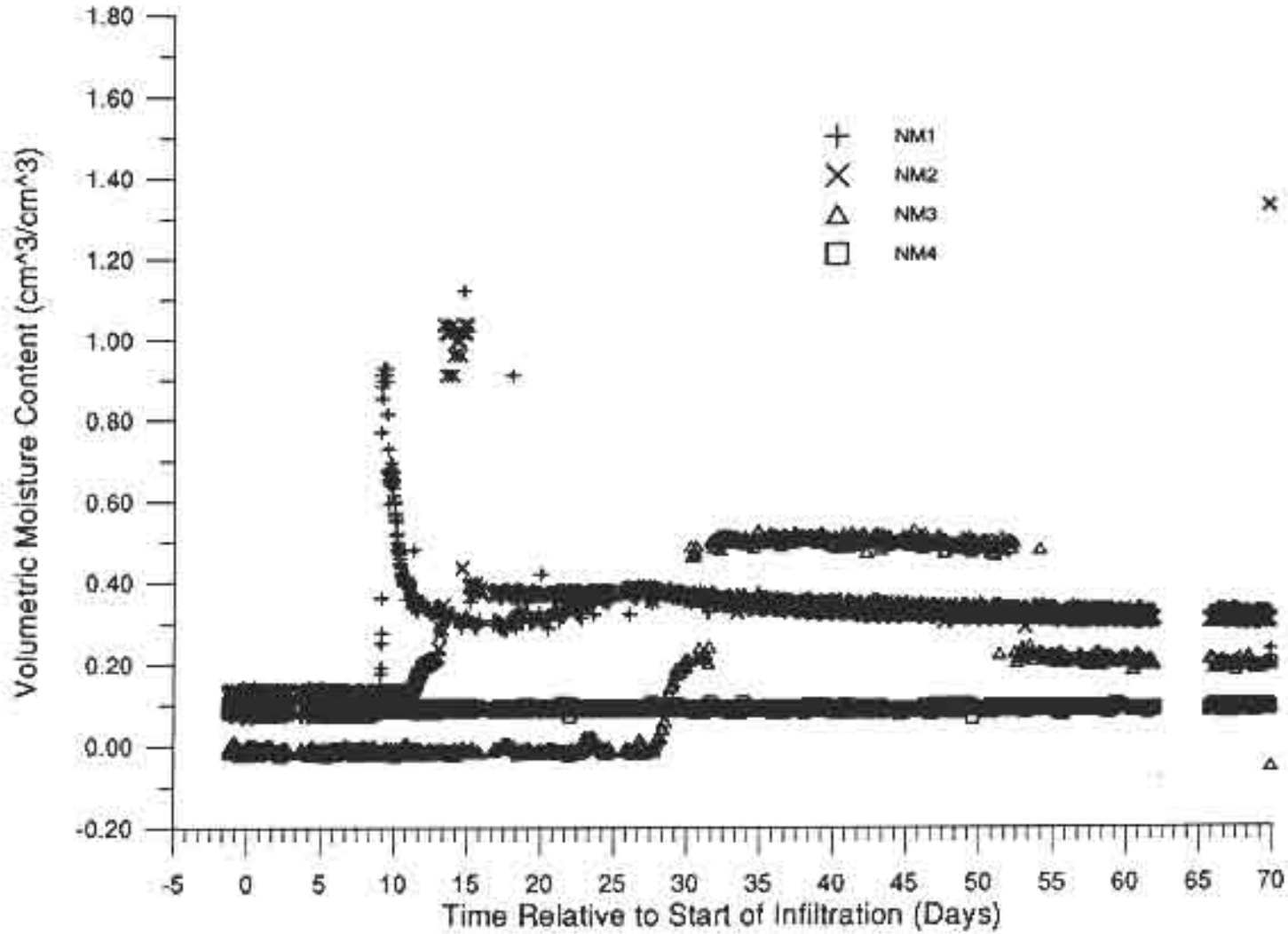

Figure 6.2.2: North Medial TDR Group Moisture Content Results

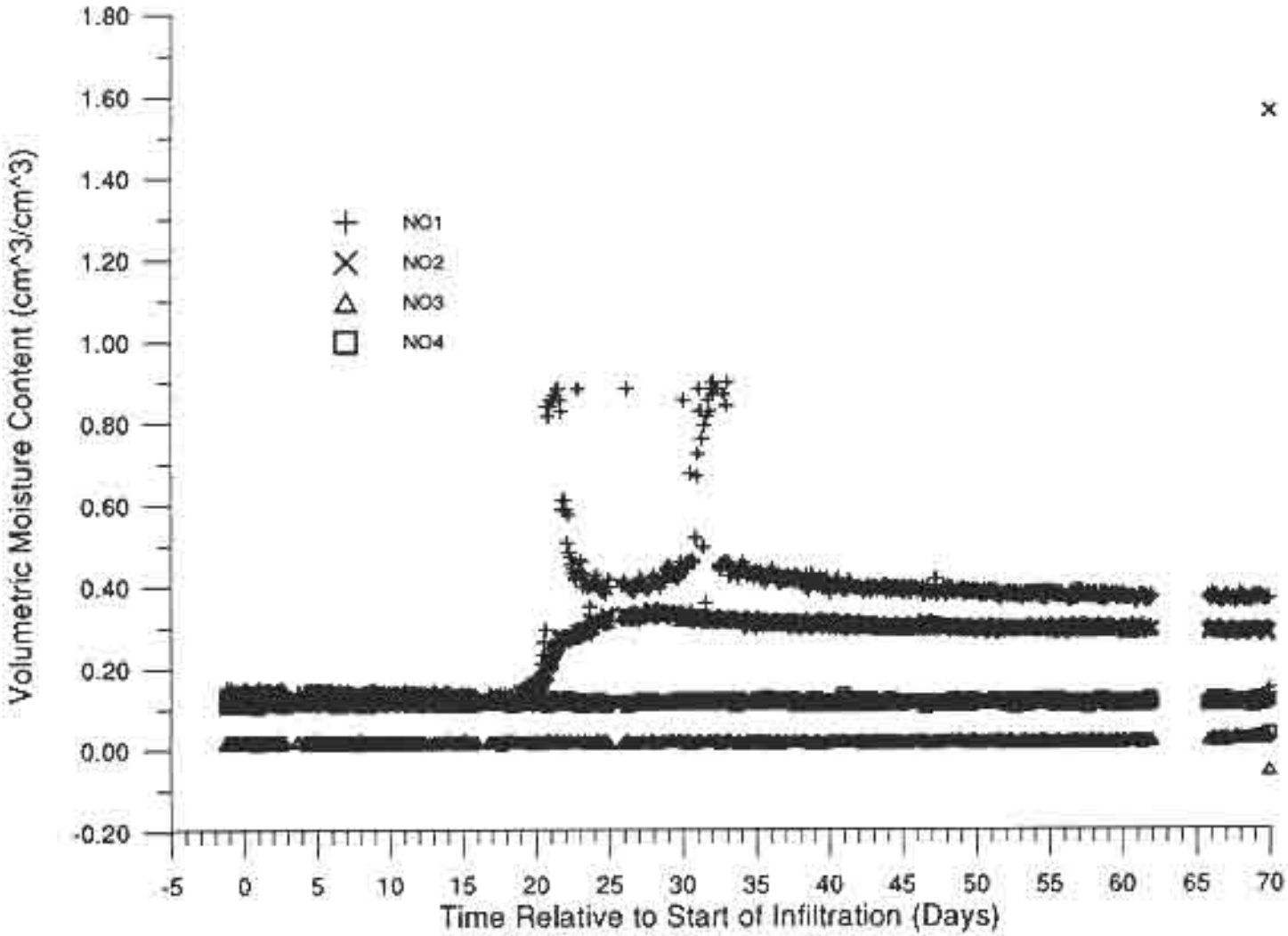

Figure 6.2.3: North Outer TDR Group Moisture Content Results

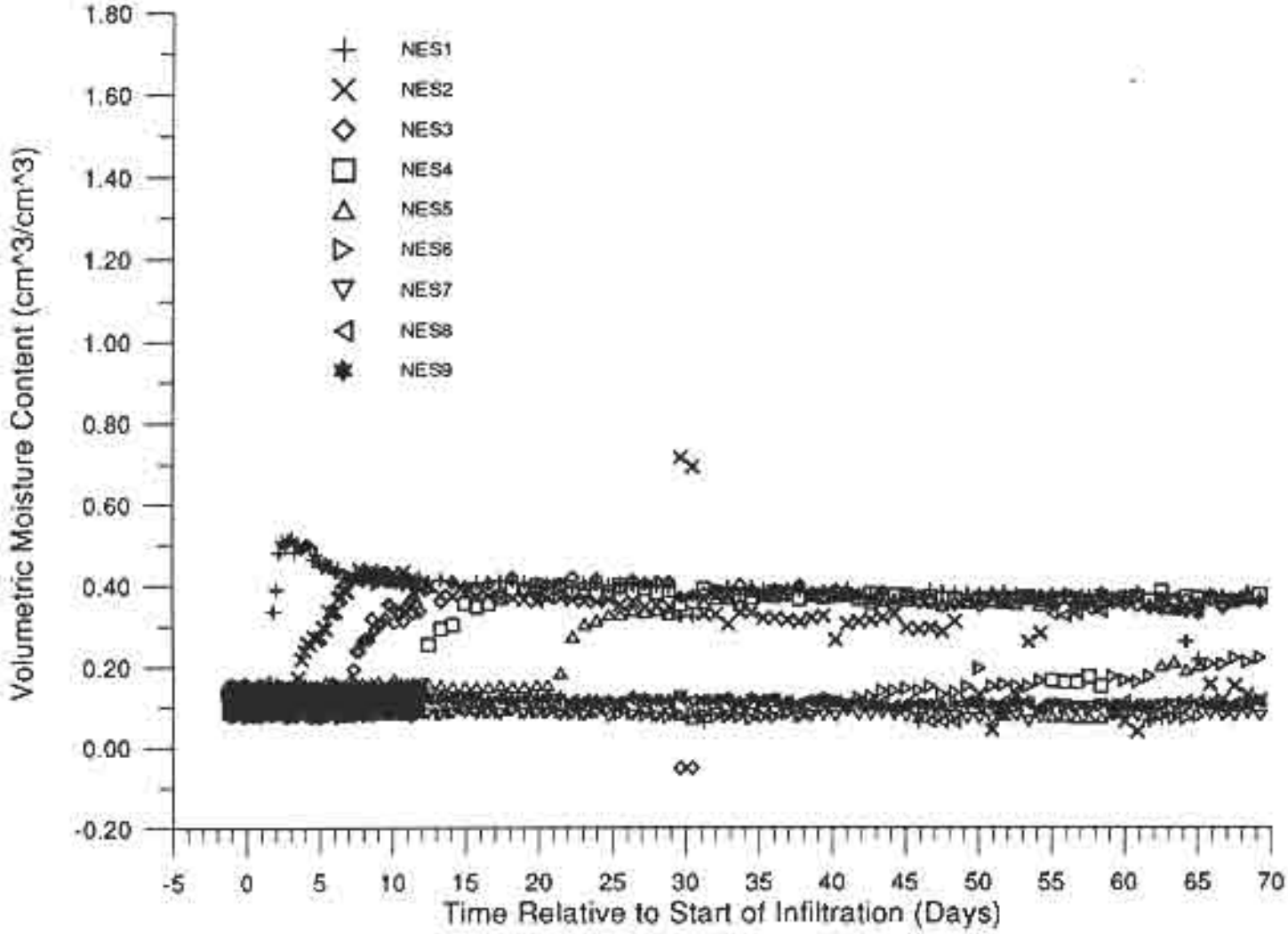

Figure 6.2.4: Northeast Radial TDR Array Moisture Content Results

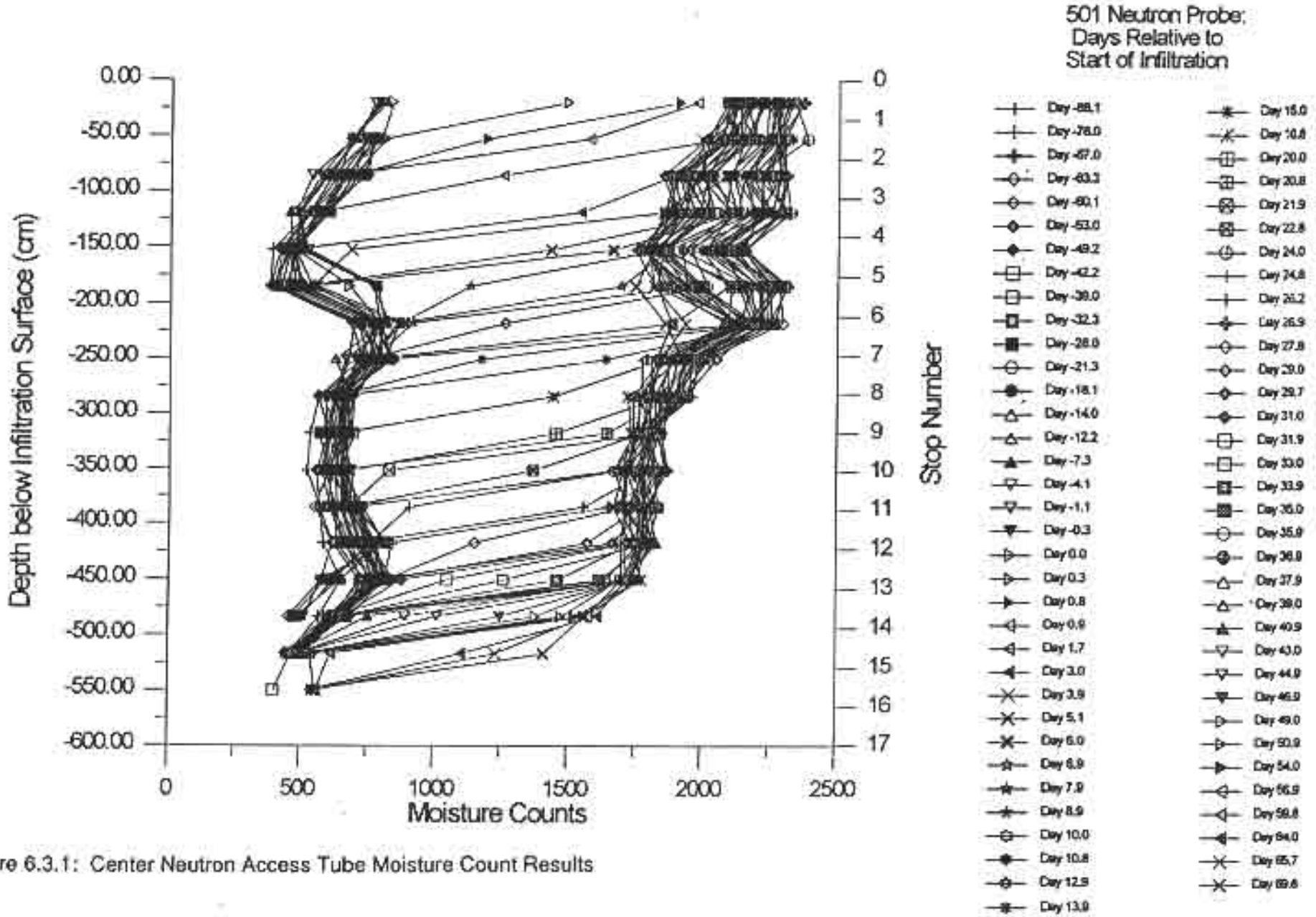

Figure 6.3.1: Center Neutron Access Tube Moisture Count Results

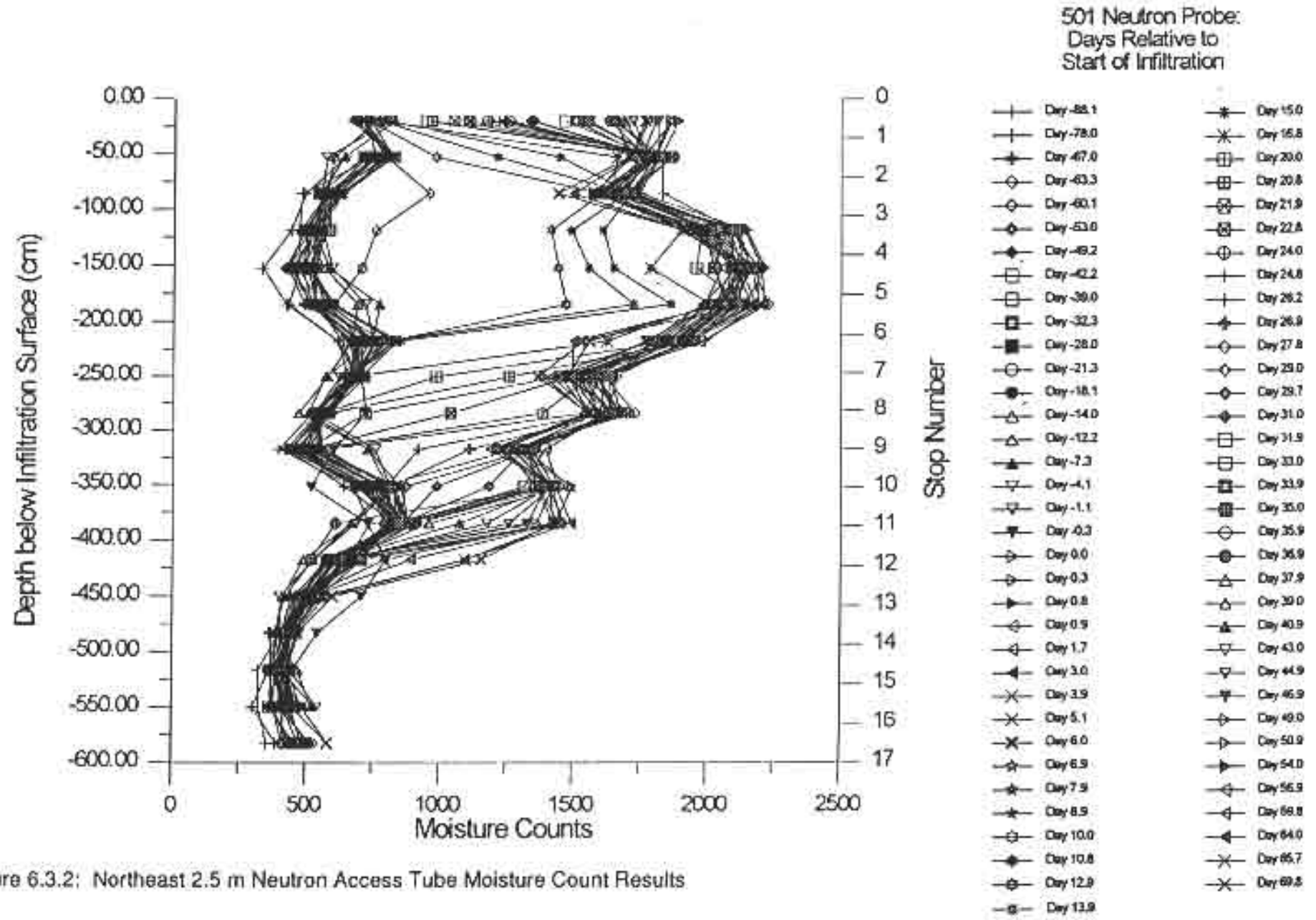

Figure 6.3.2: Northeast 2.5 m Neutron Access Tube Moisture Count Results

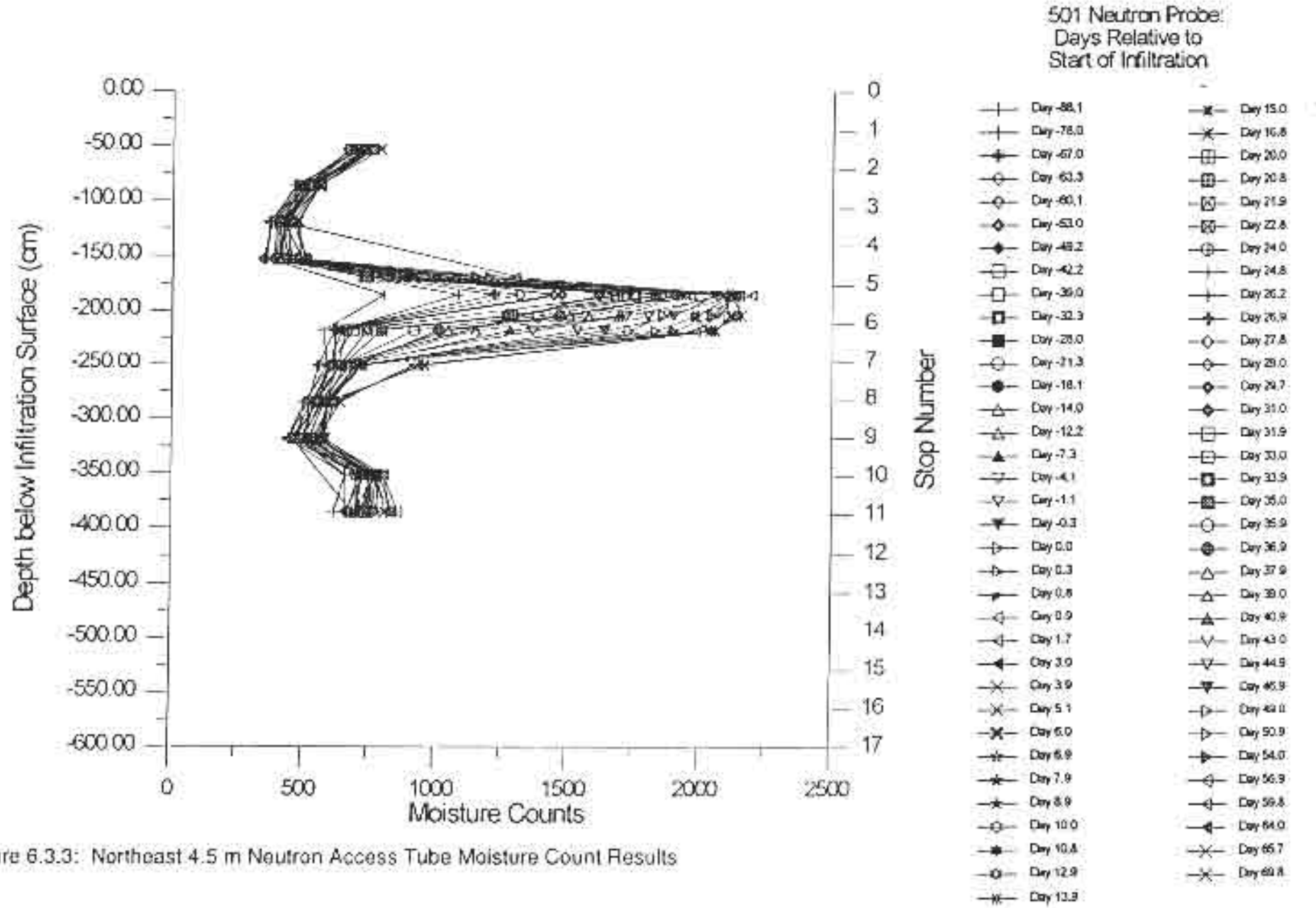

Figure 6.3.3: Northeast 4.5 m Neutron Access Tube Moisture Count Results

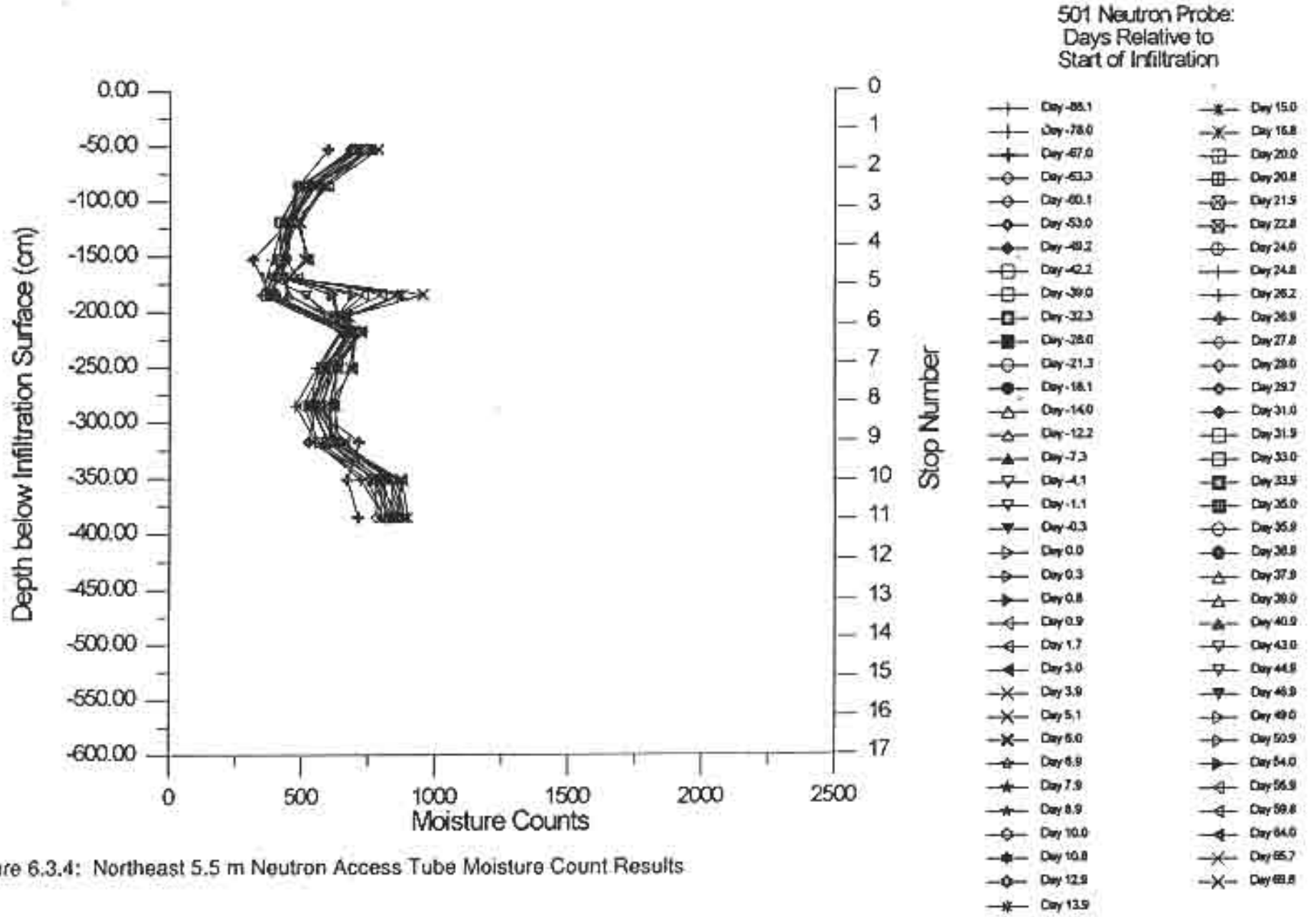

Figure 6.3.4: Northeast 5.5 m Neutron Access Tube Moisture Count Results

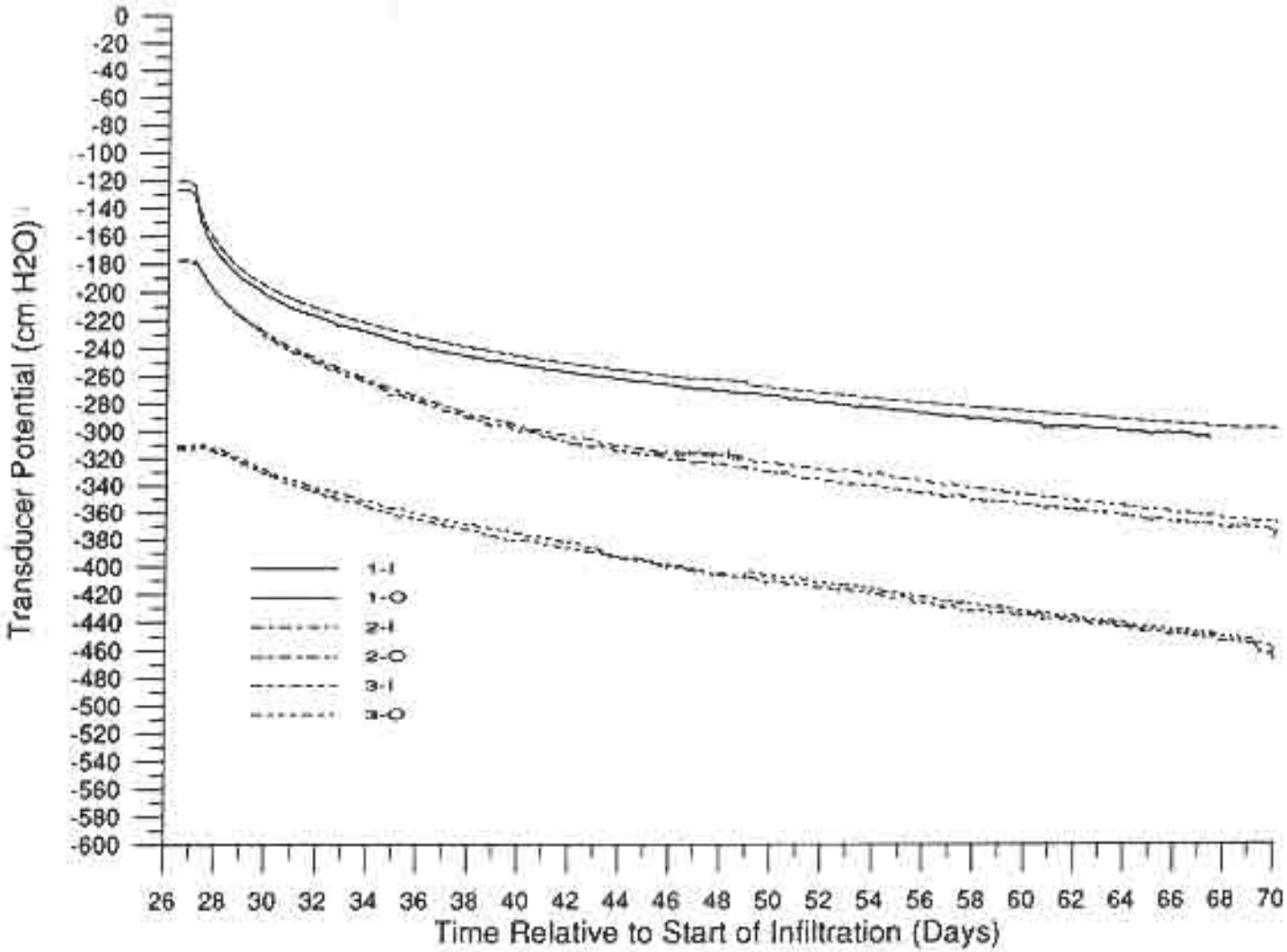

Figure 6.4.1: North Inner Tensiometer Group Transducer Potential Results

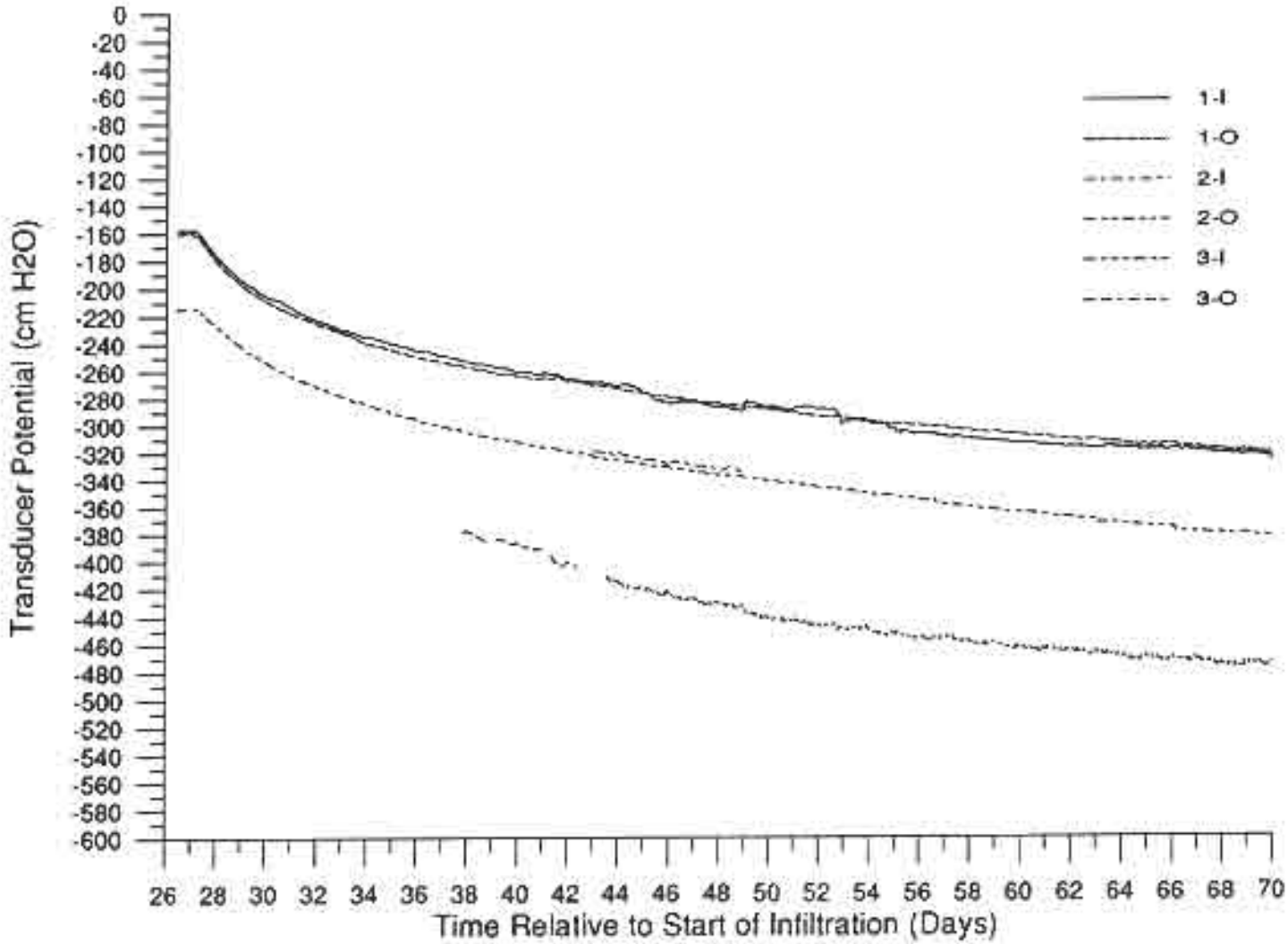

Figure 6.4.2: North Medial Tensiometer Group Transducer Potential Results

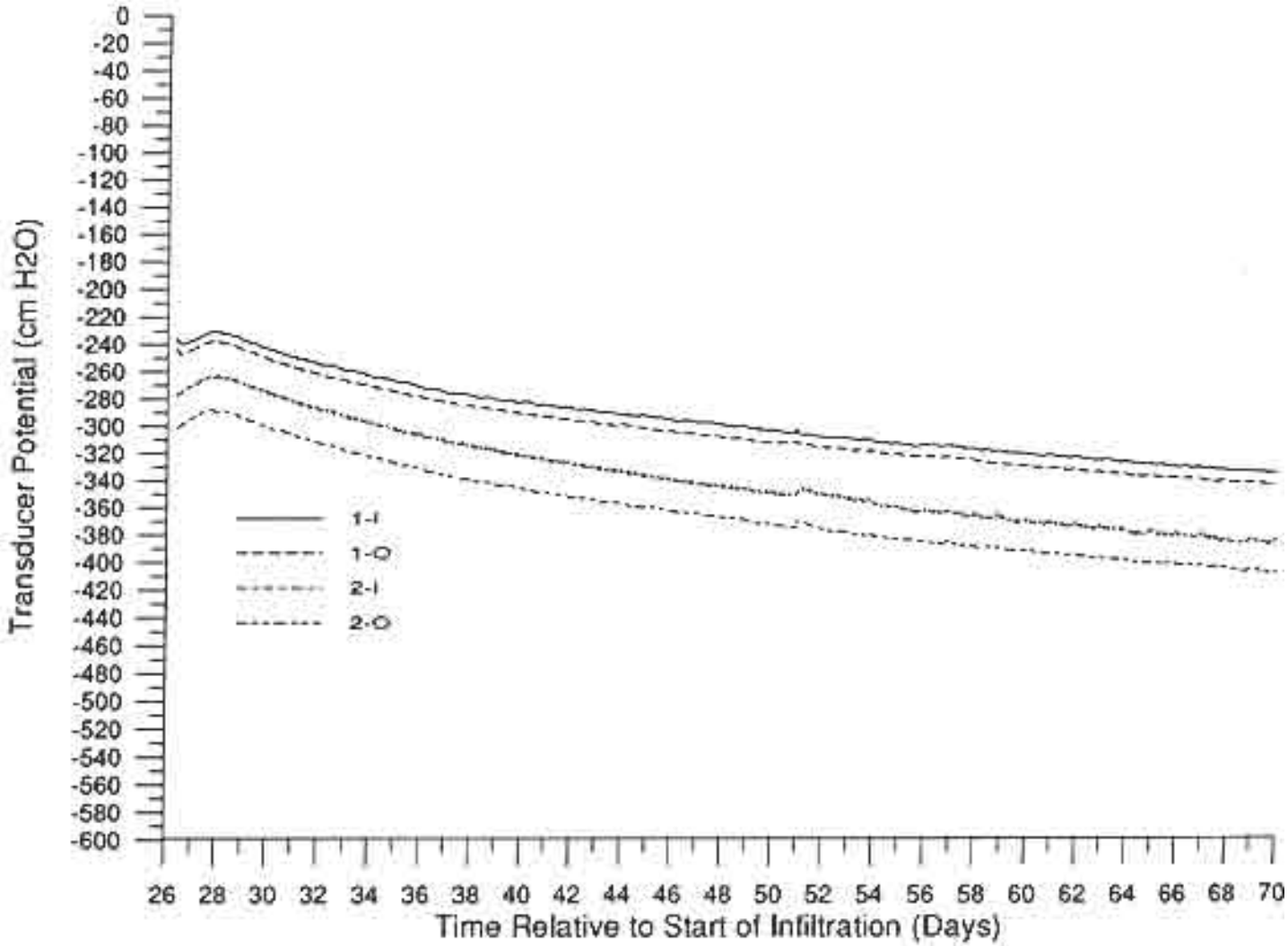

Figure 6.4.3: North Outer Tensiometer Group Transducer Potential Results

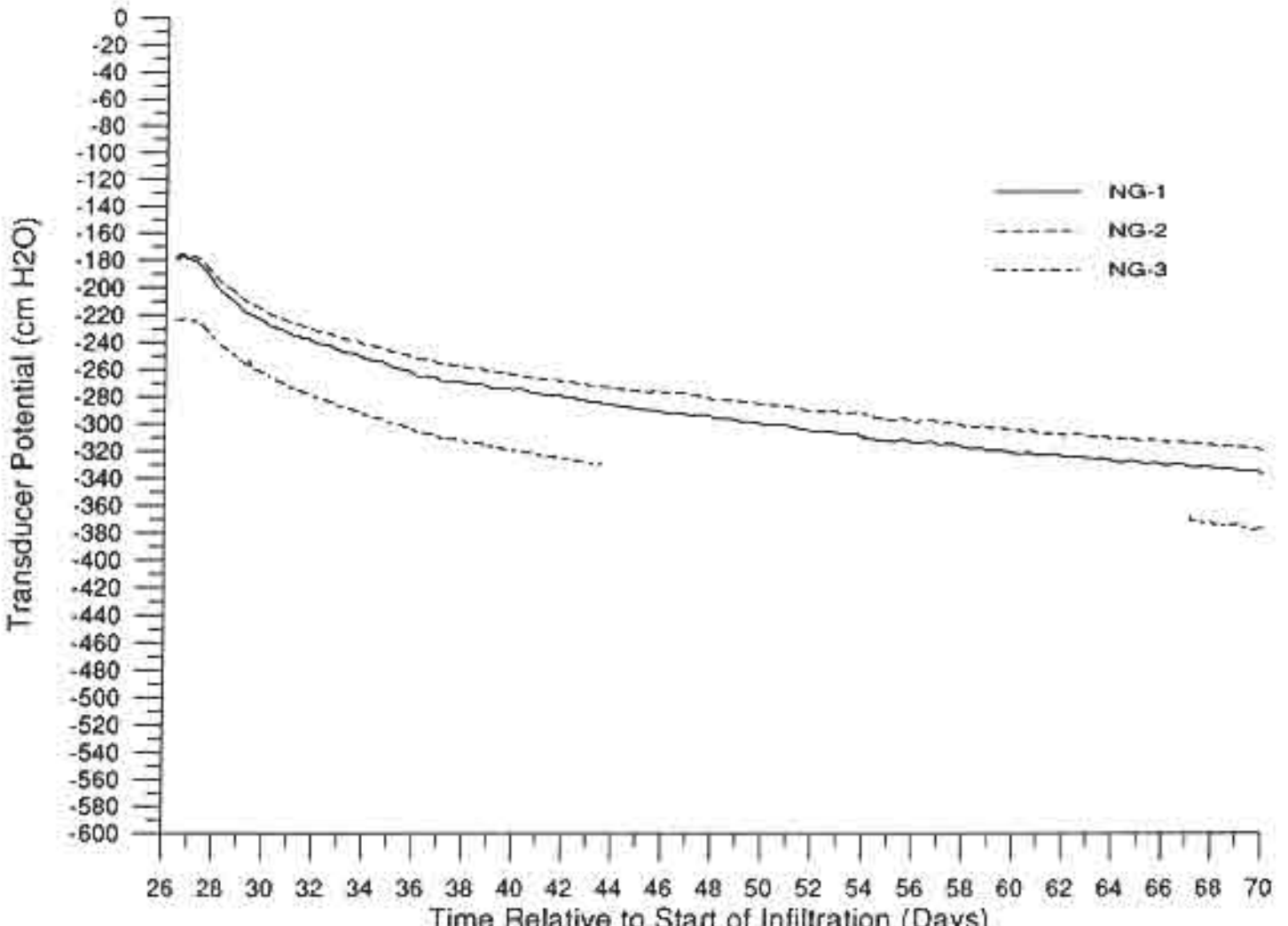

Figure 6.4.4: North Geology Tensiometer Group Transducer Potential Results

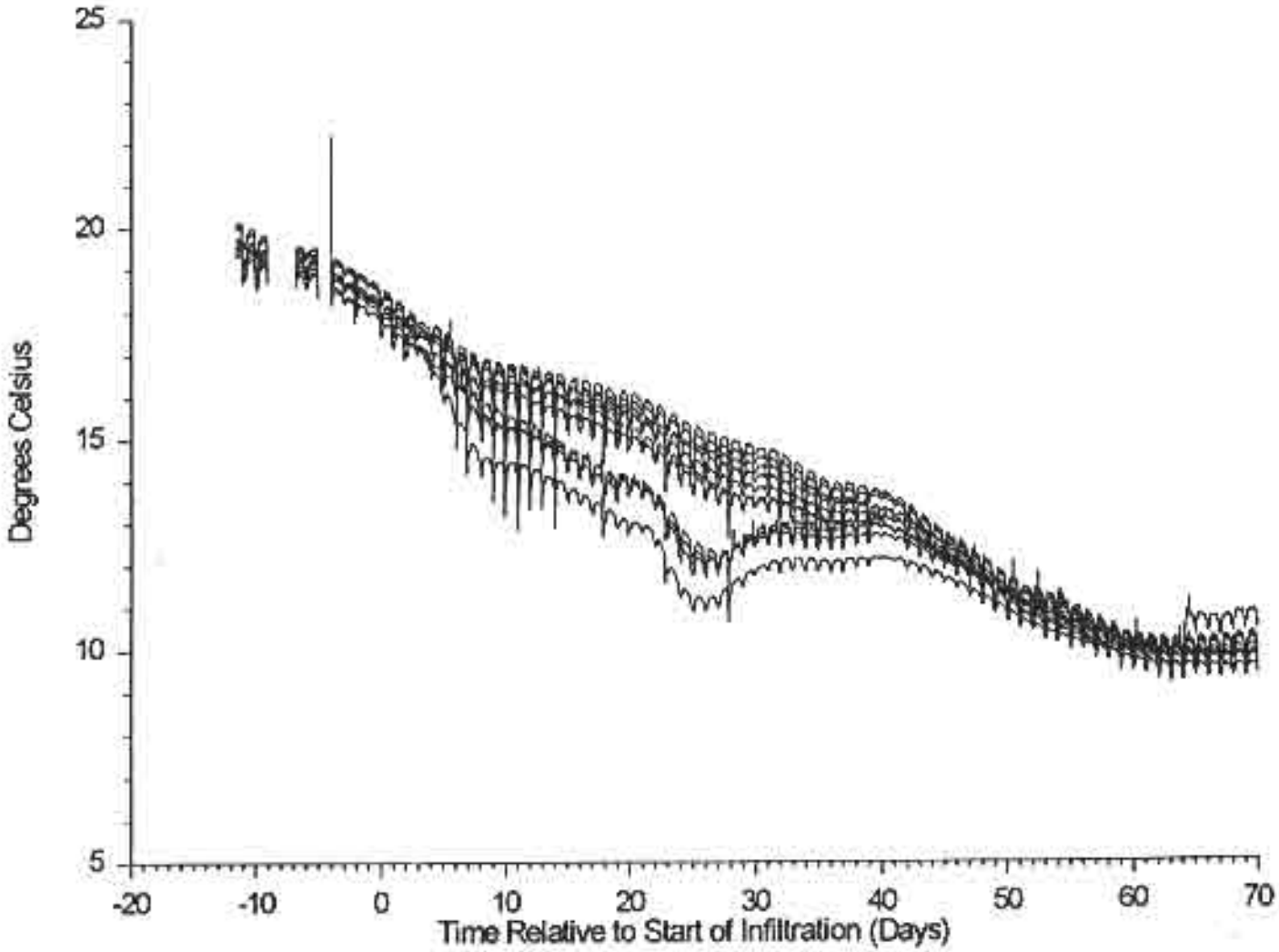

Figure 6.5.1: 1 Meter (1m) Thermocouple Data

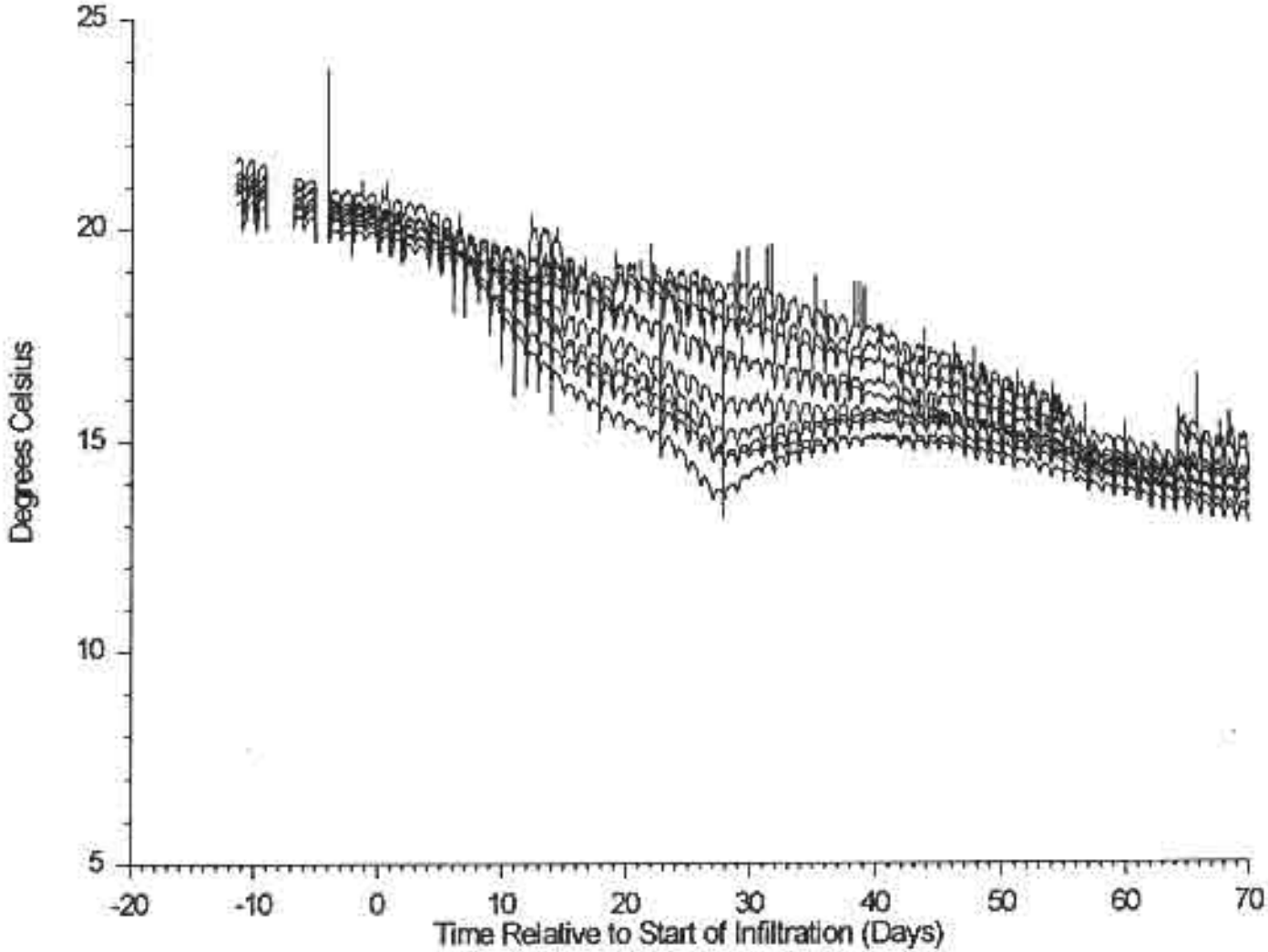

Figure 6.5.2: 2 Meter (2m) Thermocouple Data

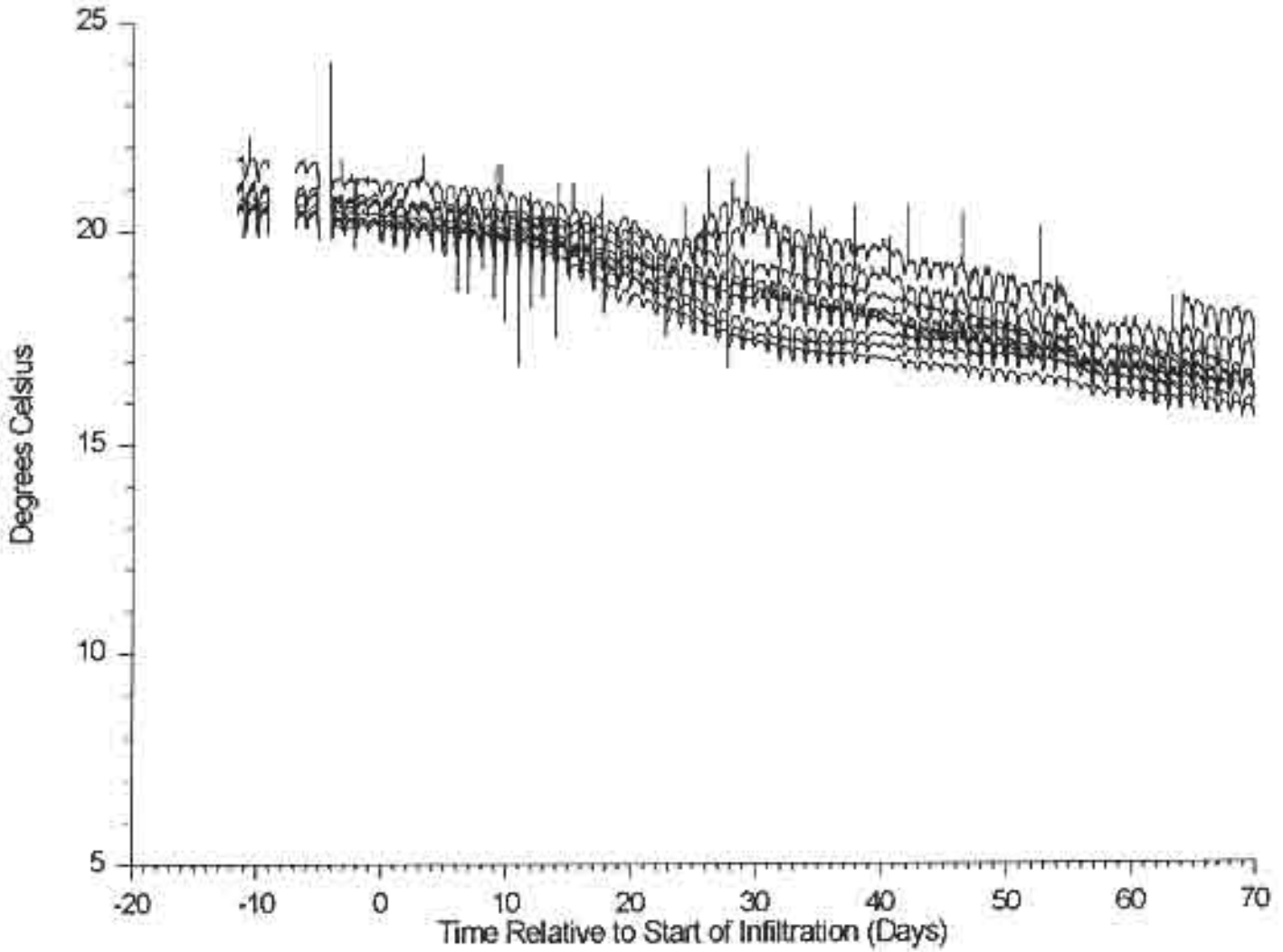

Figure 6.5.3: 3 Meter (3m) Thermocouple Data

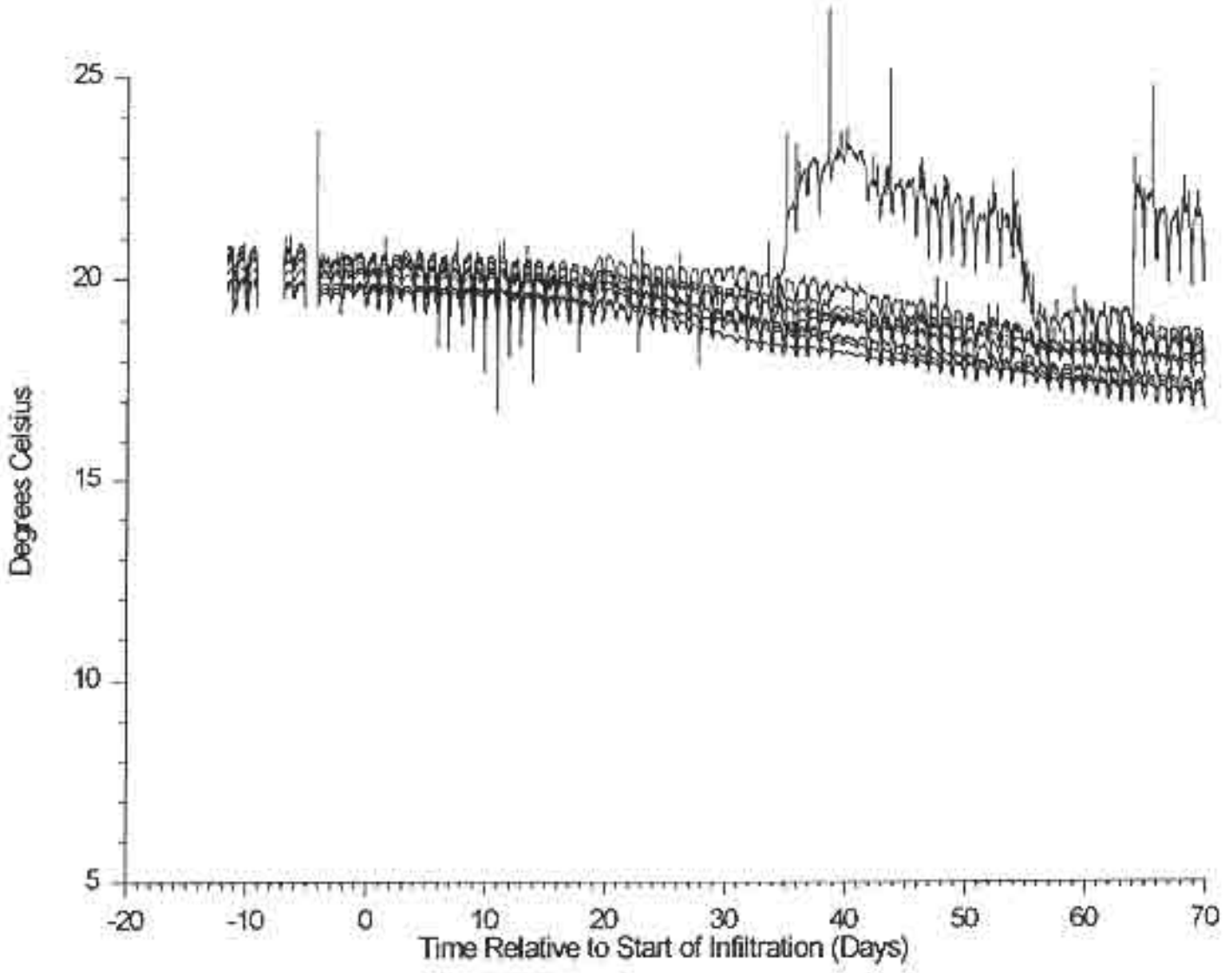

Figure 6.5.4: 4 Meter (4m) Thermocouple Data

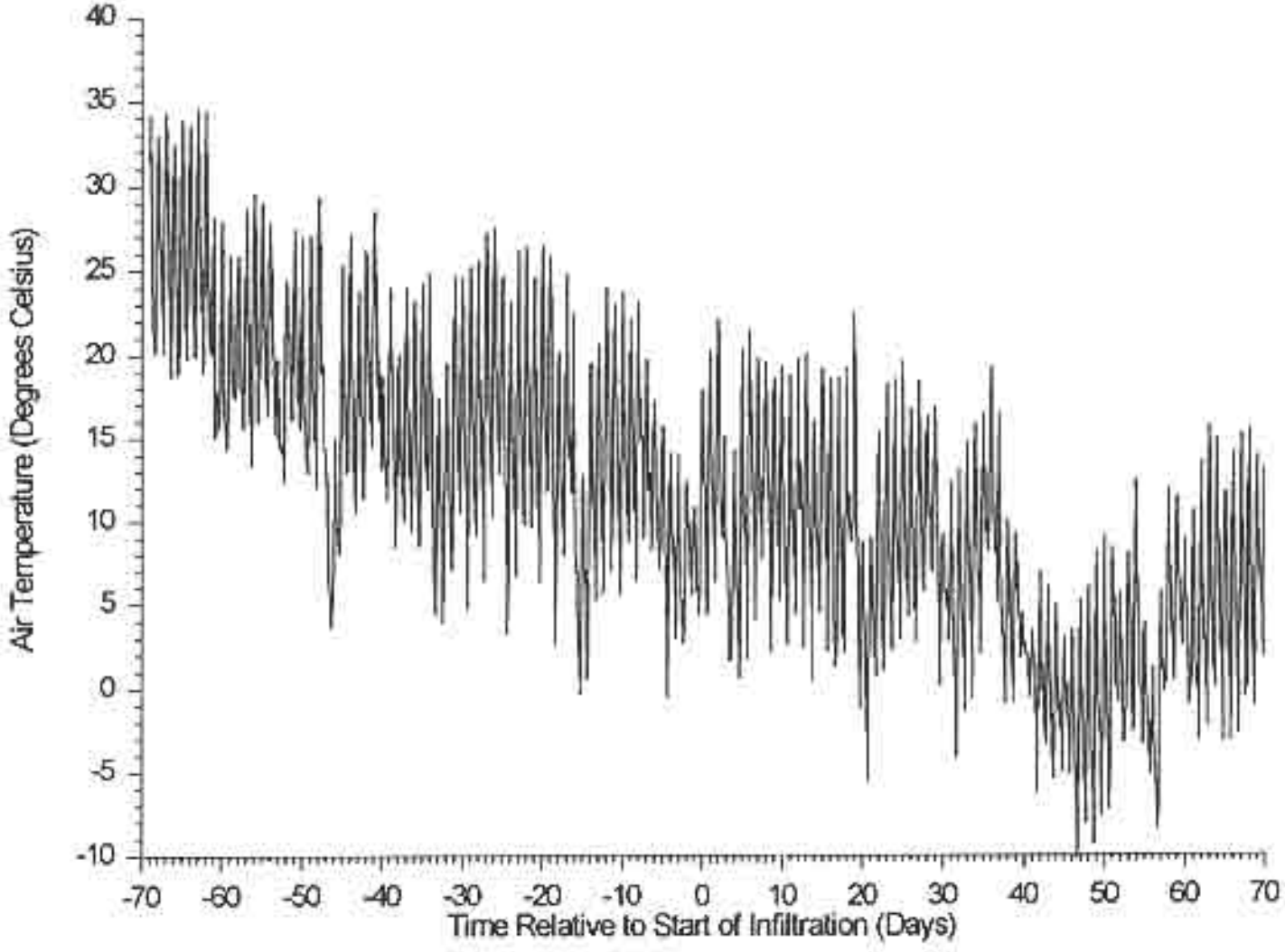

Figure 6.6.1: Weather Station Air Temperature Data

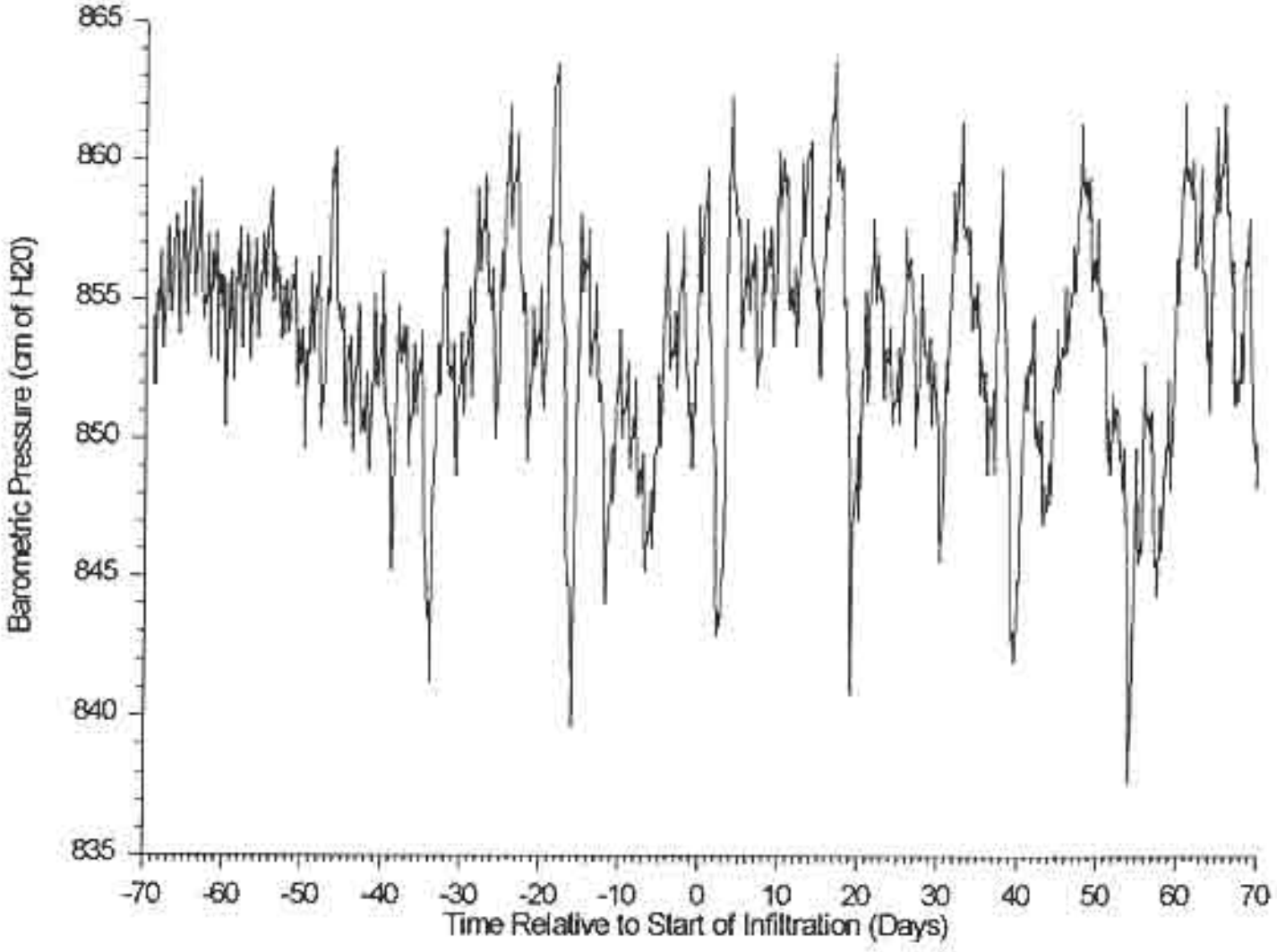

Figure 6.6.2: Weather Station Barometric Pressure Data

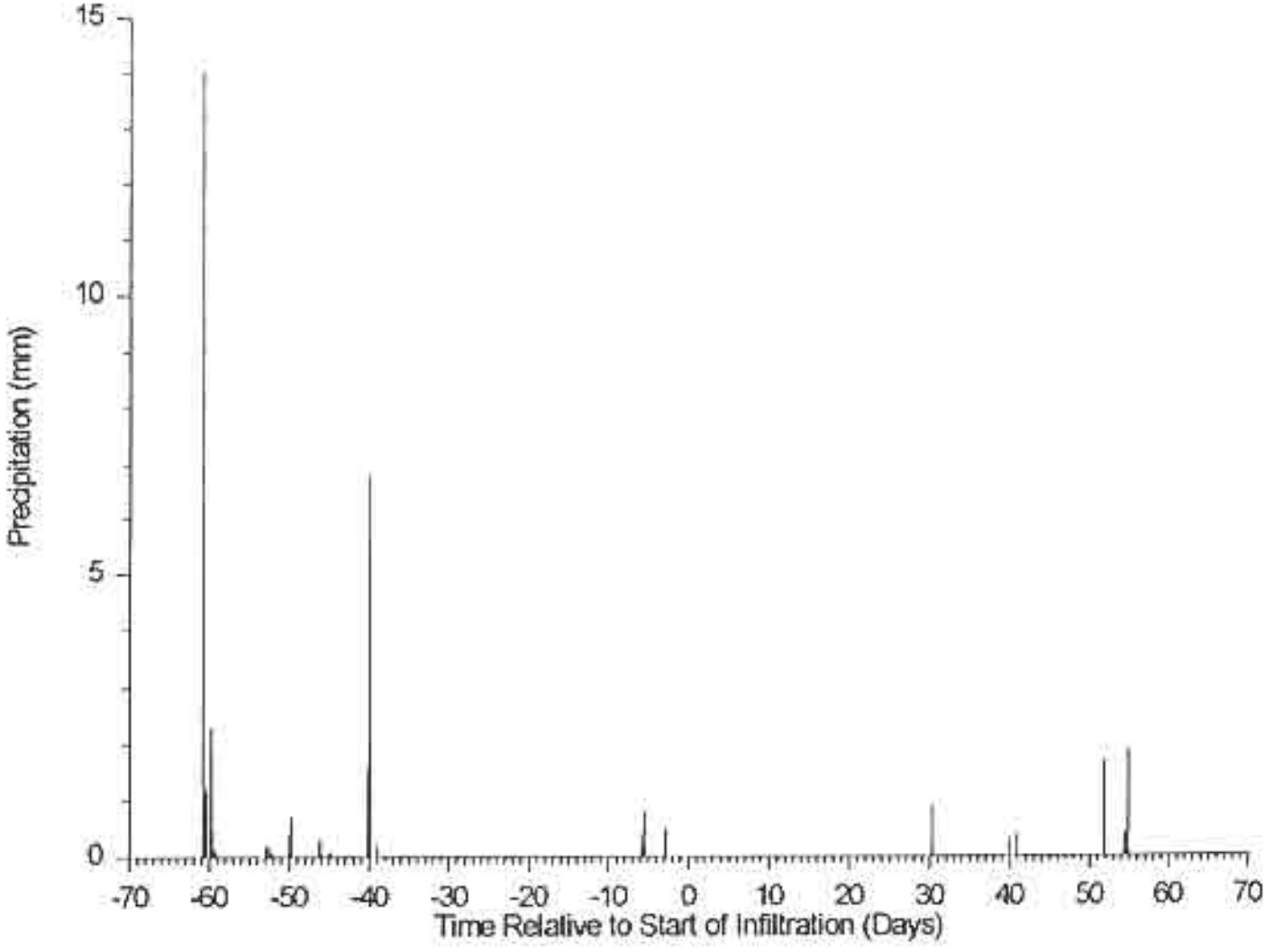

Figure 6.6.3: Weather Station Precipitation Data

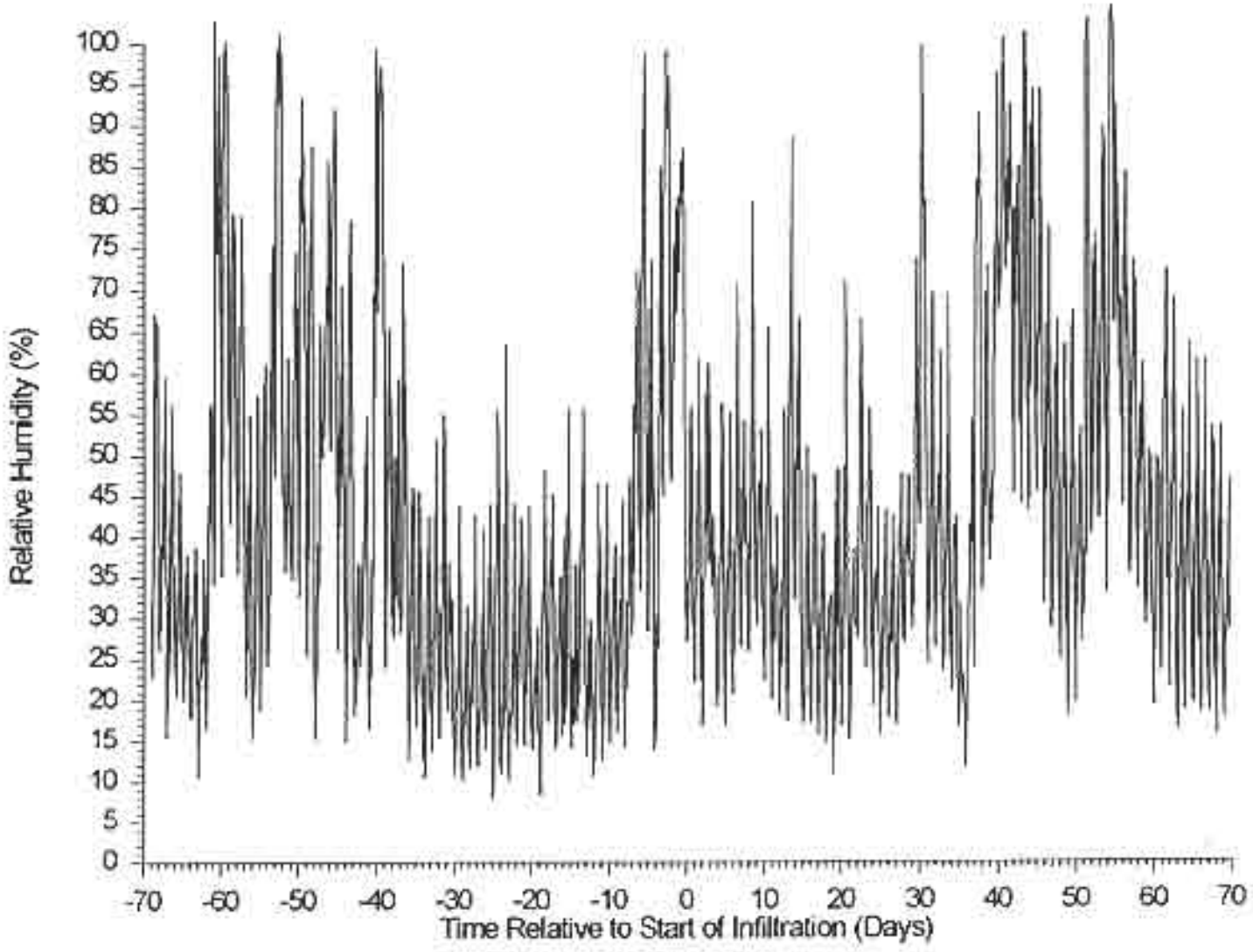

Figure 6.6.4: Weather Station Relative Humidity Data

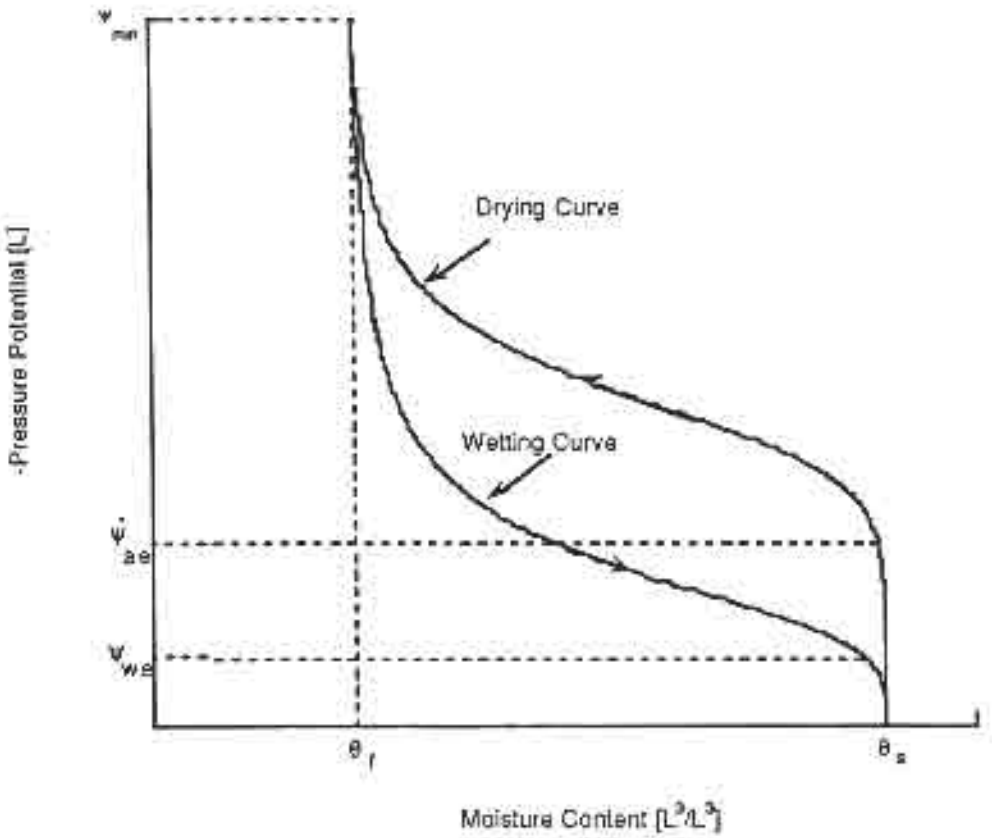

Figure 7.1: The suction-moisture content curves for the Main Wetting Curve (MWC) and Main Drainage Curve (MDC) forming the hysteresis loop.

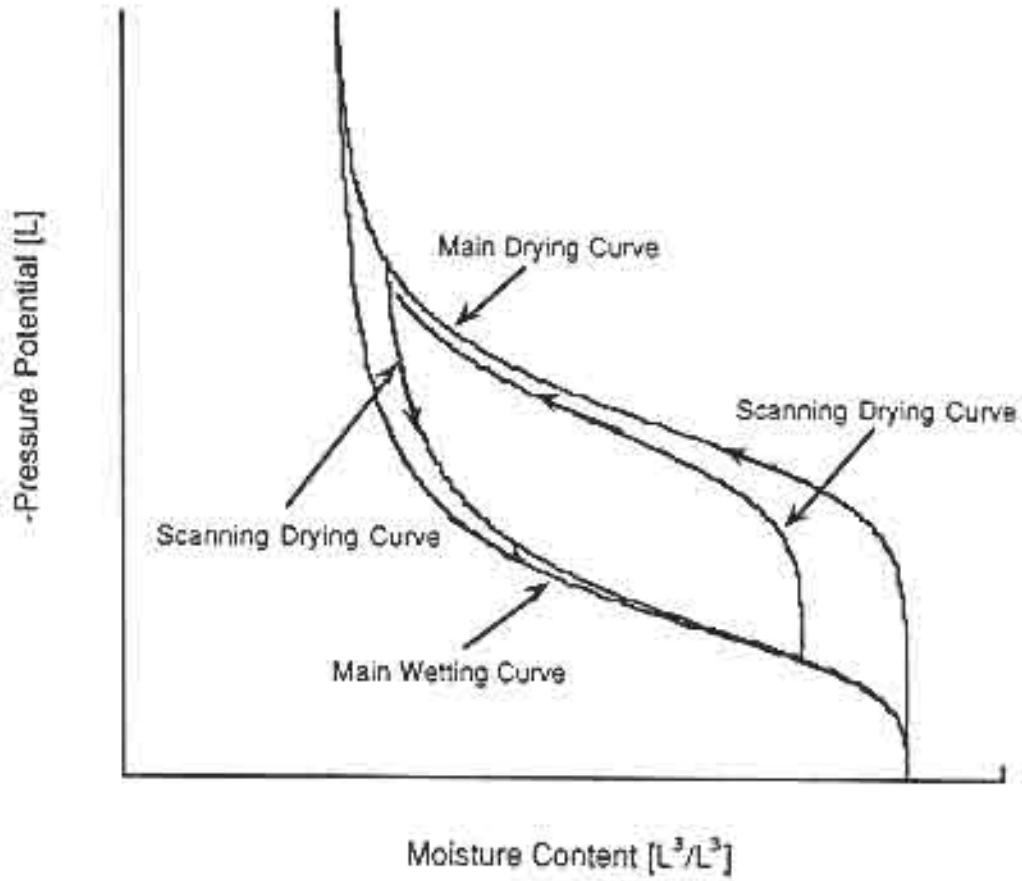

Figure 7.2: The suction-moisture content curves for the hysteresis loop and two scanning curves.

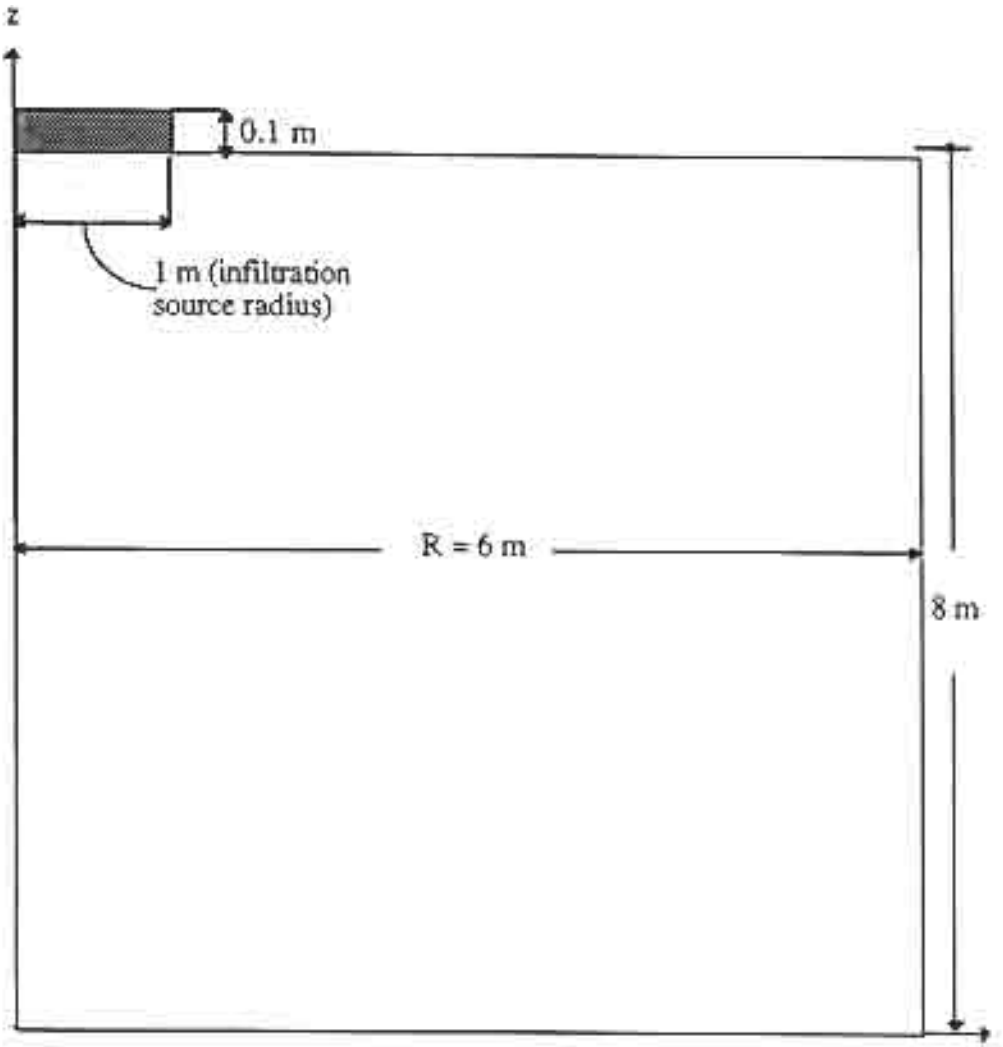

Figure 7.3: Schematic of the model problem in axi-symmetric cylindrical coordinates.

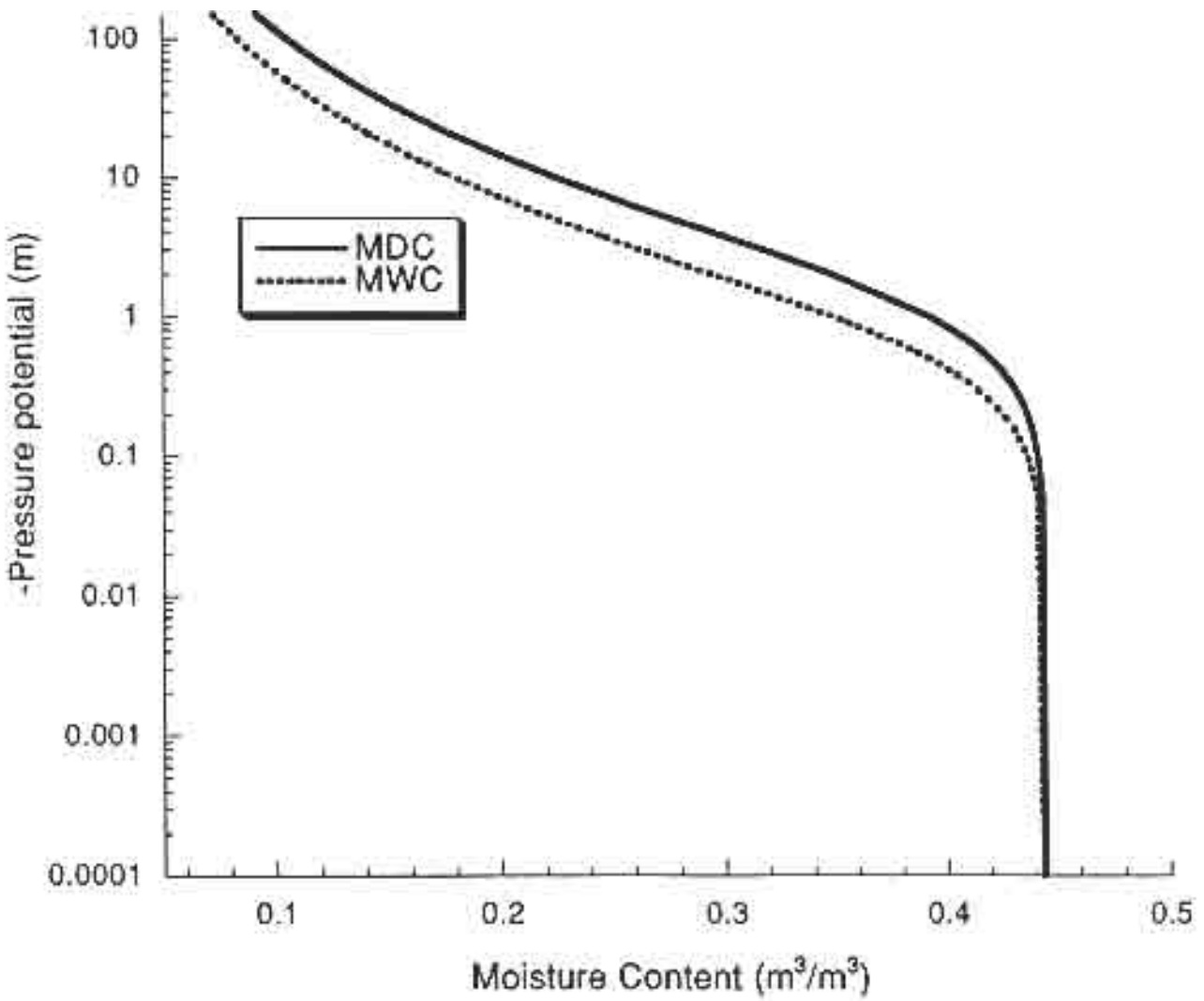

Figure 7.4: Pressure versus moisture content curves for TA-1 Undisturbed Sample (MDC from data, MWC predicted from MDC)

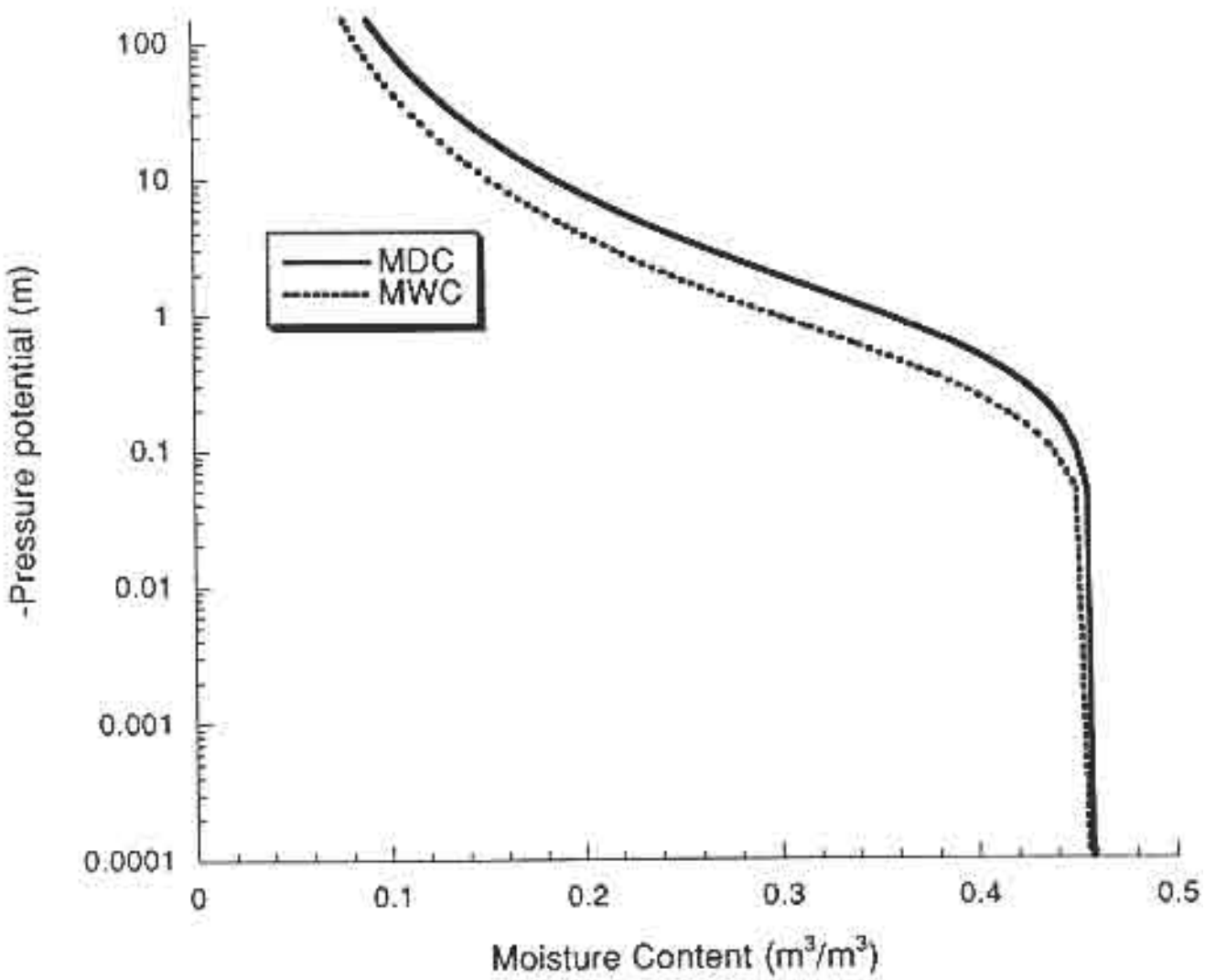

Figure 7.5: Pressure versus moisture content curves for a typical silt (MDC from RETC manual, MWC predicted from MDC)

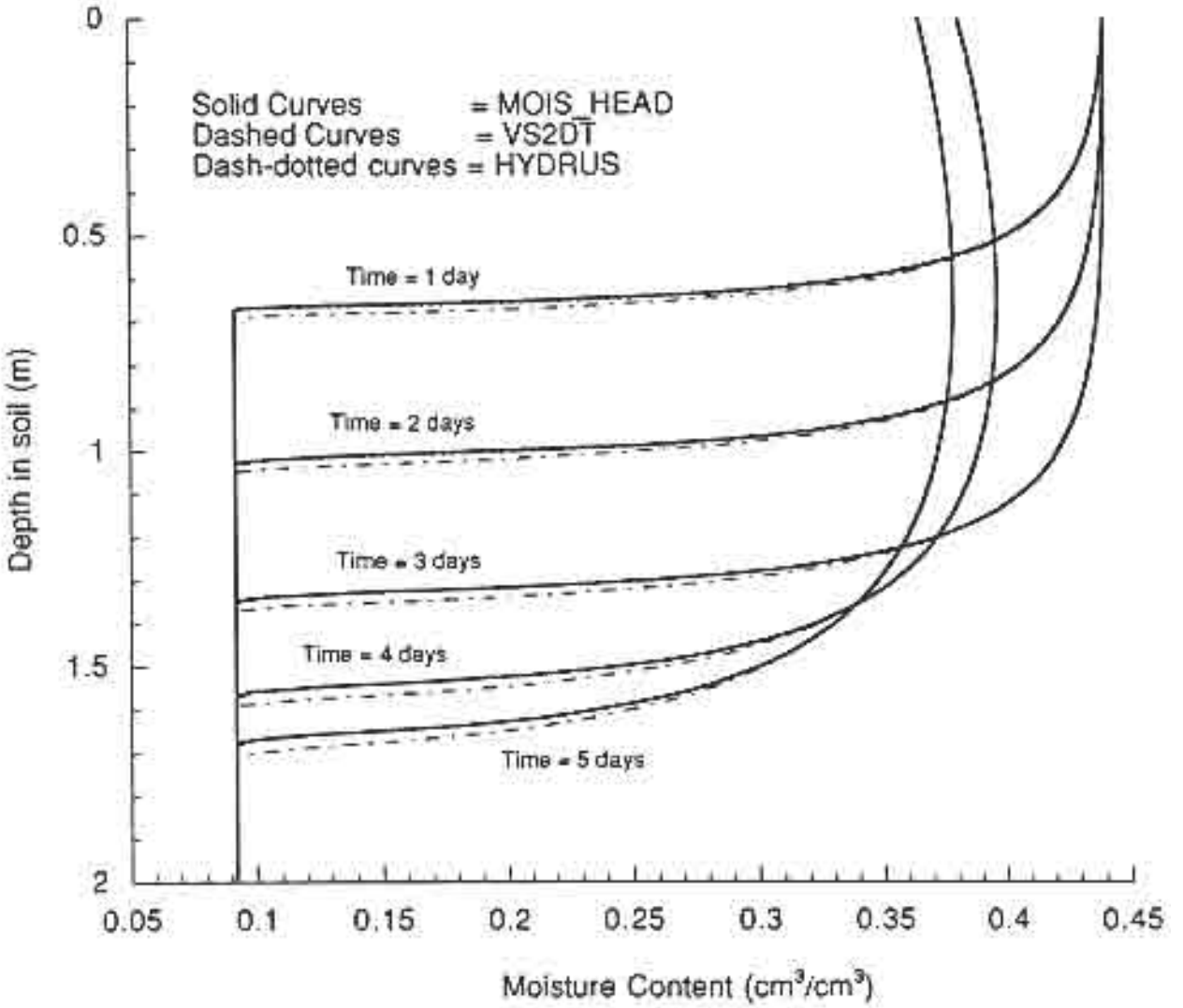

Figure 7.6: Moisture Content as a function of depth.Comparison of three different codes (1-D, nonhysteretic model, htop = -0.1m)

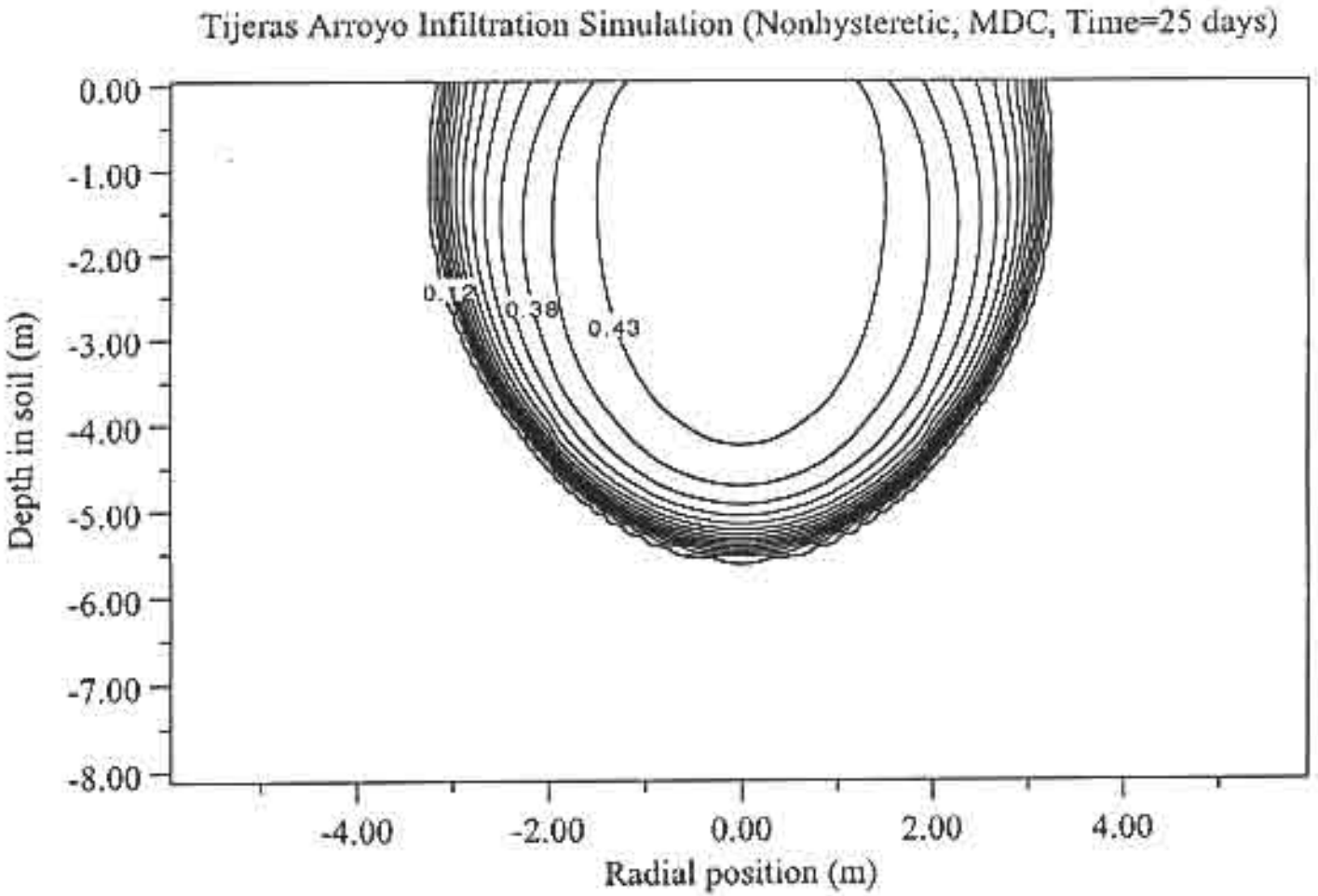

Figure 7.7: Tijeras Arroyo Infiltration Simulation (Nonhysteretic, MDC, Time = 25 days)

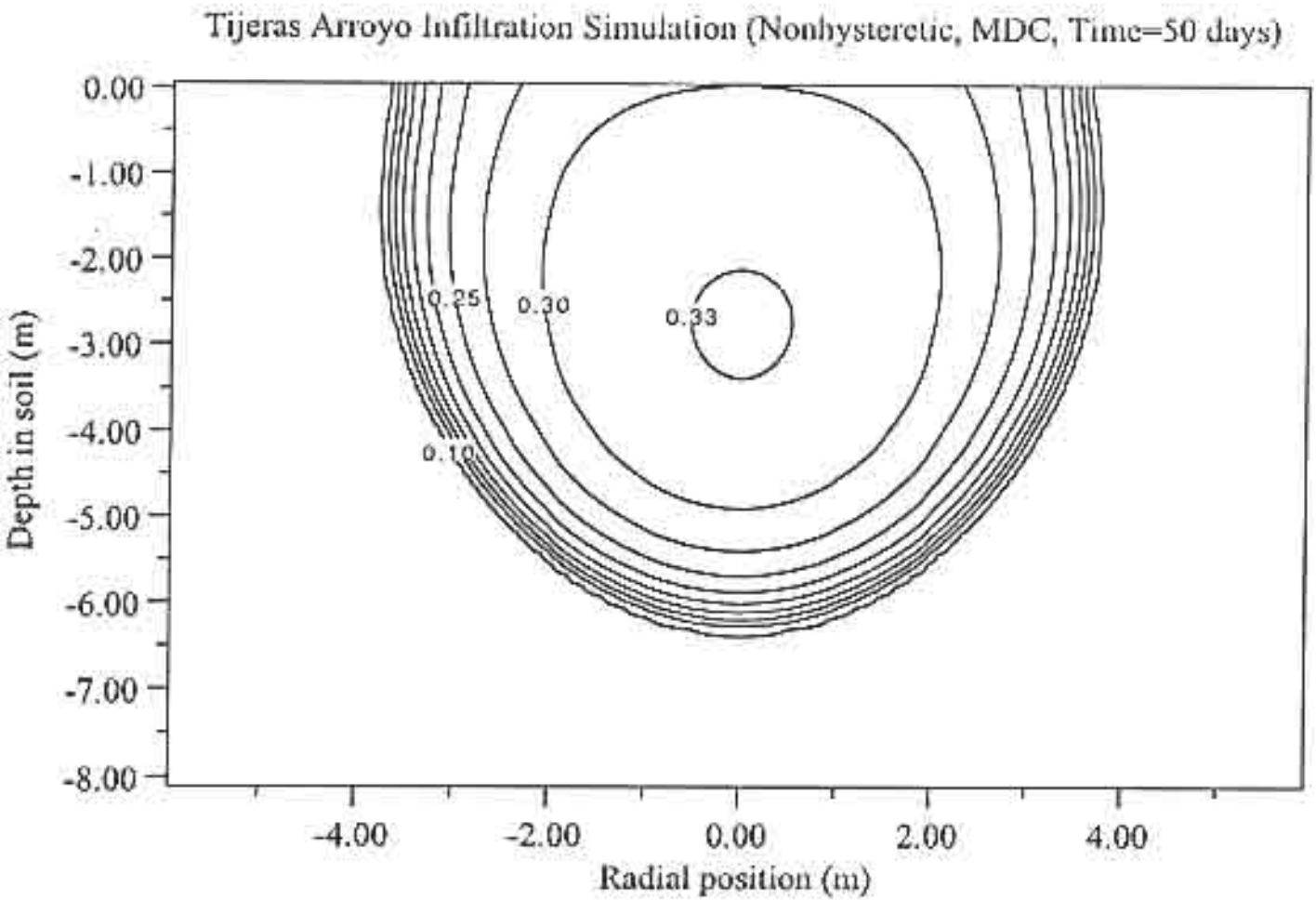

Figure 7.8: Tijeras Arroyo Infiltration Simulation (Nonhysteretic, MDC, Time = 50 days)

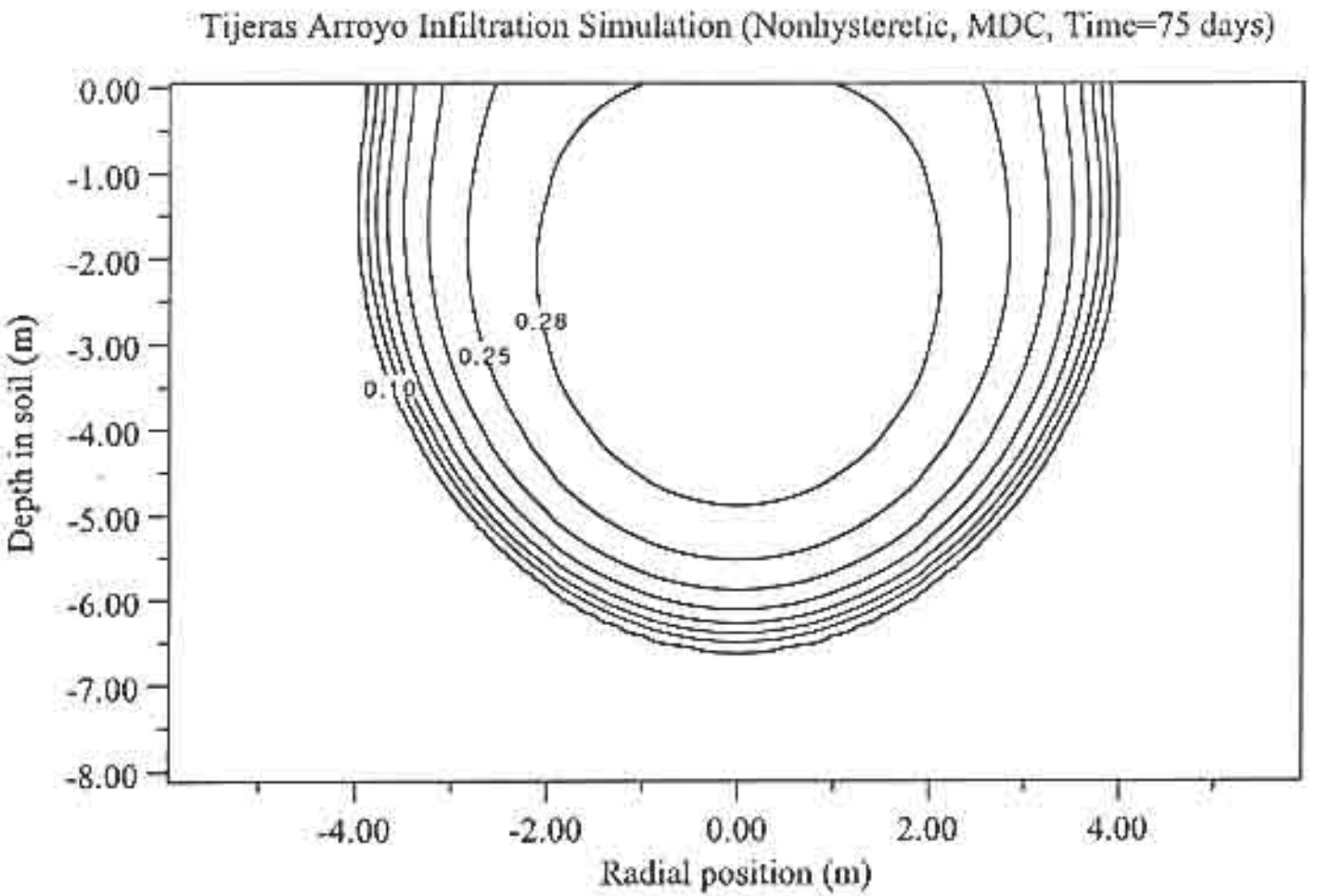

Figure 7.9: Tijeras Arroyo Infiltration Simulation (Nonhysteretic, MDC, Time = 75 days)

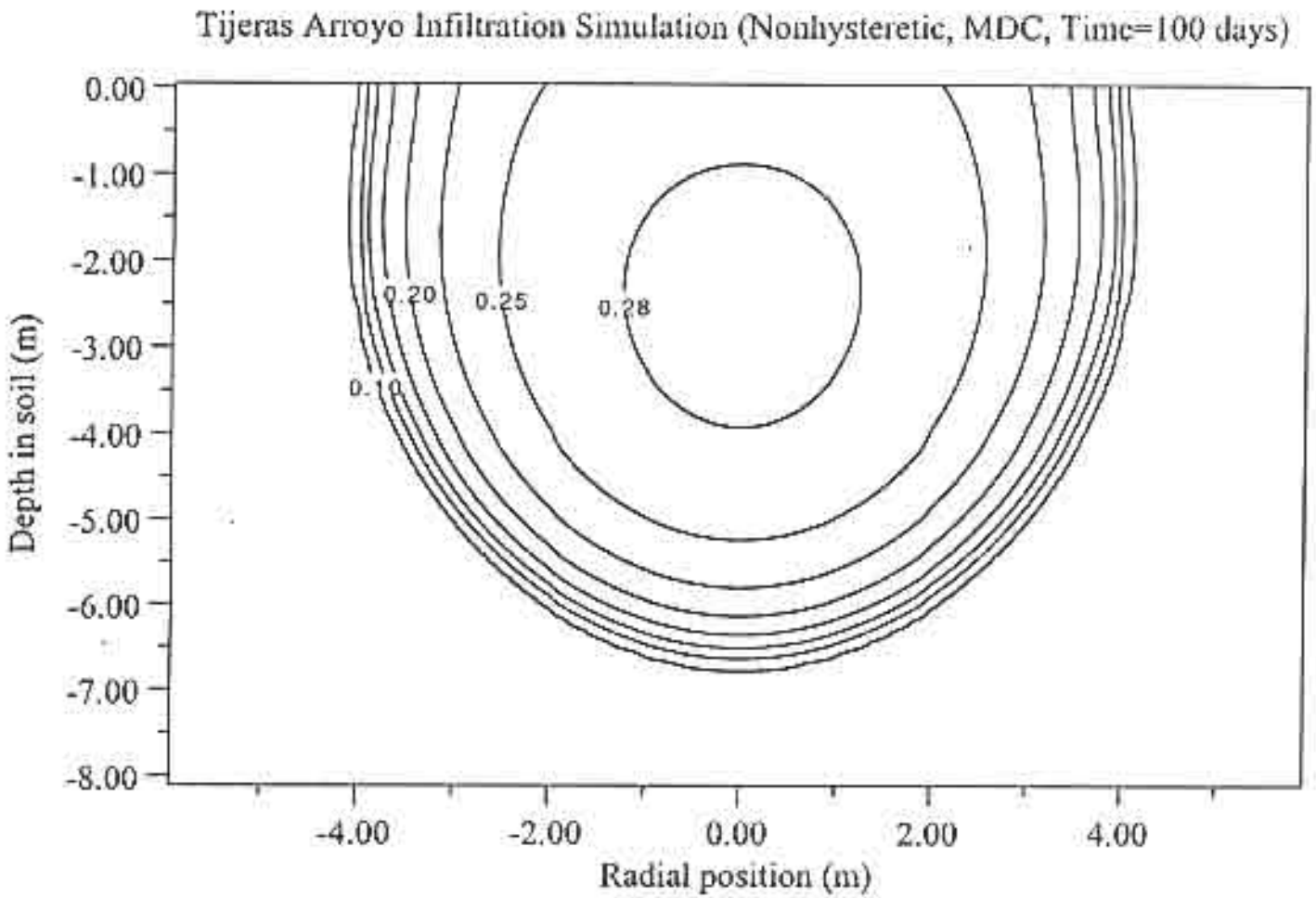

Figure 7.10: Tijeras Arroyo Infiltration Simulation (Nonhysteretic, MDC, Time = 100 days)

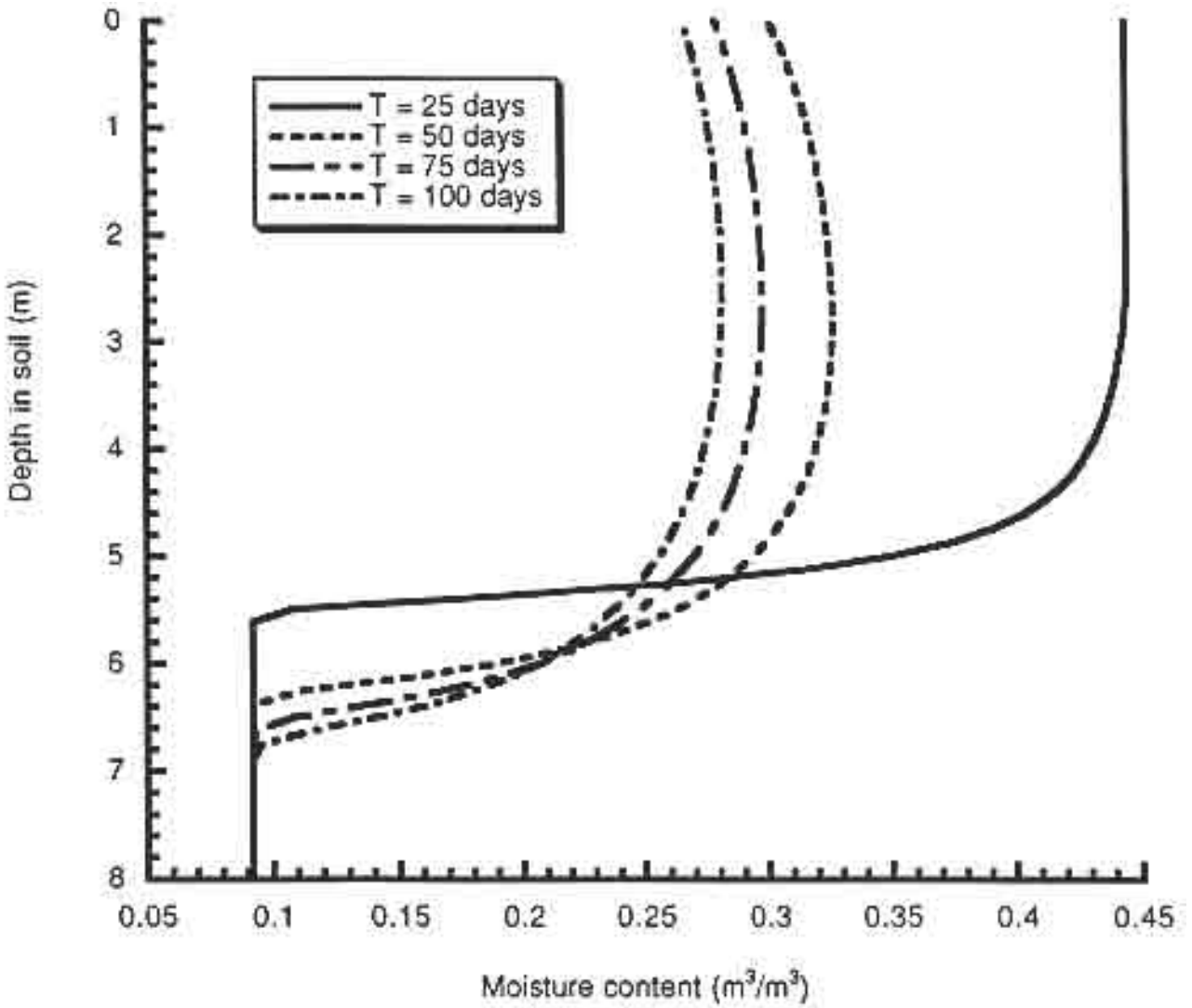

Figure 7.11: Profile Along the Axis of Symmetry (Non-hysteretic MDC)

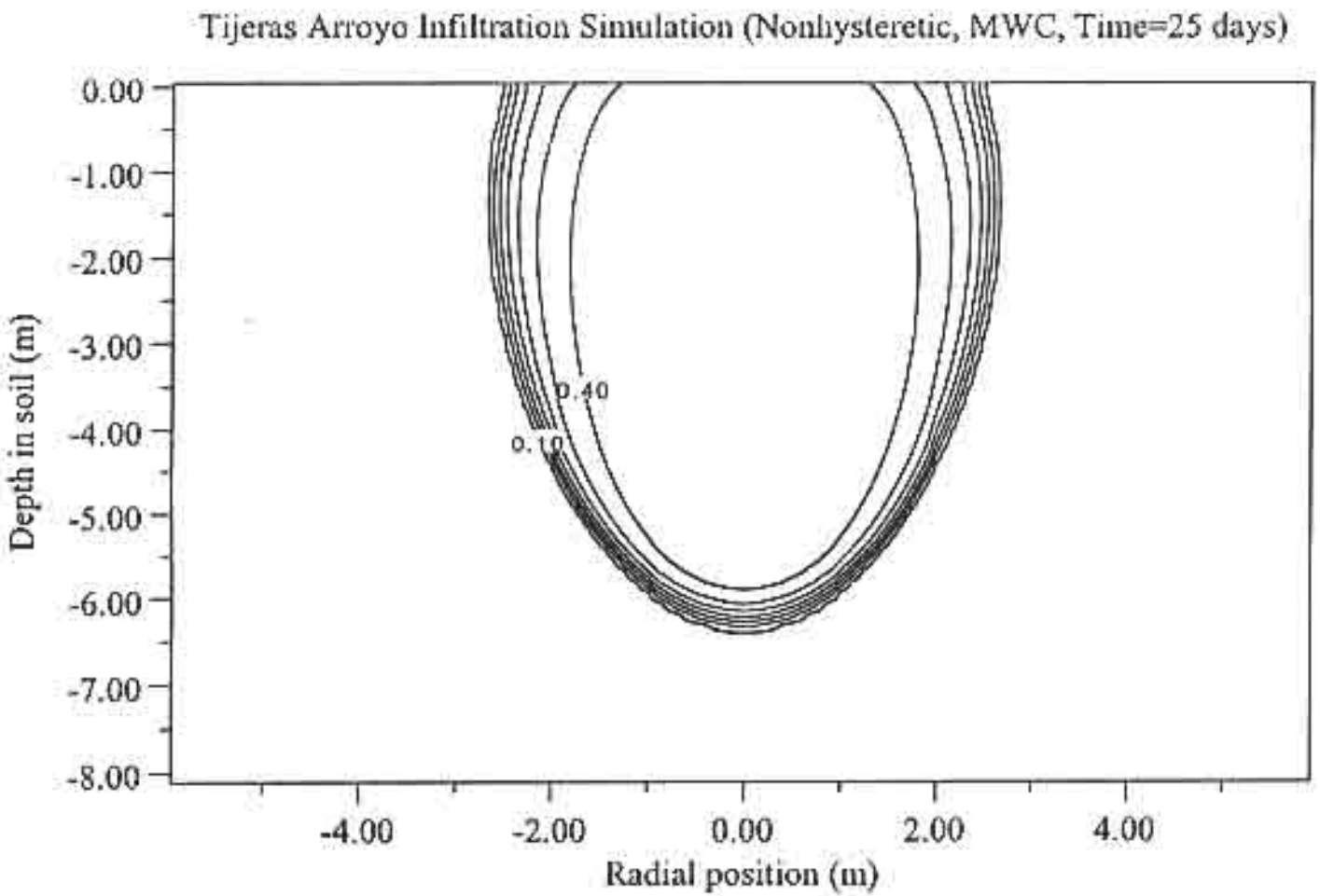

Figure 7.12: Tijeras Arroyo Infiltration Simulation (Nonhysteretic, MWC, Time = 25 days)

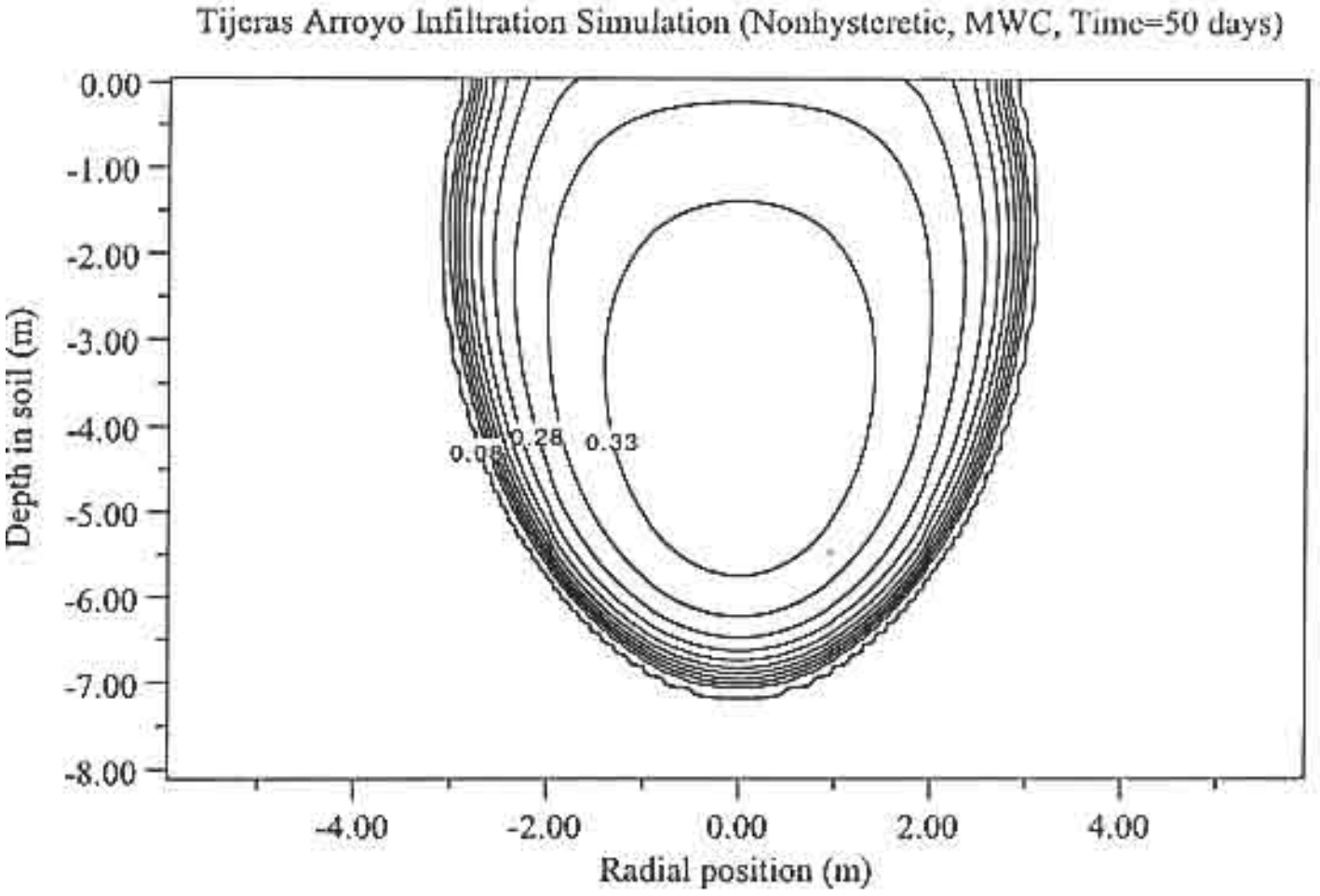

Figure 7.13: Tijeras Arroyo Infiltration Simulation (Nonhysteretic, MWC, Time = 50 days)

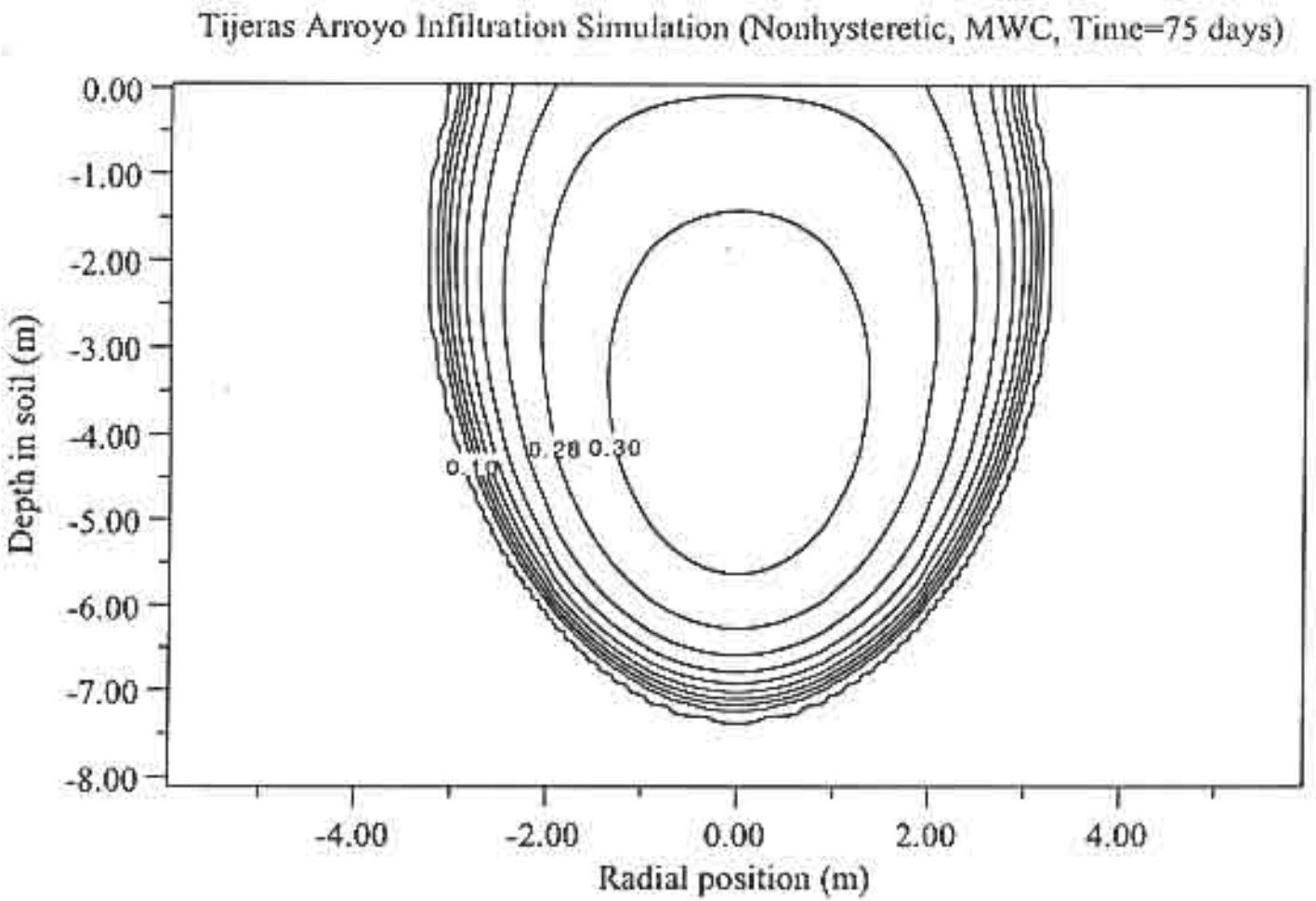

Figure 7.14: Tijeras Arroyo Infiltration Simulation (Nonhysteretic, MWC, Time = 75 days)

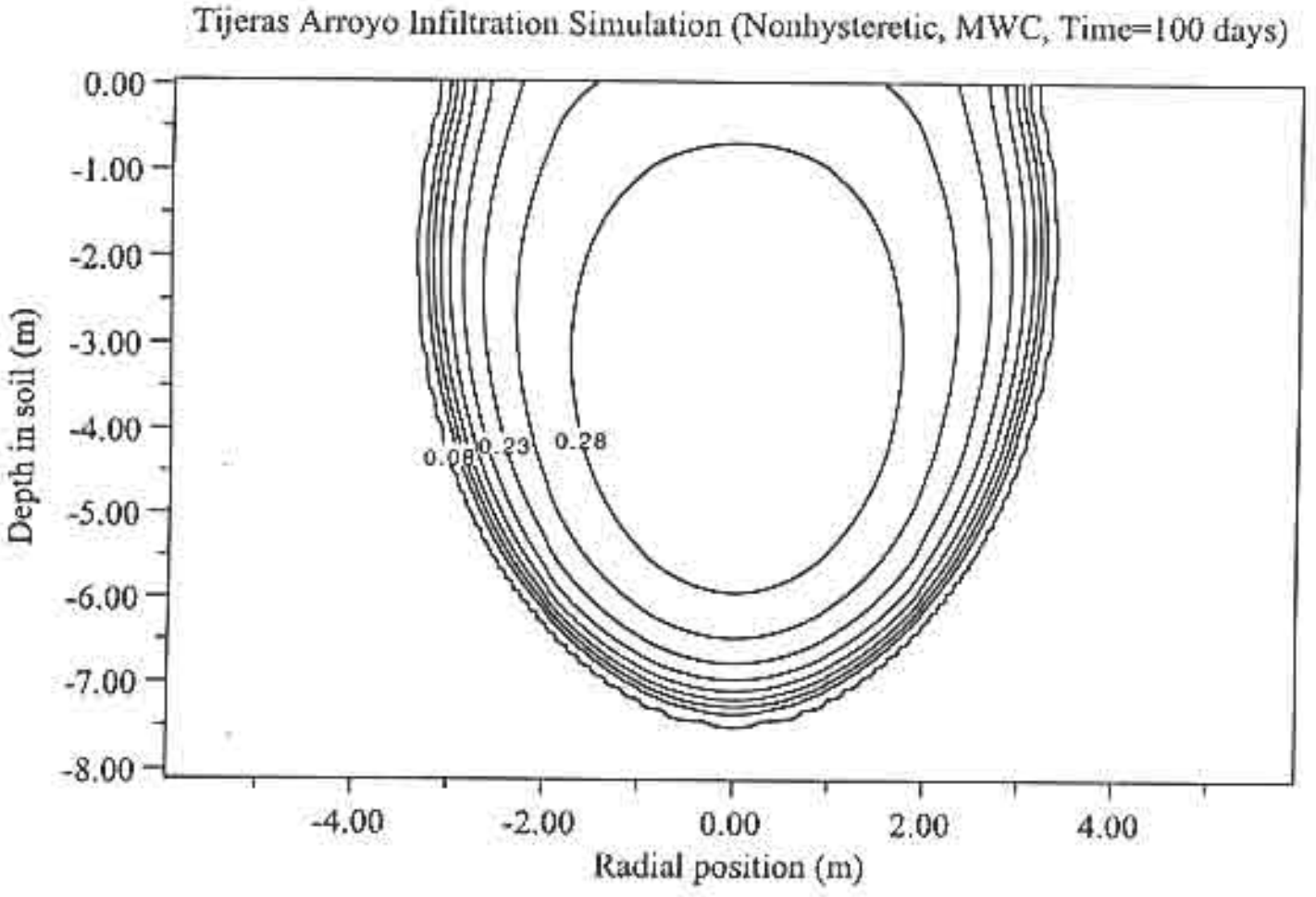

Figure 7.15: Tijeras Arroyo Infiltration Simulation (Nonhysteretic, MWC, Time = 100 days)

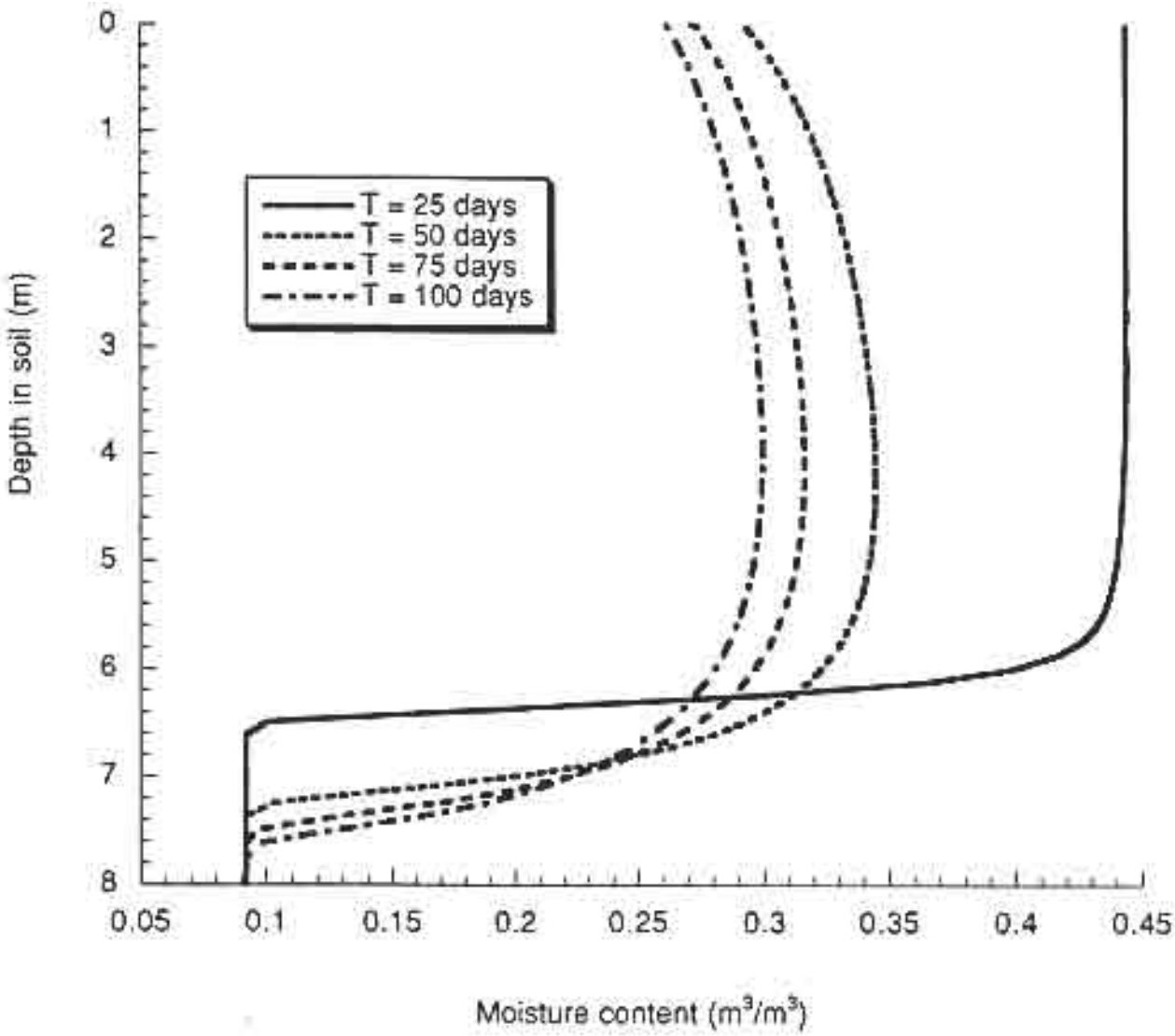

Figure 7.16: Profile Along the Axis of Symmetry (Non-hysteretic MWC)

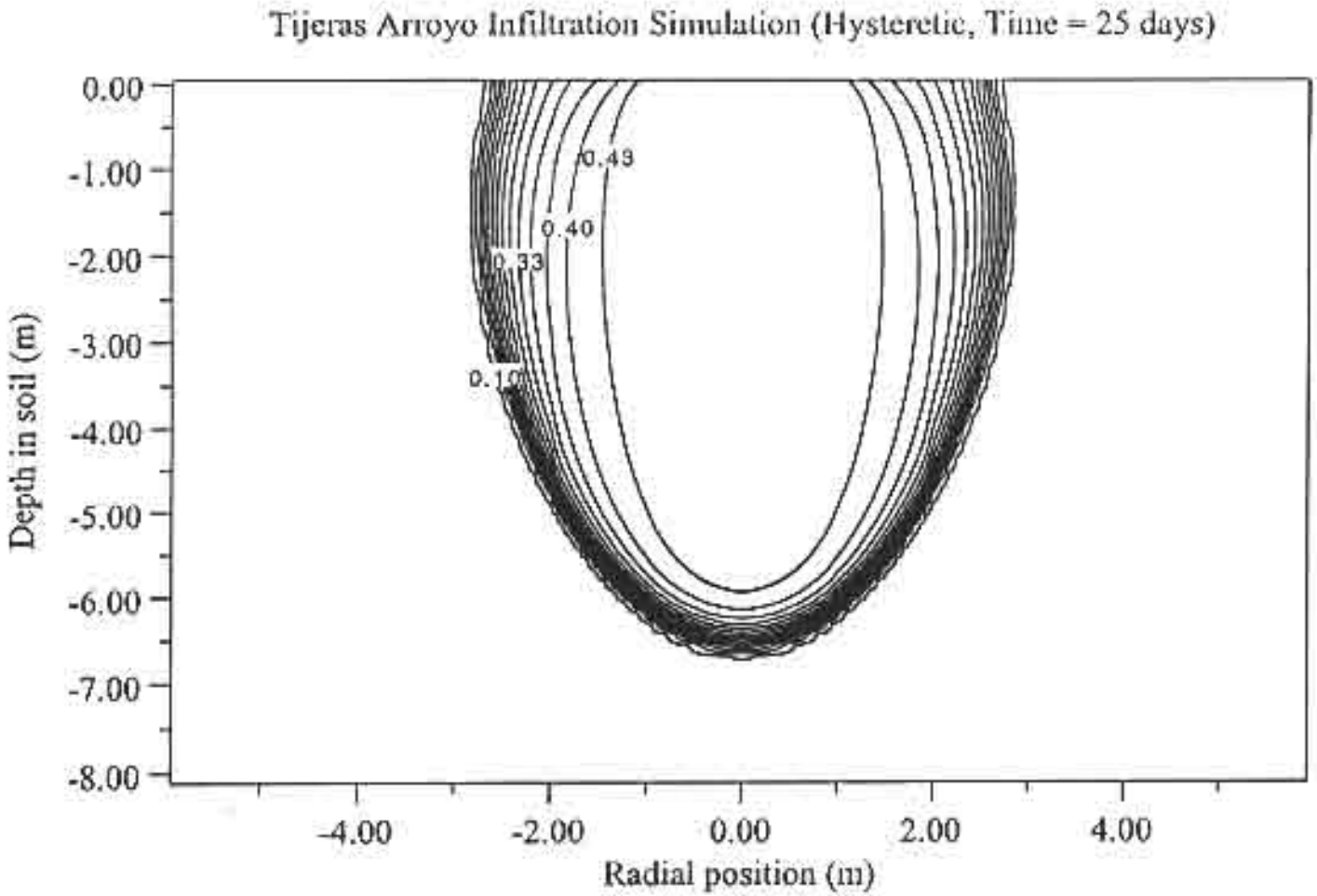

Figure 7.17: Tijeras Arroyo Infiltration Simulation (Hysteretic, Time = 25 days)

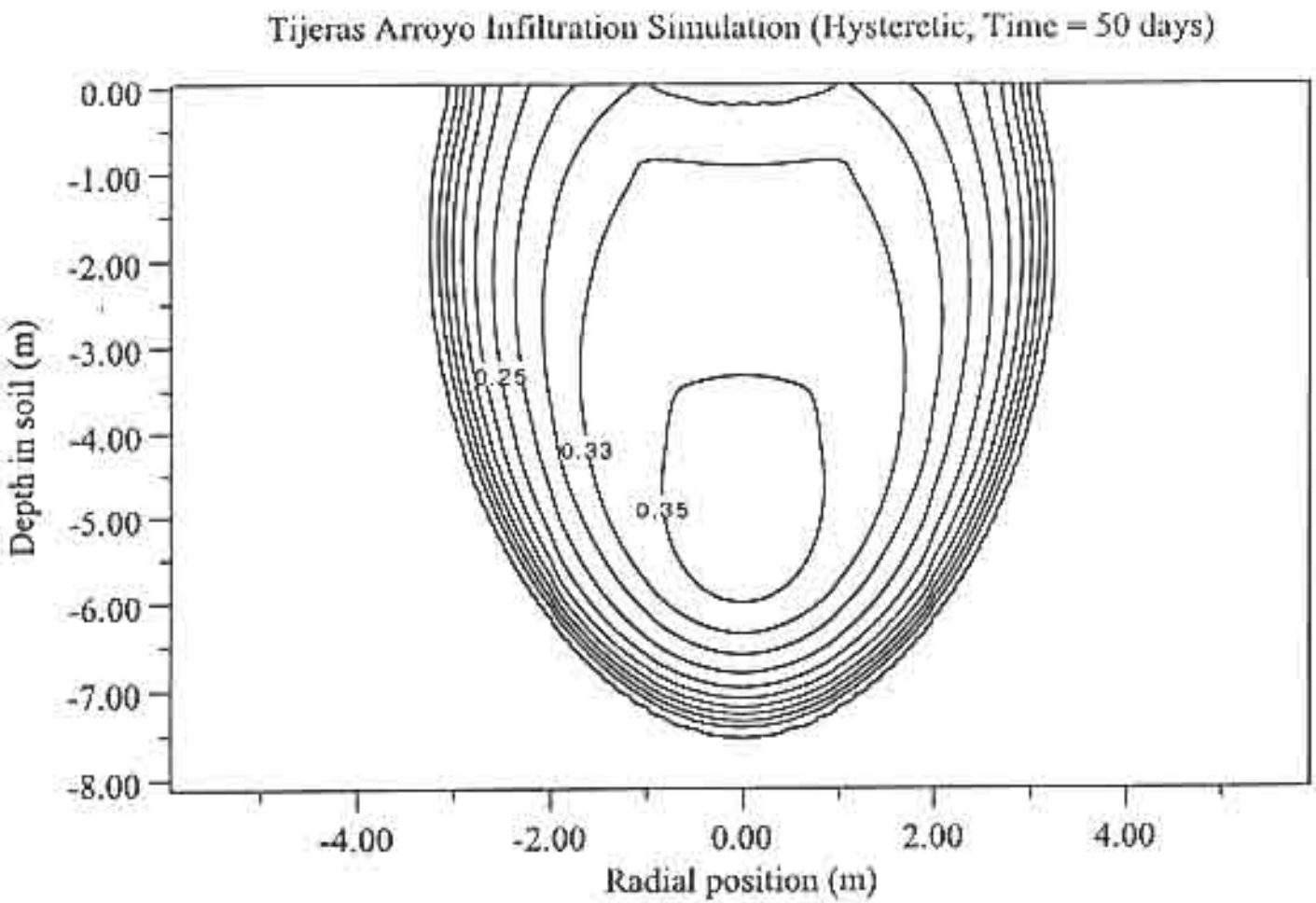

Figure 7.18: Tijeras Arroyo Infiltration Simulation (Hysteretic, Time = 50 days)

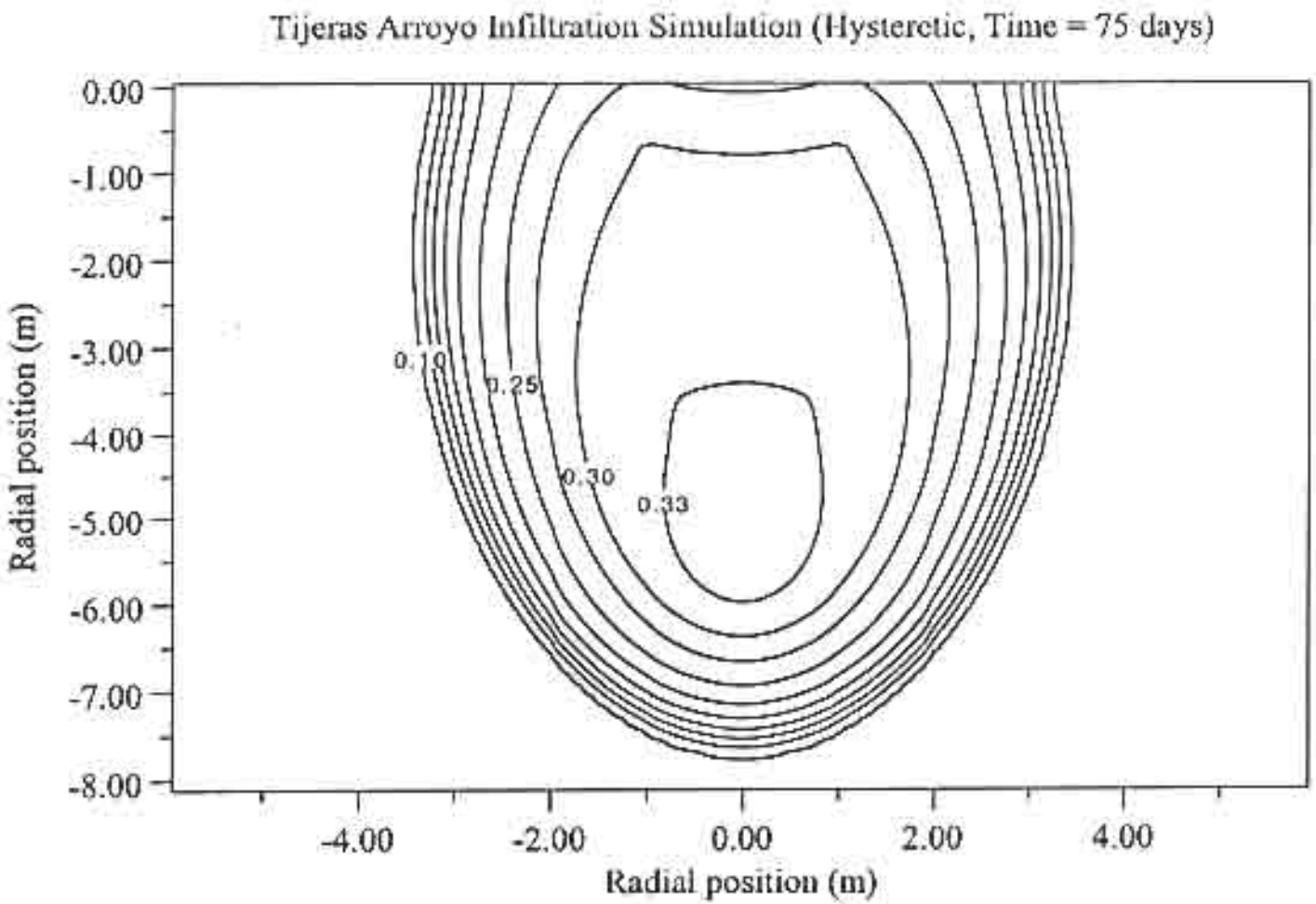

Figure 7.19: Tijeras Arroyo Infiltration Simulation (Hysteretic, Time = 75 days)

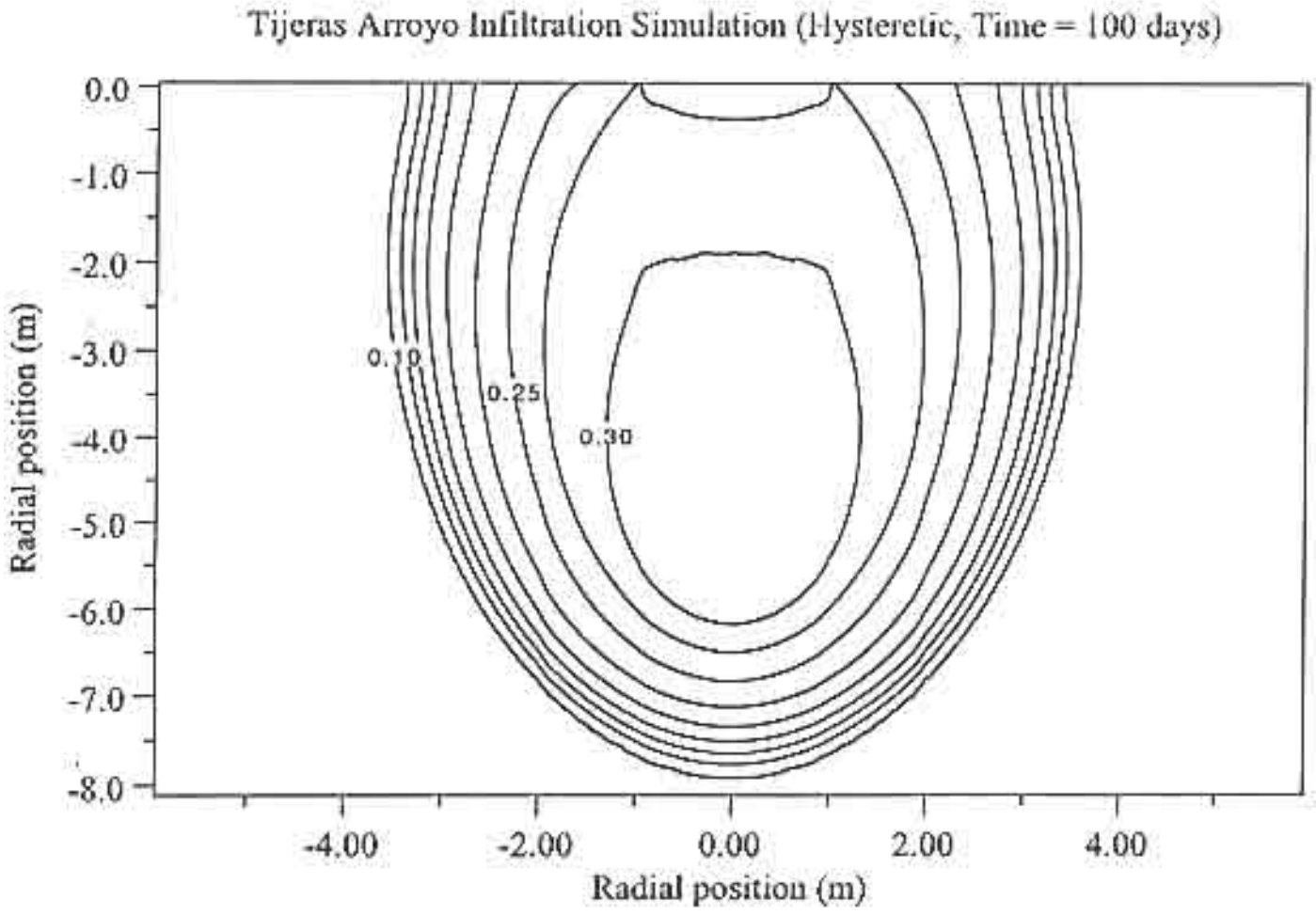

Figure 7.20: Tijeras Arroyo Infiltration Simulation (Hysteretic, Time = 100 days)

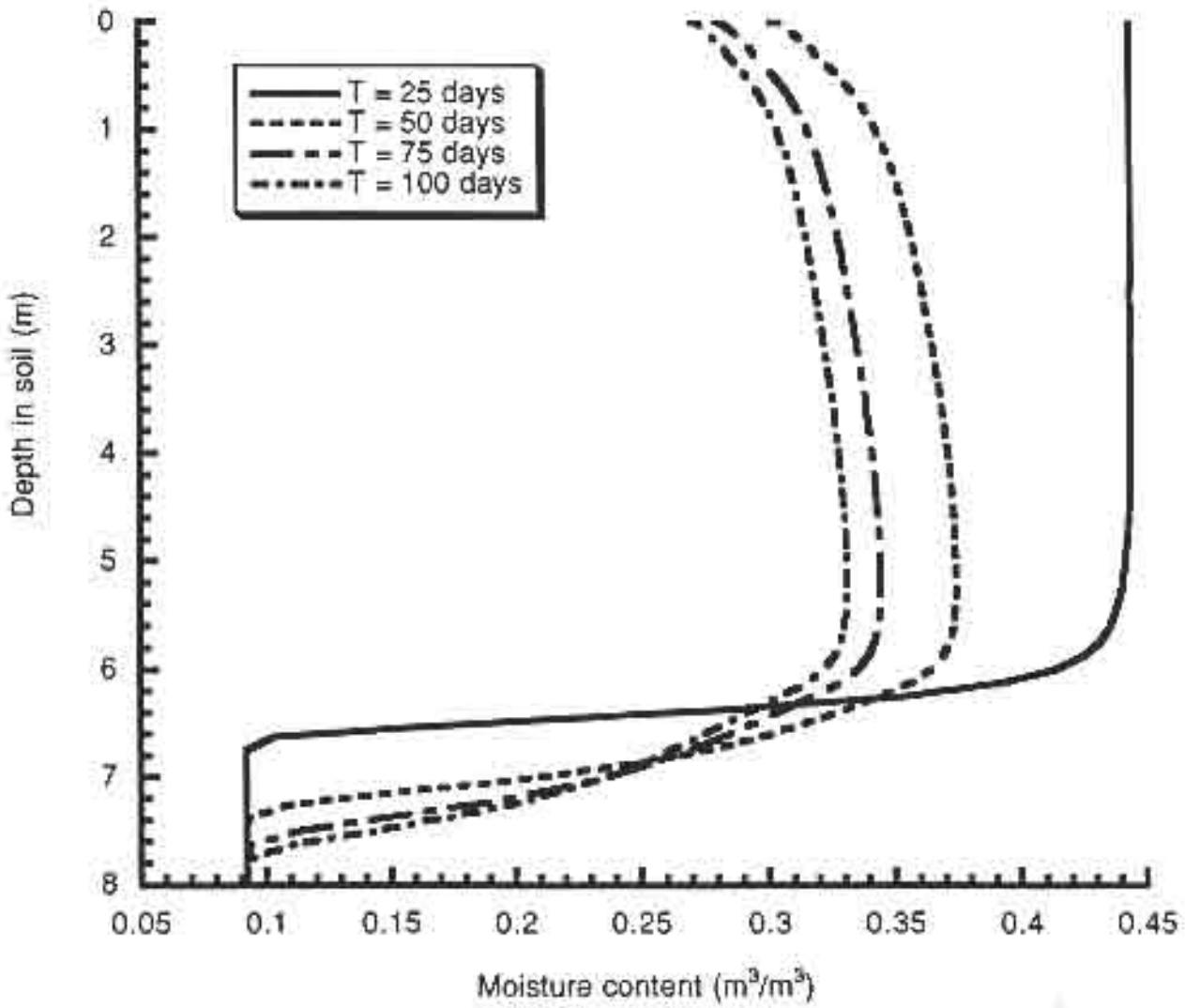

Figure 7.21: Profile Along the Axis of Symmetry (Hysteretic)

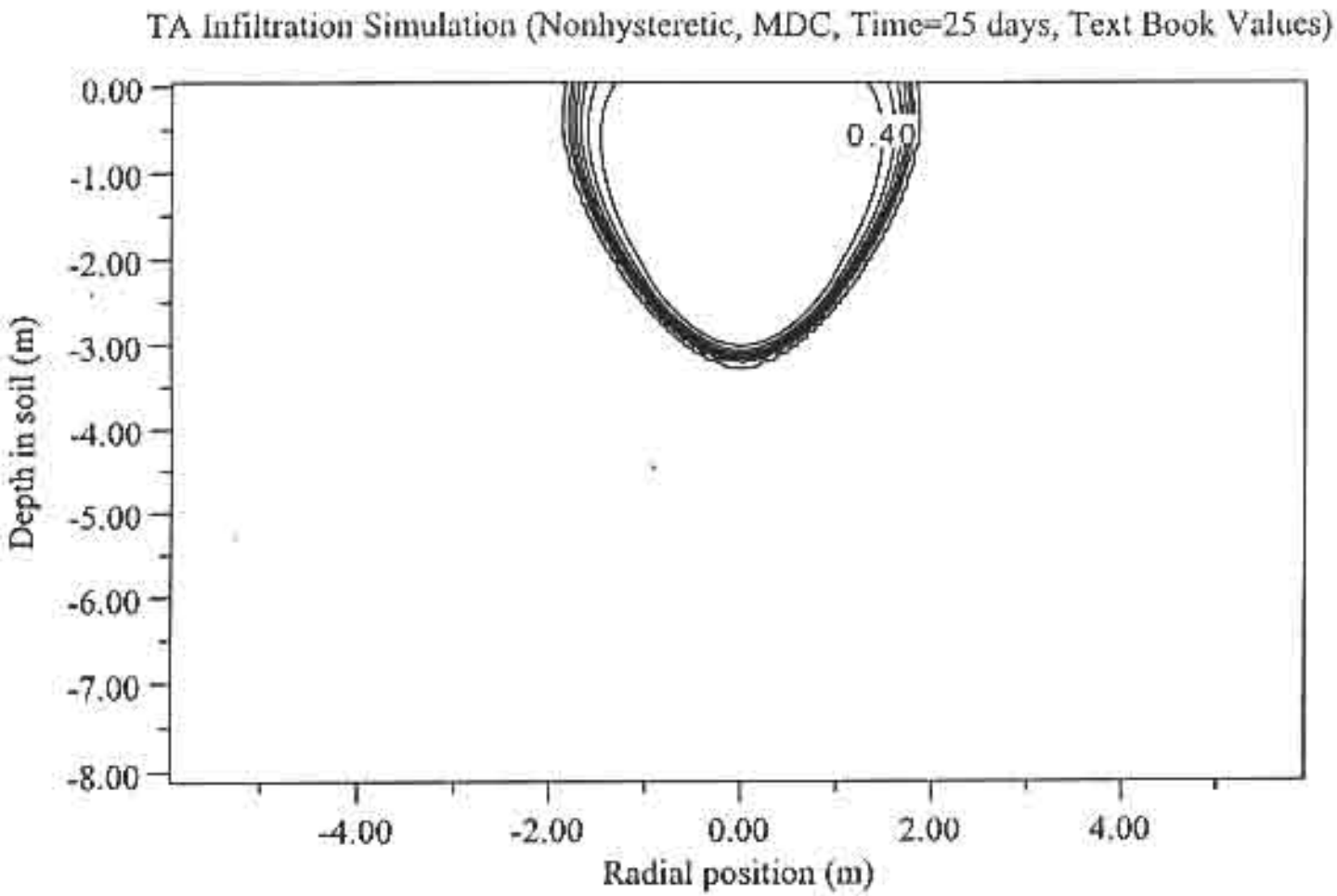

Figure 7.22: TA Infiltration Simulation (Nonhysteretic, MDC, Time = 25 days, Text Book Values)

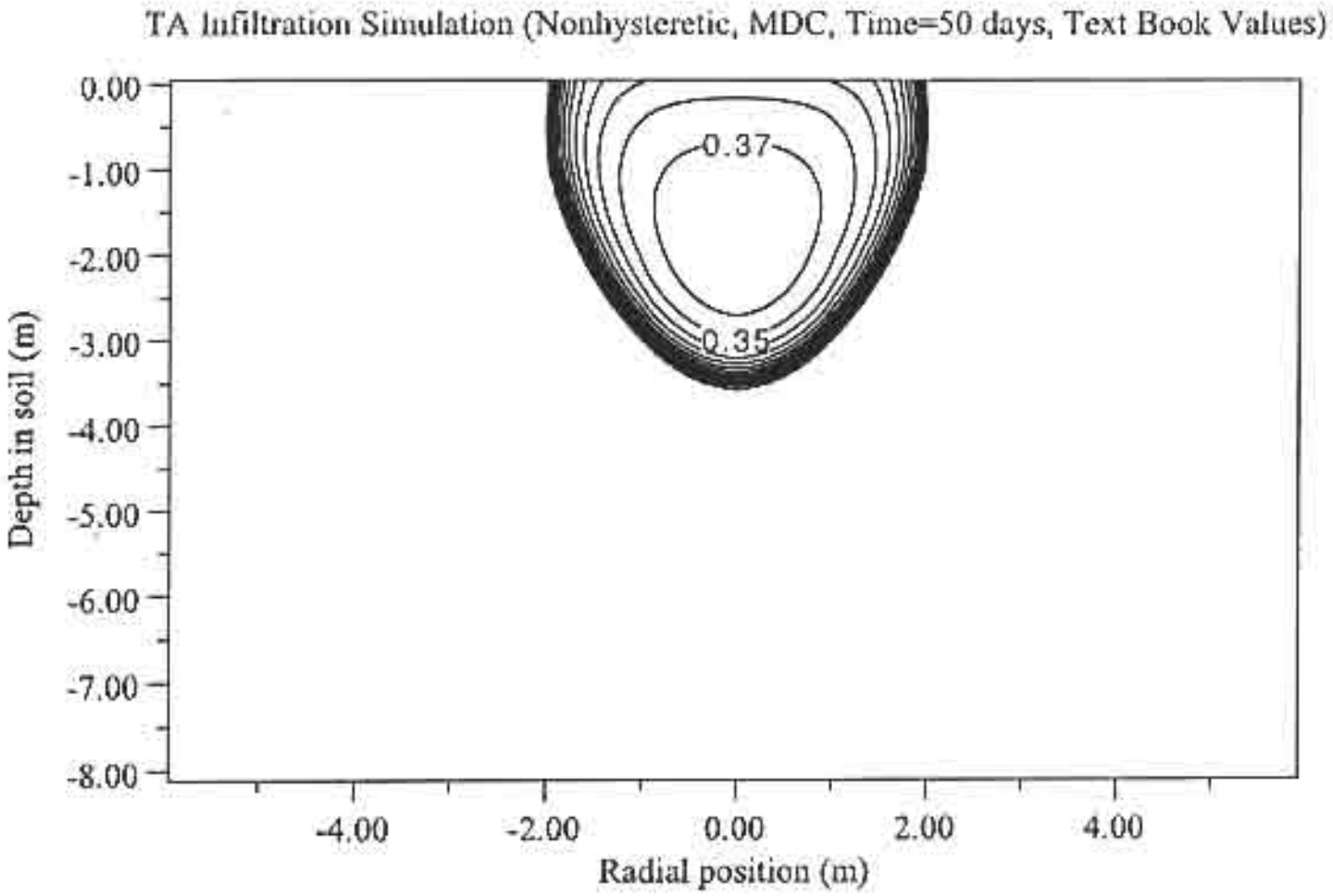

Figure 7.23: TA Infiltration Simulation (Nonhysteretic, MDC, Time = 50 days, Text Book Values)

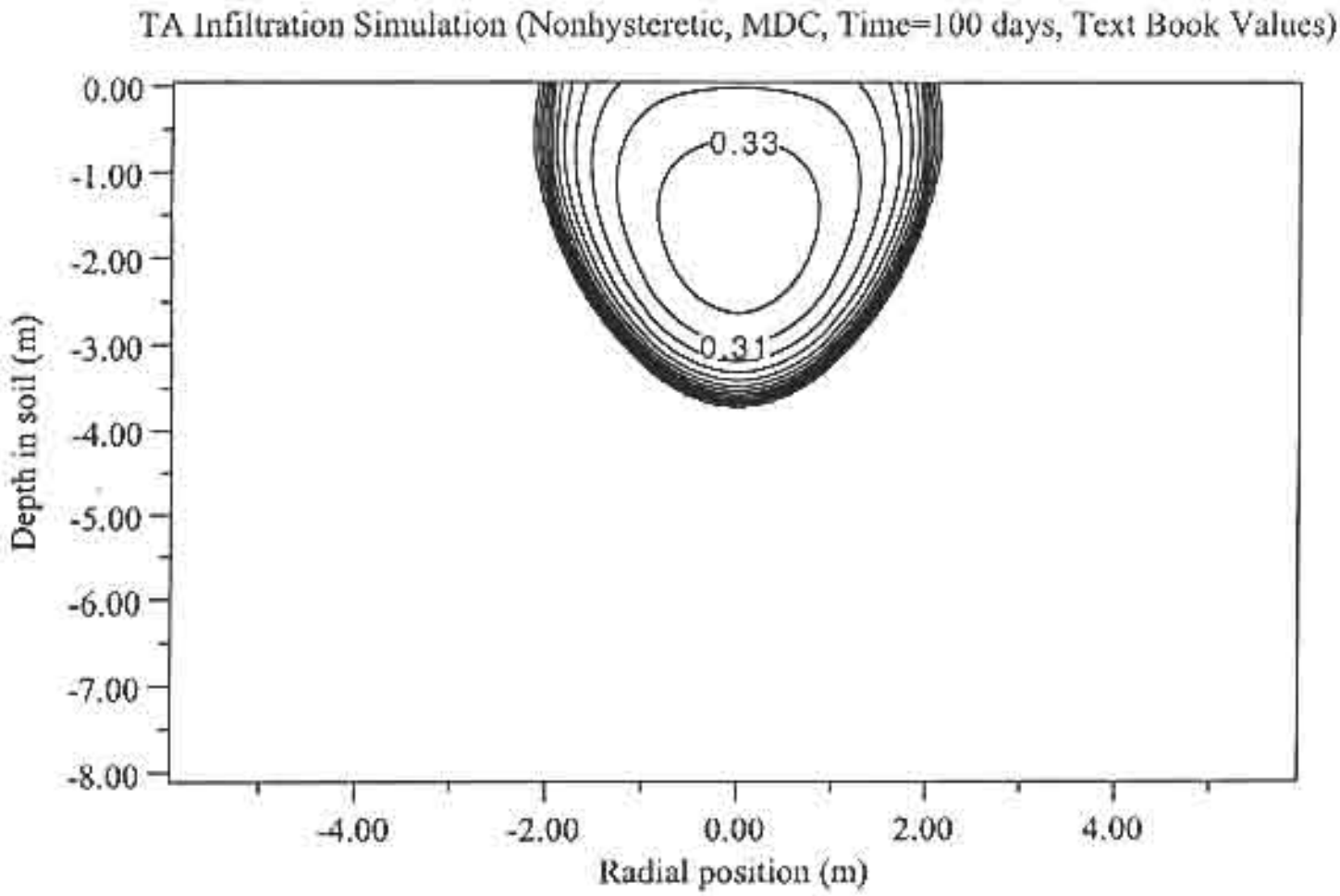

Figure 7.24: TA Infiltration Simulation (Nonhysteretic, MDC, Time = 100 days, Text Book Values)

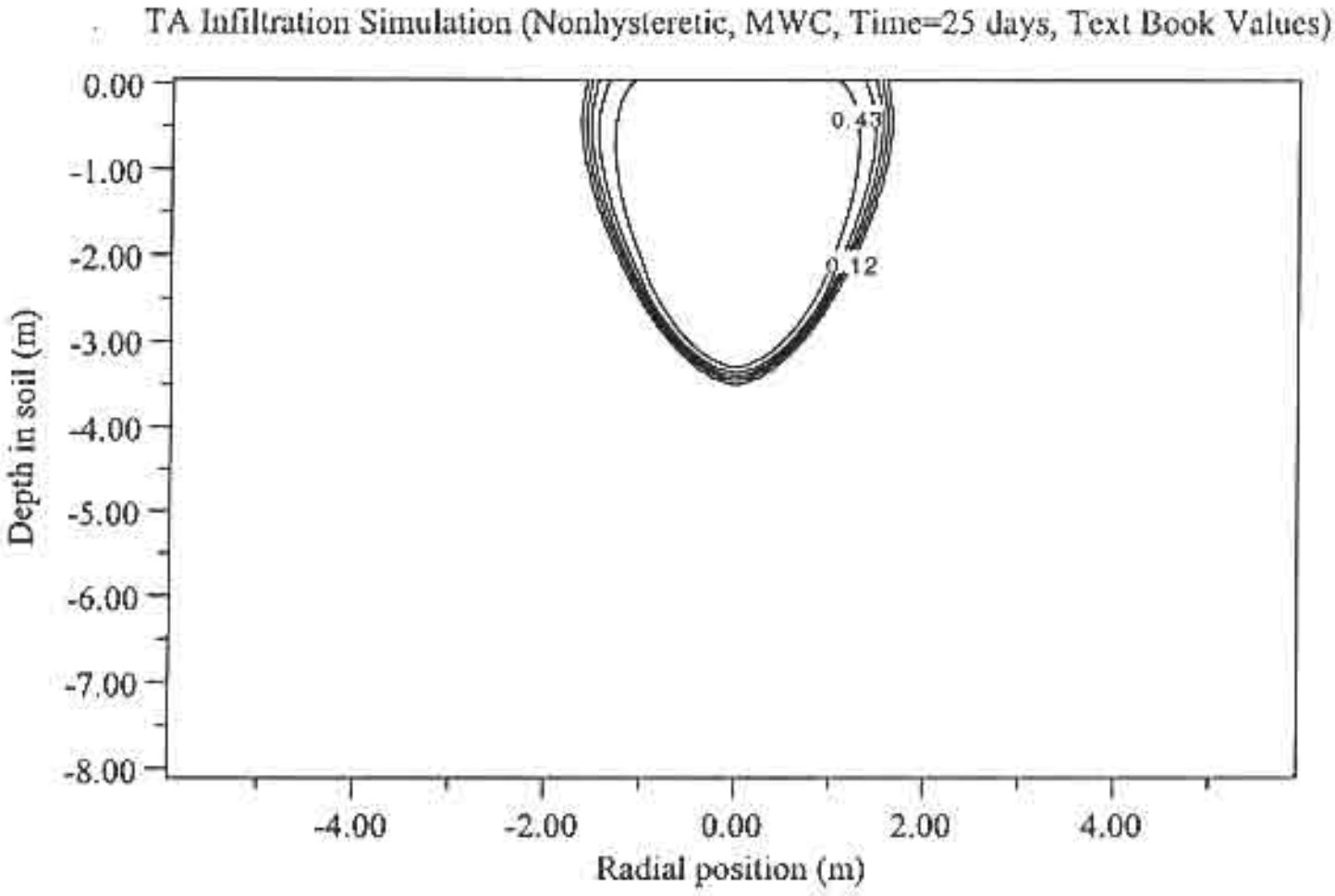

Figure 7.25: TA Infiltration Simulation (Nonhysteretic, MWC, Time = 25 days, Text Book Values)

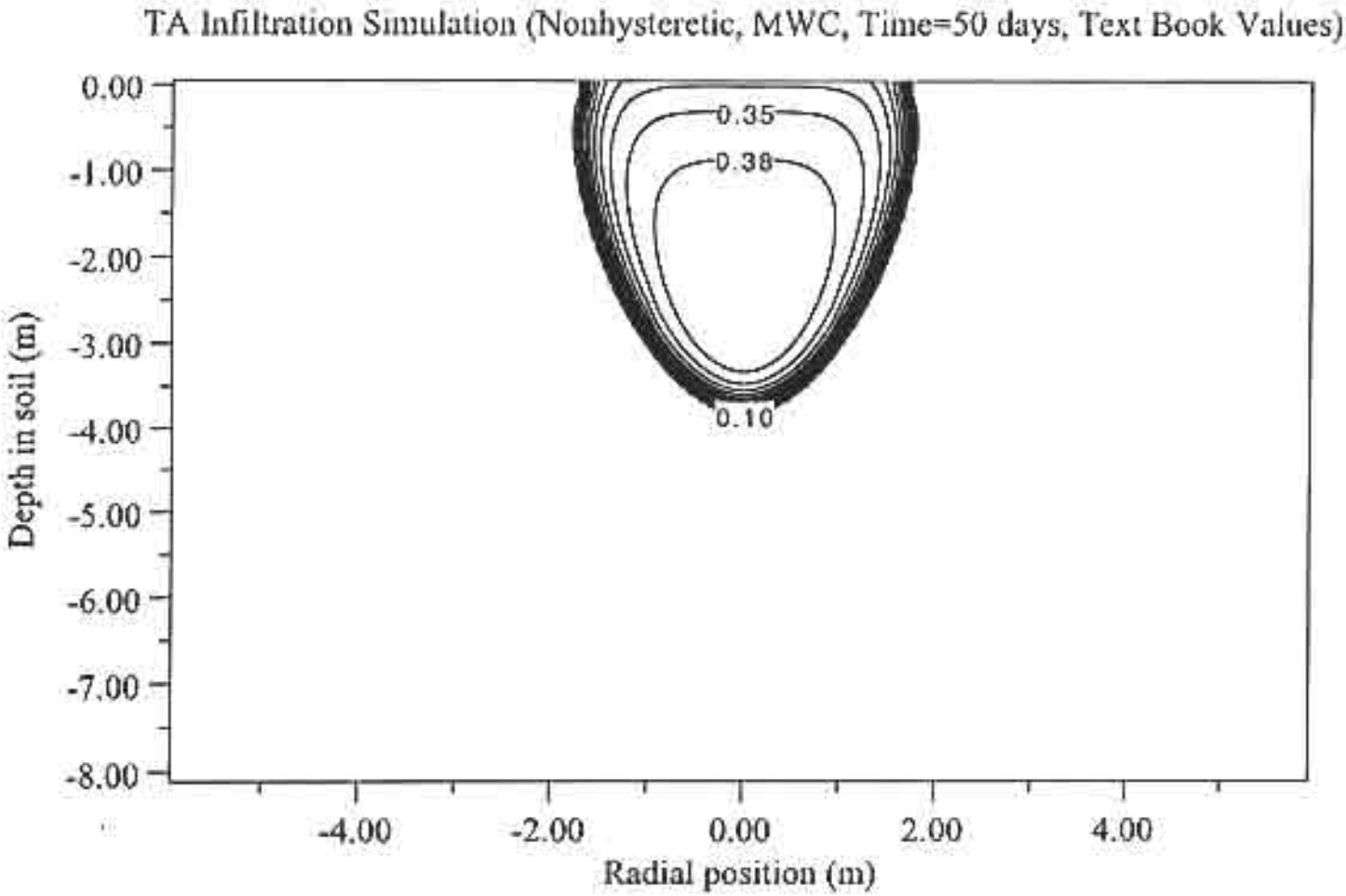

Figure 7.26: TA Infiltration Simulation (Nonhysteretic, MWC, Time = 50 days, Text Book Values)

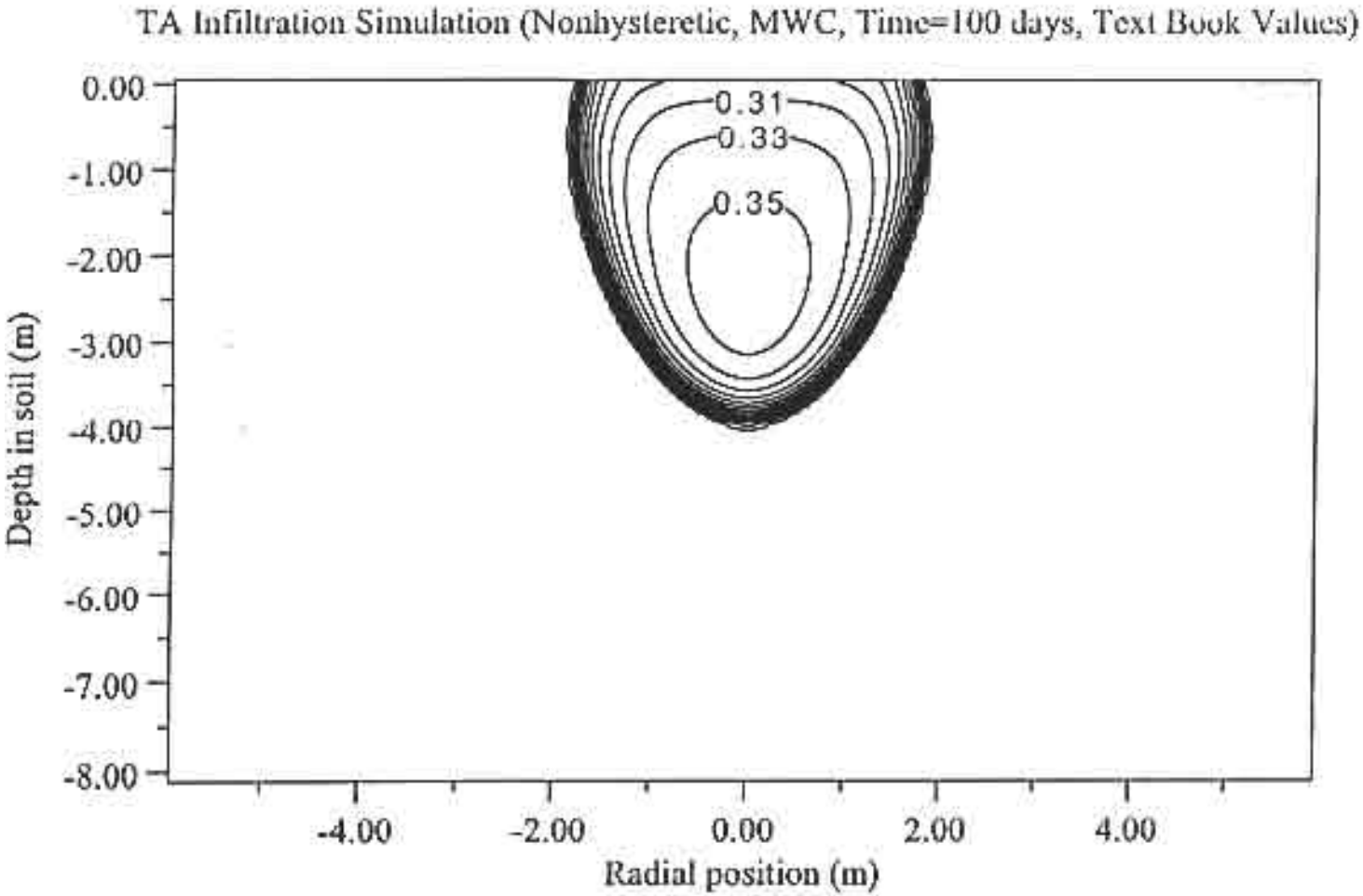

Figure 7.27: TA Infiltration Simulation (Nonhysteretic, MWC, Time = 100 days, Text Book Values)

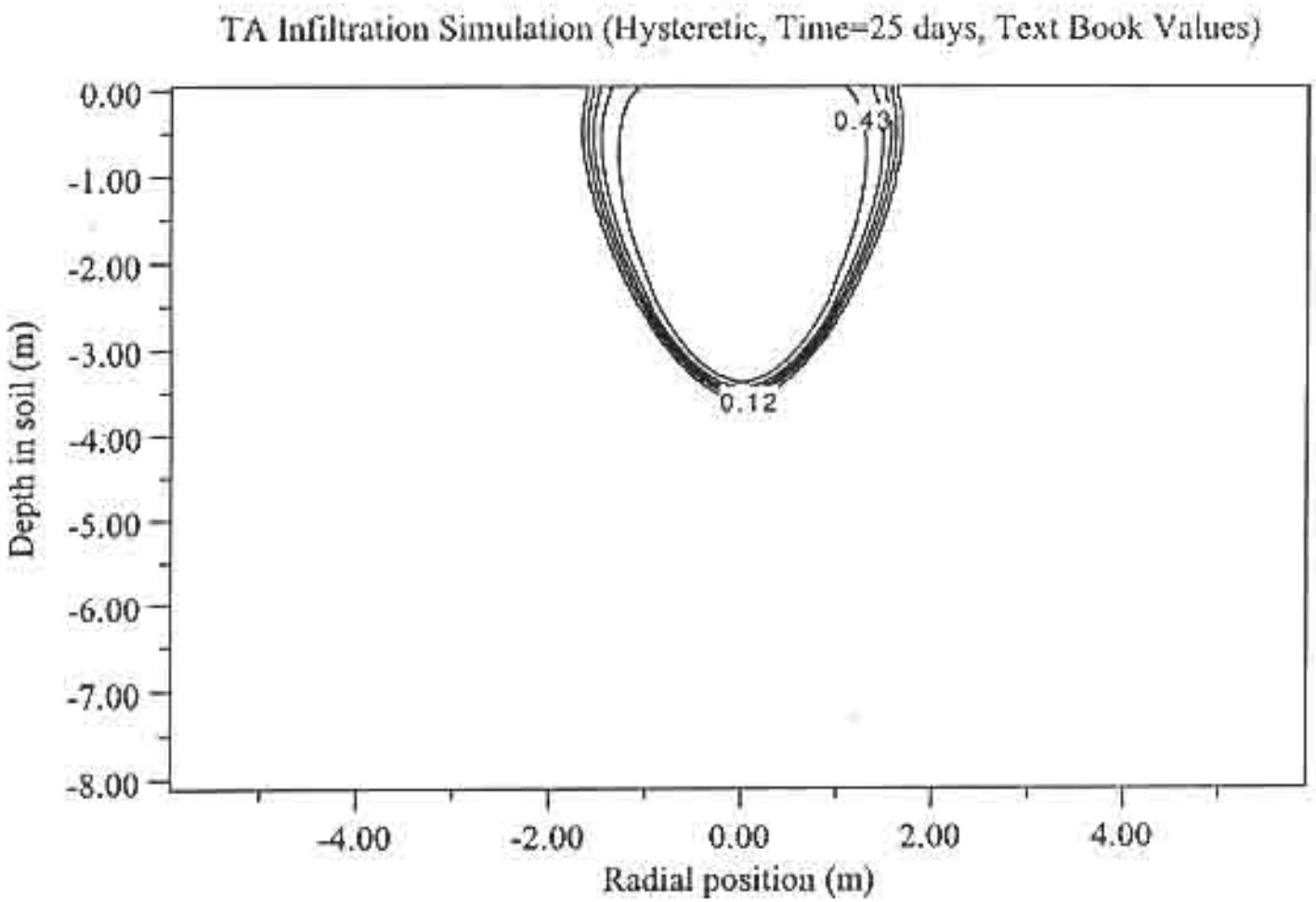

Figure 7.28: TA Infiltration Simulation (Hysteretic, Time = 25 days, Text Book Values)

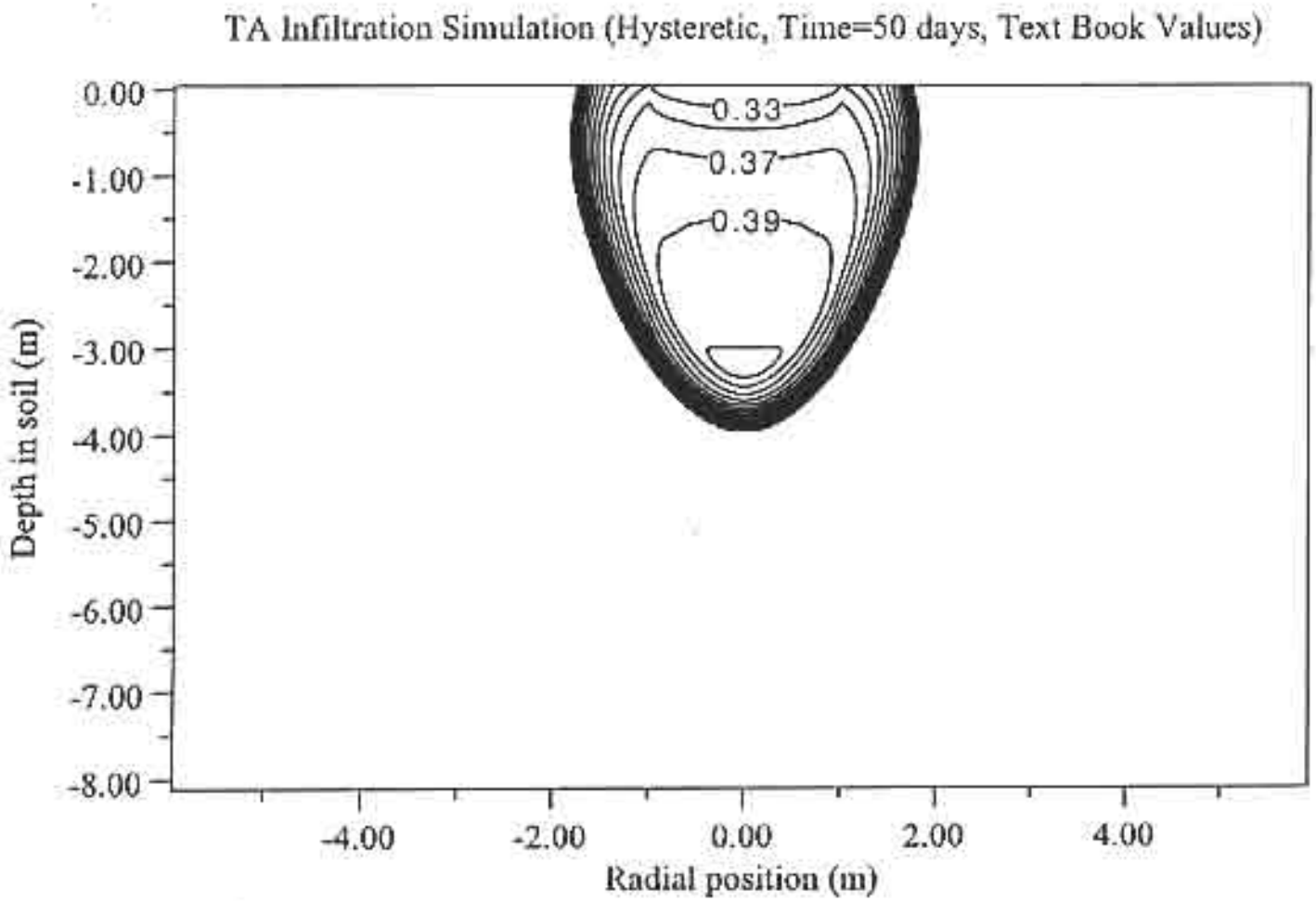

Figure 7.29: TA Infiltration Simulation (Hysteretic, Time = 50 days, Text Book Values)

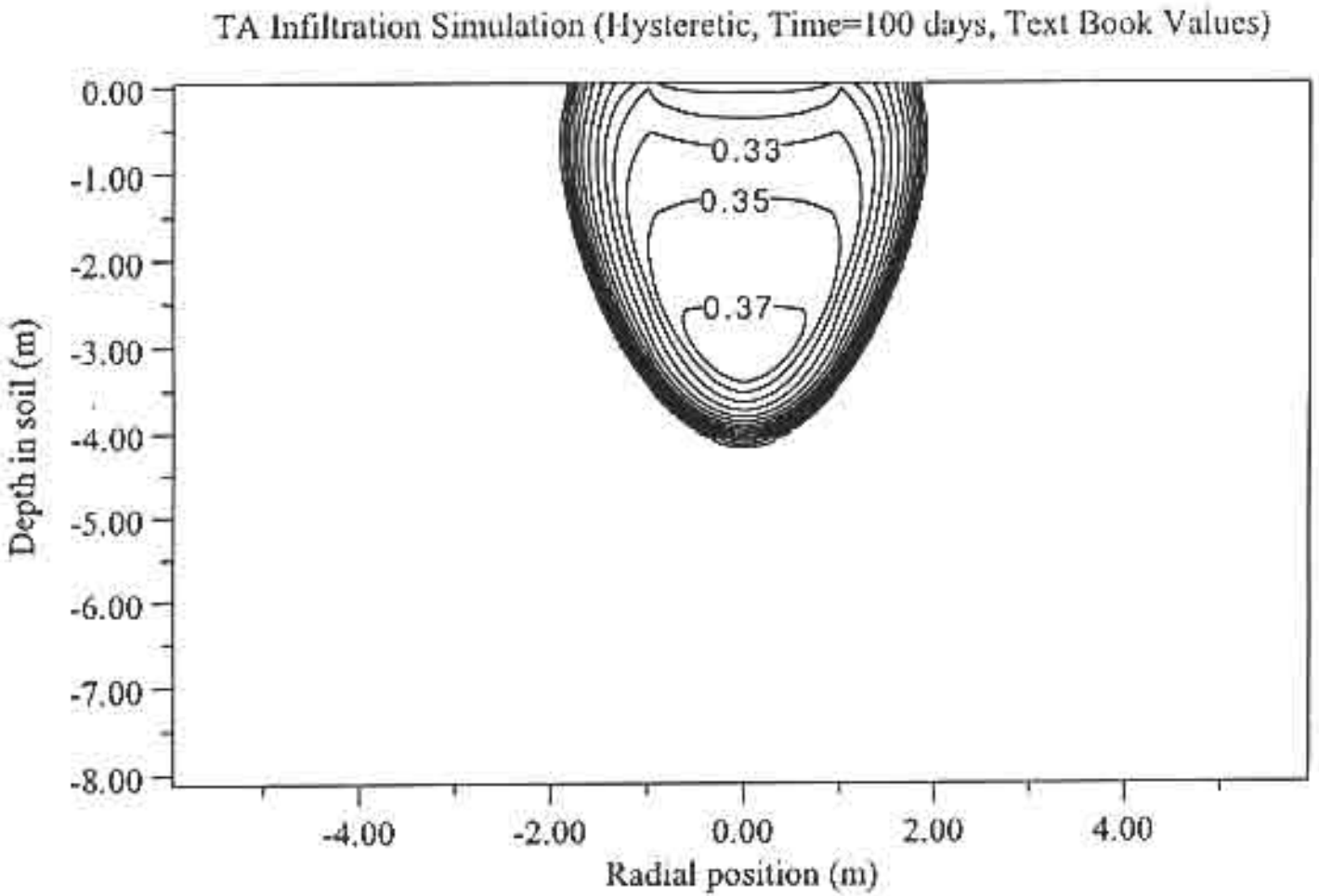

Figure 7.30: TA Infiltration Simulation (Hysteretic, Time = 100 days, Text Book Values)

TABLES

Table 5.1: Descriptors for Figure 5.2.3

Paired TDR-Tensiometer Groups	Description	Comments
NI1	North Inner Ring 1 Meter Deep	Same convention for 2, 3, & 4 m
NM1	North Medial Ring 1 Meter Deep	Same convention for 2, 3, & 4 m
NO1	North Outer Ring 1 Meter Deep	Same convention for 2, 3, & 4 m
EI1	East Inner Ring 1 Meter Deep	Same convention for 2, 3, & 4 m
EM1	East Medial Ring 1 Meter Deep	Same convention for 2, 3, & 4 m
EO1	East Outer Ring 1 Meter Deep	Same convention for 2, 3, & 4 m
SI1	South Inner Ring 1 Meter Deep	Same convention for 2, 3, & 4 m
SM1	South Medial Ring 1 Meter Deep	Same convention for 2, 3, & 4 m
SO1	South Outer Ring 1 Meter Deep	Same convention for 2, 3, & 4 m
WI1	West Inner Ring 1 Meter Deep	Same convention for 2, 3, & 4 m
WM1	West Medial Ring 1 Meter Deep	Same convention for 2, 3, & 4 m
WO1	West Outer Ring 1 Meter Deep	Same convention for 2, 3, & 4 m

Surface TDR Probes	Description	Comments
NES1	Northeast Surface	Numbered 1 - 9 from center out
SES1	Southeast Surface	Numbered 1 - 9 from center out
SWS1	Southwest Surface	Numbered 1 - 9 from center out
NWS1	Northwest Surface	Numbered 1 - 9 from center out

Neutron Access Tubes	Description	Comments
CTR	Located in Center of Infiltrometer	
NE2.5	Northeast Side 2.5 Meters from Center of Infiltrometer	Same convention for 4.5 & 5.5 m
SE2.5	Southeast Side 2.5 Meters from Center of Infiltrometer	Same convention for 4.5 & 5.5 m
SW2.5	Southwest Side 2.5 Meters from Center of Infiltrometer	Same convention for 4.5 & 5.5 m
NW2.5	Northwest Side 2.5 Meters from Center of Infiltrometer	Same convention for 4.5 & 5.5 m

Geology Holes	Description	Comments
NG	North Geology Hole	Located 2.5 Meters from Center of Infiltrometer, 4 Tensiometers/Hole
EG	East Geology Hole	Located 2.5 Meters from Center of Infiltrometer, 4 Tensiometers/Hole
SG	South Geology Hole	Located 2.5 Meters from Center of Infiltrometer, 4 Tensiometers/Hole
WG	West Geology Hole	Located 2.5 Meters from Center of Infiltrometer, 4 Tensiometers/Hole

Trenches	Description	Comments
T125	Trench oriented 125°	
T165	Trench oriented 165°	
T210	Trench oriented 210°	
T260	Trench oriented 260°	
T300	Trench oriented 300°	

Table 5.2: Water Flow Monitoring Components

Component	Description	Comments
Datalogger	Campbell Scientific, Inc. 21X	(Logan, UT)
Data Storage Module	Campbell Scientific, Inc. SM716	
Flow Meters	Omega FTB4607	Four high frequency pulse output
Pressure Transducers	Micro Switch PC126	Eight 0-5 psi differential (2 spares)
Cable	22-AWG two-pair shielded	
Water Level Monitor	Sandia-made	50-pin computer cable encased in fiberglass resin

Table 5.3: Water Temperature Monitoring System Components

Component	Description	Comments
Datalogger	Campbell Scientific, Inc. 21X	(Logan, UT)
Data Storage Module	Campbell Scientific, Inc. SM716	
Water Temperature Probe	Campbell Scientific, Inc. 107B	6 probes
Air Temperature Probe	Campbell Scientific, Inc. 107	2 probes

Table 5.4: TDR Moisture System Components

Component	Description	Comments
Computer	Compaq Contura	486 Notebook Computer
Cable Tester/Signal Generator	Tektronix 1502B	
Multiplexer	JFW Industries	16 and 24 port
Probes	Sandia-made	polycarbonate blocks with three-stainless steel rods (Diameter: 3/8 in., Length: 6 in.)
Cable	Alpha RG58-A	low noise coaxial

Table 5.5: Pressure System Components

Component	Description	Comments
Datalogger	Campbell Scientific, Inc. 21X	(Logan, UT)
Data Storage Module	Campbell Scientific, Inc. SM716	
Multiplexer	Campbell Scientific, Inc. AM-416	16 channel relay
Tensiometers	Sandia-made	112 tensiometers
Tensiometer Pipe	3/4 in Schedule 80 PVC	
Tensiometer Cup	Soil Moisture	1 bar porous ceramic
Tensiometer Sight Glass	1/2 in diameter polycarbonate	15 cm long, topped with rubber septum
Tensiometer Ruler		folded, plastic
Pressure Transducer	Micro Switch PC126	0 to 30 psi differential
Cable	22-AWG two-paired shielded	with 2 Con-x-all cable connectors

Table 5.6: Thermocouple System Components

Component	Description	Comments
Datalogger	Campbell Scientific, Inc. 21X	(Logan, UT)
Data Storage Module	Campbell Scientific, Inc. SM716	
Multiplexer	Campbell Scientific, Inc. AM-416	16 channel relay
Thermocouples	20-AWG TYPE T duplex insulated copper/constantan	48 total, assembled with a thermocouple welder
Thermocouple Welder	TIGTech, Inc. Model 116 SRL	(Lexington, MA)
Air Temperature Probe	Campbell Scientific, Inc. 107	8 probes

Table 5.7: Weather Station Components

Component	Description	Comments
Datalogger	Campbell Scientific, Inc. 21X	(Logan, UT)
Data Storage Module	Campbell Scientific, Inc. SM716	
Tripod	Campbell Scientific, Inc. CM6	
Air Temperature & Relative Humidity Probe	Vaisala, Inc. HMP35C	Housed in a Grilled Radiation Shield (air temperature in ºC, RH in %)
Tipping Bucket Rain Gage	Texas Instruments, Inc. TE525	Precipitation in millimeters
Barometric Pressure Sensor	Vaisala, Inc. PTA427	Barometric Pressure (mm of Hg)
Pyranometer	LI-COR, Inc. LI200S	(Lincoln, NE)
Soil Heat Flux Plate	Radiation Energy Balance Systems (REBS) HFT-3	(Seattle, WA)
Wind Speed Sensor	Met One, Inc. 014A	(Grants Pass, OR)
Soil Temperature Probes	Campbell Scientific, Inc. 107B	4 probes

Table 6.1: Moisture Content Results of Soil Samples Taken from the Geology Holes (see Table 5.1 for Explanation of Abbreviations)

Sample Number (location-depth below ground surface in meters)	Geologic Unit Number	Gravimetric Moisture Content (gm_w/gm_s)	Bulk Density (g_{ds}/ml_s)	Volumetric Moisture Content (ml_w/ml_s)
NG-0.33	7	0.09		
NG-1.83	6	0.03		
NG-2.33	5	0.10		
SG-0.33	7	0.12	1.45	0.17
SG-0.67	7	0.12	1.32	0.15
SG-1.0	7	0.06	1.42	0.08
SG-1.33	7	0.03		
SG-2.33	5	0.08		
SG-2.67	5	0.05		
SG-3.0	4	0.04		
WG-0.33	7	0.10		
WG-0.67	7	0.12		
WG-1.0	7	0.05		
WG-1.33	7	0.04	1.31	0.06
WG-1.67	6	0.02		
WG-2.0	6	0.04		
WG-2.33	5	0.10	1.34	0.14
WG-2.67	5	0.05		
WG-3.0	5	0.04		
WG-3.33	4	0.03		
EG-0.33	7	0.09	1.32	0.11
EG-0.67	7	0.10	1.27	0.13
EG-1.0	7	0.06	1.37	0.08
EG-1.33	7	0.02		
EG-1.67	6	0.01		
EG-2.0	6	0.03		
EG-2.25	5	0.03		
EG-2.33	5	0.10		
EG-2.67	5	0.05		
EG-3.0	5	0.04		

Table 6.2: Gravimetric Moisture Content Results of Soil Samples Taken from the 4.5 m Neutron Access Tubes (see Table 5.1 for Explanation of Abbreviations)

Sample Number (location-depth below ground surface in meters)	Geologic Unit	Gravimetric Moisture Content (gm_W/gm_S)
NE4.5-0.5	7	0.08
NE4.5-1.0	7	0.07
NE4.5-1.5	7	0.02
NE4.5-2.0	6	0.05
NE4.5-2.5	5	0.06
NE4.5-3.0	5	0.04
NE4.5-3.5	4	0.06
NE4.5-4.0A	3	0.07
NE4.5-4.0B	3	0.07
NE4.5-4.5	3	0.06
SE4.51-0.5	7	0.10
SE4.51-1.0	7	0.05
SE4.51-1.5	7	0.01
SE4.51-2.0	6	0.02
SE4.51-2.5A	5	0.08
SE4.51-2.5B	5	0.05
SE4.51-3.0	5	0.04
SE4.51-3.5	4	0.06
SE4.51-4.0	4	0.07
SE4.51-4.5	3	0.04
SW4.51-0.5	7	0.12
SW4.51-1.0	7	0.07
SW4.51-1.5	7	0.02
SW4.51-2.0	6	0.05
SW4.51-2.5	5	0.07
SW4.51-3.0	4	0.05
SW4.51-3.5	4	0.05
SW4.51-4.0	3	0.05
SW4.51-4.5	3	0.05
NW4.51-0.5	7	0.08
NW4.51-1.0	7	0.05
NW4.51-1.5	7	0.02
NW4.51-2.0	6	0.01
NW4.51-2.5	5	0.14
NW4.51-3.5	4	0.07
NW4.51-4.0	3	0.06
NW4.51-4.5	3	0.03

Table 7.1: Fitting parameters for the van Genuchten model using undisturbed samples

Parameter	Main Drying Curve (MDC)	Main Wetting Curve (MWC)
θ_r	0.00023	0.00023
θ_s	0.445	0.445
n	1.336	1.336
α (1/m)	0.727	1.454
K_s (m/day)	0.305	-

Table 7.2: Fitting parameters for the van Genuchten model for a typical silt

Parameter	Main Drying Curve (MDC)	Main Wetting Curve (MWC)
θ_r	0.034	0.034
θ_s	0.460	0.460
n	1.370	1.370
α (1/m)	1.600	3.200
K_s (m/day)	0.060	-

Table 7.3: Two-dimensional grid system used to perform the simulation of the model problem

Axial Position (m)	N_z	Δz (m)	Radial Position (m)	N_r	Δr (m)
0.0-1.0	20	0.0500	0.0-1.0	20	0.0500
1.0-2.0	16	0.6250	1.0-2.0	16	0.6250
2.0-4.0	24	0.0833	2.0-4.0	24	0.0833
4.0-8.0	32	0.1250	4.0-6.0	16	0.1250